ESTIMATION OF AERODYNAMIC LOADS OF A PROPELLER THROUGH IMPROVED BLADE ELEMENT AND MOMENTUM THEORY AND PROPELLER DESIGN OPTIMIZATION

A THESIS SUBMITTED TO
THE GRADUATE SCHOOL OF NATURAL AND APPLIED SCIENCES
OF
MIDDLE EAST TECHNICAL UNIVERSITY

BY

DERYA KAYA

IN PARTIAL FULFILLMENT OF THE REQUIREMENTS
FOR
THE DEGREE OF DOCTOR OF PHILOSOPHY
IN
AEROSPACE ENGINEERING

JUNE 2021

Approval of the thesis:

ESTIMATION OF AERODYNAMIC LOADS OF A PROPELLER THROUGH IMPROVED BLADE ELEMENT AND MOMENTUM THEORY AND PROPELLER DESIGN OPTIMIZATION

submitted by **DERYA KAYA** in partial fulfillment of the requirements for the degree of **Doctor of Philosophy** i**n Aerospace Engineering, Middle East Technical University** by,

Prof. Dr. Halil Kalıpçılar
Dean, Graduate School of **Natural and Applied Sciences** _____

Prof. Dr. İsmail H. Tuncer
Head of the Department, **Aerospace Engineering** _____

Assist. Prof. Dr. Ali Türker Kutay
Supervisor, **Aerospace Engineering Department, METU** _____

Examining Committee Members:

Prof. Dr. Ozan Tekinalp
Aerospace Engineering Department, METU _____

Assist. Prof. Dr. Ali Türker Kutay
Aerospace Engineering Department, METU _____

Prof. Dr. Kemal Leblebicioğlu
Electrical and Electronics Engineering Department, METU _____

Prof. Dr. Nafiz Alemdaroğlu
Aerospace Engineering Department, Atılım University _____

Assist. Prof. Dr. Özcan Yırtıcı
Computer Engineering Department, Osmaniye Korkut Ata University _____

Date: 25.06.2021

I hereby declare that all information in this document has been obtained and presented in accordance with academic rules and ethical conduct. I also declare that, as required by these rules and conduct, I have fully cited and referenced all material and results that are not original to this work.

Name, Last name : Derya Kaya

Signature :

ABSTRACT

ESTIMATION OF AERODYNAMIC LOADS OF A PROPELLER THROUGH IMPROVED BLADE ELEMENT AND MOMENTUM THEORY AND PROPELLER DESIGN OPTIMIZATION

Kaya, Derya
Doctor of Philosophy, Aerospace Engineering
Supervisor : Assist. Prof. Dr. Ali Türker Kutay

June 2021, 106 pages

This study focuses on accurate prediction of total forces and moments acting on a propeller in all flight conditions through Blade Element and Momentum Theory (BEMT) and design optimization of a UAV propeller. Under various flight conditions such as hover, vertical climb, and forward flight, propeller generates different aerodynamic loads in different free-stream velocities, propeller disk angles of attack, and propeller's angular speeds. For this reason, it is important to have a mathematical model that predicts all forces and moments generated by the propeller under these different flight conditions. Propeller aerodynamic loads at different flight conditions can also be found experimentally (e.g., wind tunnel or real-flight tests) or computationally (i.e., Computational Fluid Mechanics (CFD) methods) but these methods are time-consuming. As well, experimental methods are not affordable for optimization studies. The mathematical model obtained from model-based calculations of propeller aerodynamic loads is more useful compared to CFD and experimental methods. However, some assumptions in classical Blade Element Theory and assuming the induced velocity constant cause inaccurate prediction of the propeller's forces and moments in model-based approaches. On the other hand, the Improved BEMT (IBEMT) model proposed in this study can estimate the

propeller performance in wide flight regimes from hover to forward flight for unmanned aircraft applications. It is computationally efficient in fast optimization studies. Induced velocity is calculated iteratively at each annulus of the rotor disc. Euler integration is used in the calculation of the propeller's aerodynamic loads at each blade section and azimuth angle. The improved model is validated with wind tunnel experiments and it is compared with the results of experimental data of another study and CFD result for which the geometric properties of the propeller used and operating conditions are known in detail. Besides, in this study, design optimization of a propeller is also conducted using MATLAB® Optimization Tool-Box and the IBEMT model.

Keywords: Propeller Aerodynamics, Blade Element and Momentum Theory, Induced Velocity, Wind Tunnel Experiments, Propeller Design Optimization

ÖZ

BİR PERVANENİN AERODİNAMİK YÜKLERİN GELİŞTİRİLMİŞ PALA ELEMANI VE MOMENTUM TEORİSİ YOLUYLA TAHMİNİ VE PERVANE TASARIM OPTİMİZASYONU

Kaya, Derya
Doktora, Havacılık ve Uzay Mühendisliği
Tez Yöneticisi: Dr. Öğr. Üyesi Ali Türker Kutay

Haziran 2021, 106 sayfa

Bu çalışma, Pala Elemanı ve Momentum Teorisi aracılığıyla tüm uçuş koşullarında pervaneye etki eden toplam kuvvet ve momentlerin doğru tahminine ve bir İnsansız Hava Aracı (İHA) pervanesinin tasarım optimizasyonuna odaklanmaktadır. Askıda kalma, dikey tırmanma ve ileri uçuş gibi çeşitli uçuş koşulları altında, pervane, farklı serbest akış hızlarında, pervane disk hücum açılarında ve pervanenin açısal hızlarında farklı aerodinamik yükler üretir. Bu nedenle, bu farklı uçuş koşulları altında pervane tarafından oluşturulan tüm kuvvetleri ve momentleri tahmin eden bir matematiksel modele sahip olmak önemlidir. Farklı uçuş koşullarında pervane aerodinamik yükleri deneysel olarak (örneğin, rüzgar tüneli veya gerçek uçuş testleri) veya hesaplamalı (örneğin, Hesaplamalı Akışkanlar Mekaniği (HAD) yöntemleri) olarak bulunabilir, ancak bu yöntemler zaman alıcıdır. Ayrıca, deneysel yöntemler optimizasyon çalışmaları için karşılanabilir değildir. Pervane aerodinamik yüklerinin model tabanlı hesaplarından elde edilen matematiksel model, HAD ve deneysel yöntemlere göre daha kullanışlıdır. Bununla birlikte, klasik Pala Elemanı Teorisindeki bazı varsayımlar ve endüvi hızın sabit varsayılması, model tabanlı yaklaşımlarda pervane kuvvetlerinin ve momentlerinin yanlış tahmin edilmesine

neden olur. Öte yandan, bu çalışmada önerilen iyileştirilmiş BEMT (IBEMT) modeli, insansız hava aracı uygulamaları için havada asılı kalma koşulundan ileri uçuşa kadar geniş uçuş rejimlerinde pervane performansını tahmin edebilir. Hızlı optimizasyon çalışmalarında hesaplama açısından verimlidir. Endüvi hız, rotor diskinin her bir halkasında iteratif olarak hesaplanır. Pervanenin her kanat kesitinde ve azimut açısında aerodinamik yüklerinin hesaplanmasında Euler entegrasyonu kullanılmıştır. Geliştirilen model rüzgar tüneli deneyleri ile doğrulanmış ve kullanılan pervanenin geometrik özelliklerinin detaylı olarak bilinen başka bir çalışmanın deney datası ve HAD sonuçları ile karşılaştırılmıştır. Ayrıca, bu çalışmada, MATLAB® Optimization Tool-Box ve IBEMT modeli kullanılarak bir pervanenin tasarım optimizasyonu da gerçekleştirilmiştir.

Anahtar Kelimeler: Pervane Aerodinamiği, Pala Elemanları ve Momentum Teorisi, Endüvi Hız, Rüzgar Tüneli Deneyleri, Pervane Tasarım Optimizasyonu

To my dearest parents…

ACKNOWLEDGMENTS

I would like to express my deepest gratitude to my thesis supervisor, Asst. Prof. Dr. Ali Türker Kutay for his encouragement, advice, criticism, and valuable discussion throughout my research. During my graduate years, my gratitude and respect for him grew exponentially. He was always understanding, helpful, and wise to me. Dr. Kutay, thank you very much for accepting me as your graduate student and starting this journey. Without your guidance and help, I would not be able to finish this work.

I want to thank my thesis committee members, Prof. Dr. Nafiz Alemdaroğlu, Prof. Dr. Ozan Tekinalp, Prof. Dr. Kemal Leblebicioğlu, and Assist. Prof. Dr. Özcan Yırtıcı, for their suggestions and comments that improves my thesis. Besides, I would like to thank Assoc. Prof. Dr. Ercan Gürses and Derya Kaya Topa for their guidance and help during the submission procedure of the thesis. Special thanks to my friends Merve, Nilay, Sedat, and Zuhal for their friendship throughout my life and my office roommate Dilek for her positive energy and friendship, and to my colleague Harun for his technical assistance, and to Yudum and Berk for their chats in coffee hours. Special thanks to Anas for his never-ending assistance. Without his help and guidance, I would not be able to perform the wind tunnel experiments.

And the well-deserved last thanks go to my family that I feel so grateful to have them: Boncuk, Tırt, Siren, Uzay, Mars, and Toras; thank you for taking my time and repaying it with your unconditional love and disregard, s*evgili eşim* Engin for his love, care, and support since the moment I met him, without his support and assistance I would not be able to finish this work, *biricik abim* Deniz for his guidance and friendship which makes me feel like the luckiest sister ever, and my dearest father İsmail Kaya and dearest mother Fatma Kaya, who are by my side whenever and wherever I need them, for their love, care, and support throughout my life. *Canım babam ve canım annem, bu tezi size ithaf ediyorum çünkü bu tez benim olduğu kadar sizin de başarınız.*

TABLE OF CONTENTS

LIST OF TABLES

TABLES

LIST OF FIGURES

FIGURES

LIST OF ABBREVIATIONS

ACRONYMS

A.o.A.	Angle of Attack
AOF	Aggregate Objective Function
BET	Blade Element Theory
BEMT	Blade Element and Momentum Theory
CFD	Computational Fluid Dynamics
IBEMT	Improved Blade Element and Momentum Theory
RPM	Revolution Per Minute
UAV	Unmanned Aerial Vehicle
VTOL	Vertical Take-Off and Landing

SYMBOLS

α	Propeller Disk Angle of Attack
α_b	Angle of Attack of the Blade Section
Ω	Propeller's Angular Speed in *radian/second*
n	Propeller's Angular Speed in *revolutions/second*
V_∞	Free-Stream Velocity
c	Chord of the Blade
C_d	Drag Coefficient
$\overline{C_d}$	Average Drag Coefficient
C_l	Lift Coefficient

C_T	Thrust Coefficient
J	Advance Ratio
J	Aggregate Objective Function
η	Propeller Aerodynamic Efficiency
v_i	Induced Velocity
a	Lift Curve Slope
σ	Solidity Ratio
$\boldsymbol{\sigma}$	Sigmoid Function
S	Reference Area of the Propeller
D	Diameter of the Propeller
T	Thrust Force
H	Hub Force
Y	Side Force
Q	Rotor Torque
P	Pitching Moment
R	Rolling Moment
R	Radius of the Propeller
ψ	Azimuth Angle
θ_0	Zero Twist Angle
θ_{tw}	Twist Angle
ϕ	Local Inflow Angle
N	Number of Blades

A	Area Captured by the Propeller
$\boldsymbol{AR}$	Aspect Ratio
a	2D Lift Curve Slope of Airfoil Section
e	Oswald Efficiency Factor
U_p	Vertical Velocity of the Blade
U_T	Horizontal Velocity of the Blade
V_∞	Free-Stream Velocity
ρ	Density of Air
y	Radius of the Blade Section
$dF_{v_{BET}}$	Incremental Thrust Force Found by Blade Element Theory
$dF_{v_{MT}}$	Incremental Thrust Force found by Momentum Theory

CHAPTER 1

INTRODUCTION

1.1 Objective

Accurate prediction of propeller's forces and moments becomes an important role in the high-fidelity design, simulation, and control of aircrafts. Small propellers used on high thrust-to-weight ratio multi-copters and propellers used in VTOL aircrafts which are tilted from hover to forward flight are subjected to varying flight conditions from 0° to 90° propeller disk angles of attack. For this reason, it is important to predict all aerodynamic loads of a propeller under each flight condition such as hovering, vertical climb, and forward flight.

Propeller theories have significantly improved during the last decades that estimate the propeller forces and moments. Before the computational era, the Momentum Theory and the classical Blade Element Theory were common [1, 2]. As the experimental set-ups become more available, parameter estimation methods are thought to be used to identify the relation between forces and moments produced by a propeller and forward flight speed, propeller disk angle of attack, and propeller's angular speed using experimental data obtained from the wind tunnel tests for a given propeller [3-7]. On the other hand, with the advances of computational technology, the CFD methods [8-10] have become a common way in the estimation process of propeller aerodynamics since it is affordable compared to experimental studies. However, to find the optimum propeller for an aircraft, experimental and CFD studies are time-consuming. Also, the classical BET is not applicable in the presence of the free-stream velocity because of some simplifications in the theory due to the lack of computational abilities. Predicting total forces and moments acting on a propeller using only its geometric information through a model-based method using computational advances is more affordable and faster than the wind tunnel/real flight

tests and CFD methods. As well, it is more accurate compared to the classical BET. Using the IBEMT model proposed in this study, look-up tables can be generated for propeller's forces and moments (i.e., aerodynamic loads) at different flight conditions for optimization purposes in a negligible time.

1.2 Literature Review on Propeller Aerodynamics

1.2.1 Blade Element Theory and Momentum Theory

There are several theories to estimate the aerodynamic loads (i.e., forces and moments) of propellers such as Lifting Line Theory, Vortex Lattice Theory, and Panel Method. However, the well-known method that estimates the blade's aerodynamic loads is the classical Blade Element Theory (BET) and the Blade Element Momentum Theory (BEMT) [11-14]. Although it is applicable in hovering flight (i.e., in the absence of free-stream velocity) it fails to approximate the propeller aerodynamic loads accurately in vertical climb and forward flight conditions (i.e., in the presence of free-stream velocity and propeller's disk angle of attack). In the studies conducted by Seddon [12], Fay [13], and Wheatley [14], to predict the total vertical and horizontal forces acting on a blade, the integrals of perpendicular and parallel aerodynamic forces to the rotor disk at each blade section and at each azimuth angle are taken analytically with the help of some simplifications in the classical BET. The whole steps of the integration of the total horizontal and vertical forces and moments are given in [3]. Thrust force is a function of induced velocity as well as rotor speed, free-stream velocity, and propeller disk angle of attack. Therefore, induced velocity plays an important role in the estimation of propeller performance. The well-known theory that models the induced velocity is known as Momentum Theory [11, 12]. Thrust force produced by each annular ring of the rotor disc at each blade section is found both using Momentum Theory and Blade Element Theory separately. The whole step that gives the inflow distribution along the blade by equalizing each thrust found both by BET and Momentum Theory is called Blade

Element and Momentum Theory (BEMT). The reason for making assumptions in the classical BET is to take the integrals over the blade's radius and azimuth angle analytically. However, thanks to the advances in computational technologies these integrals can be evaluated in negligible time using computer programs such as MATLAB® without making simplifications.

In early small-scale multi-copter vehicle developments, the thrust force and the rotor torque of a propeller are assumed to be proportional to the square of its rotation rate, and hub force and rolling moment are ignored [15-21]. However, when the propeller is subject to free-stream velocity and propeller disk angle of attack, the aerodynamic loads produced by it differ from hovering flight. The fidelity of simulations of UAV control systems can be improved using the IBEMT model proposed in this study because it can estimate all forces and moments in all three axes. Besides, propellers can be designed for multi-rotor or fixed-wing UAVs considering the propeller's performance in forward flight. That is, the propeller, selected for a UAV or VTOL aircraft by considering its hovering performance might not be the optimum propeller for forward flight condition. To evaluate the overall performance of such vehicles in their entire flight envelope, a fast and accurate performance estimation model is needed.

1.2.2 Open-Source Tools to Analyze Propeller Performance

Several open-source tools are available for analyses of propeller performance [22-24]. JAVAPROP [22] is a simple tool for the design and analysis of propellers and wind turbines but it has no capability to accurately predict the flow around the propeller. QPROP [23] is an analysis program for predicting the performance of propeller-motor combinations. OPROP's companion program, QMIL, generates propeller geometries for minimum induced loss. QBLADE [25] is an open-source wind turbine calculation software developed at TU Berlin. Because the purpose of QBLADE is the design and aerodynamic simulation of wind turbine blades, an open-source tool called JBLADE is developed for propeller analysis based on QBLADE

and XFLR5, as a Ph.D. study at the Aerospace Sciences Department at the University of Beira Interior [24]. However, these methods [22-25] cannot be modified by the user such as to investigate the effects of the assumptions in the classical BET, to apply a different stall model for the propeller's airfoil or to optimize the propeller's geometry. The IBEMT model allows practical modification for these kinds of purposes.

Most helicopter companies have their own blade element simulation tools. There are also commercial tools for calculating propeller performance like CAMRAD which is designed to calculate rotor performance, loads, noise, helicopter vibration, and gust response [26].

1.2.3 In-House BEMT Models

There are also several in-house BEMT model studies in the literature [27-30]. The aerodynamic performances of four 12in diameter propellers having different geometric properties are investigated at different propeller disk angles of attack varying from 0° to 90° and at different advance ratios ranging from 0 to 0.55 by Serrano et al. [27]. Two Slow Flyers (SF) with pitches 4.7 in/rev and 6 in/rev, and two Sport (SP) models with pitches of 5 in/rev and 6 in/rev are tested by considering their airfoil characteristics, and the wind tunnel tests are performed to a maximum free-stream advance ratio of 0.55 and 0.5 for the SF and SP model propellers, respectively [27]. Since the detailed geometric information and the operating conditions of the tested propellers is available, the IBEMT model is compared with the experimental results given in [27].

Thrust, drag (hub force), and rotor torque (drag moment) of propellers used in the unmanned aerial vehicle (UAV) applications are modeled by using Blade Element Theory (BET), Blade Element Momentum Theory (BEMT), and a parameter fitting procedure to determine aerodynamic parameters by Gill and D'Andrea [28]. Momentum theory is applied to an infinitesimal rotor disk [28, 29]. An iterative

solution is proposed for induced velocity and thrust force, and the wind tunnel measurements are also performed for the validation of the results [28-30]. In [30], 13x6.5in and 13x6in propellers are simulated and results are validated with the wind tunnel measurements. For low angles of attack up to 30° a BEMT model called RotoCalc is developed [30]. By Khan and Nahon [29] a non-uniform model of induced flow is used which is also a function of the azimuth angle. The change of the thrust coefficient with advance ratio are given in axial flow (vertical climb) condition, however, due to the lack of the source of wind tunnel measurements, in oblique flow (forward flight) condition the change of forces and moments with respect to the free-stream velocity or advance ratio is not presented [29].

The originality of this study compared to these mentioned iterative studies is presenting the results of forces and moments with an increasing free-stream velocity at a wide range of propeller disk angles of attack and angular speeds of the propeller. Besides, a more realistic stall model is implemented called AERODAS developed in [31] that increase the accuracy of the BEMT model. The implementation of the stall model affects the results remarkably.

1.3 Contribution

The main contribution of the study is to predict the propeller aerodynamic loads, computationally fast and accurately compared to similar studies found in the literature in all the flight conditions by using a more realistic stall model. The IBEMT model improved here allows quick analyses at various RPMs, free-stream velocities, and propeller disk angles of attack. Sample propeller performance charts are generated and presented in comparison with wind tunnel test results, which are difficult to find in the literature comprehensively. As well, the methodology is explained in detail, and results are presented for a wide range of propeller disk angles of attack and angular speeds of the propeller. Moreover, the effects of the assumptions used in the classical BET are investigated as a contribution. Also, unlike the similar in-house BEMT studies [27-30] the IBEMT model is applied in a

propeller design optimization problem by serving as an input to the optimization for a given flight mission profile. This shows the importance of having an accurate model-based BEMT model for propeller design optimization purposes.

1.4 Structure of the Thesis

CHAPTER 1 consists of the objective, literature survey, and contribution of the thesis. CHAPTER 2 gives a detailed information on the methodology which explains the propeller aerodynamics, identification of the propeller's geometry used in this study and the code generation for the IBEMT model improved in this study. CHAPTER 3 is about the wind tunnel experiments for the validation of the IBEMT model. CHAPTER 4 gives information about the propeller design optimization. CHAPTER 5 presents the results of the study. CHAPTER 6 concludes the thesis with discussions and recommendations.

CHAPTER 2

PROPELLER PERFORMANCE IN HOVER, VERTICAL CLIMB, AND FORWARD FLIGHT

2.1 Propeller Aerodynamics

Forces and moments acting on a fixed-pitch propeller are presented in Figure 2.1. According to the body-fixed reference frame, the direction of thrust force is in the -z_b axis, and the hub force is in the direction of free-stream velocity. The rolling moment occurs due to the advancing and retreating blades see different free-stream velocities. Rotor torque is in the counterclockwise direction when a propeller turns in the clockwise direction. In the presence of free-stream velocity, thrust force, hub force (drag force), rolling moment, and rotor torque (drag moment) occur, and side force and pitching moment equal zero.

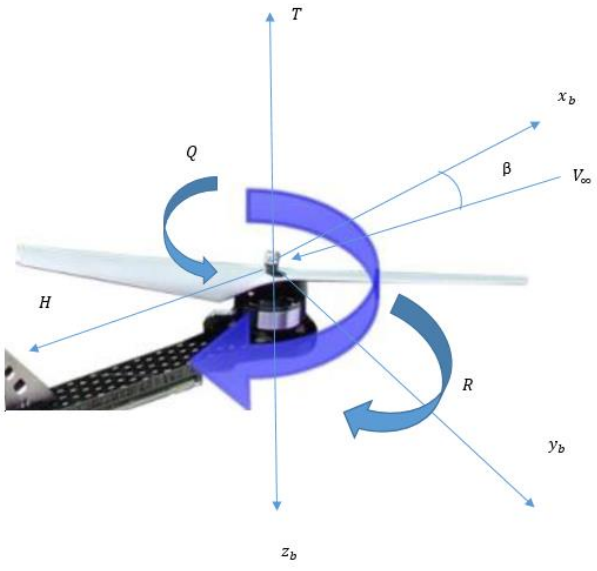

Figure 2.1: Forces and moments acting on a rotor [3].

2.1.1 Blade Element Theory

Blade Element Theory (BET) is a theory that approximately calculates the total forces of a blade by breaking it down into several small parts. These forces are then integrated along the entire blade's radius and azimuth angle to obtain the forces and moments produced by the propeller consisting of different numbers of blades in one revolution.

Total vertical and horizontal forces acting on the center of pressure of the blade is given as follows:

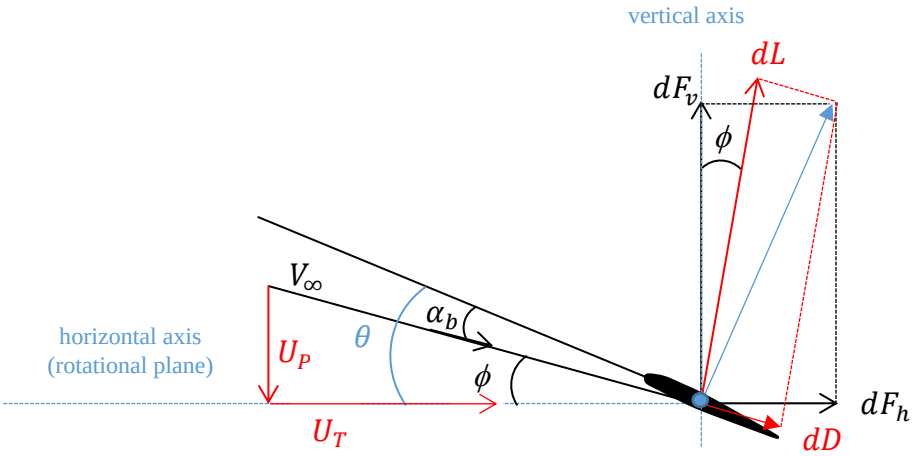

Figure 2.2: Total forces acting on a blade section.

Hint: ● *is the center of pressure of the blade section where the resultant force acts.*

Assumptions used in the classical Blade Element Theory are listed as follows:

1. The blades of the propeller are assumed to be rigid.

2. The lift coefficient of the blade airfoil varies linearly with the blade's angle of attack, α_b.

3. The twist angle, θ, of the blade varies linearly with the radial position, y.

4. The chord length along the radius is assumed constant.

5. Lift acting on a blade has at least one order of magnitude greater than drag so that contribution of drag force, dD, is negligible in the calculation of thrust force.

6. The local inflow angle, ϕ, is assumed very small.

7. Only lift and drag forces are assumed to act on the blade section.

8. Flow is assumed inviscid and incompressible.

By using the assumptions mentioned above, the analytical results, which is known as the classical BET results are presented in Table 2.1:

Table 2.1: Analytical results of the classical BET [3].

Thrust force	$T = \left(\frac{1}{6}\rho A\sigma a\theta_0 \mathrm{R}^2 + \frac{1}{8}\sigma a\rho A\theta_{tw}\mathrm{R}^2\right)\Omega^2 + \left(\frac{1}{4}\rho A\sigma a\theta_0 + \frac{1}{8}\sigma a\rho A\theta_{tw}\right)(V_\infty \cos\alpha)^2 + \left(-\frac{1}{4}\sigma a\rho A\mathrm{R}\right)\Omega(V_\infty \sin\alpha + \mathrm{v_i})$
Hub force	$H = \left(\frac{1}{4}\rho A\sigma\overline{C_d}\mathrm{R}\right)(\Omega V_\infty \cos\alpha) + \left(\frac{1}{4}\rho A\sigma a\left(\theta_0 + \frac{\theta_{tw}}{2}\right)\right)V_\infty \cos\alpha\,(\mathrm{v}_i + V_\infty \sin\alpha)$
Side force	$Y = 0$
Rotor torque	$Q = \Omega^2\left(\frac{1}{8}\rho A\sigma\overline{C_d}\mathrm{R}^3\right) + (V_\infty \cos\alpha)^2\left(\frac{1}{8}\rho A\sigma\mathrm{R}\overline{C_d}\right) + (\Omega \mathrm{v}_i)\left(\frac{1}{4}\sigma a\rho A\theta_0\mathrm{R}^2 + \frac{1}{8}\rho A\sigma a\theta_{tw}\mathrm{R}^2\right) + (\Omega V_\infty sin\alpha)\left(\frac{1}{4}\sigma a\rho A\theta_0\mathrm{R}^2 + \frac{1}{8}\rho A\sigma a\theta_{tw}\mathrm{R}^2\right) + (\mathrm{v}_i + V_\infty \sin\alpha)^2\left(-\frac{1}{4}\sigma a\rho A\mathrm{R}\right)$
Rolling moment	$R = (\Omega V_\infty \cos\alpha)\left(-\frac{1}{6}\sigma a\rho A\theta_0\mathrm{R}^2 - \frac{1}{8}\rho A\sigma a\theta_{tw}\mathrm{R}^2\right) + (\mathrm{v}_i V_\infty \cos\alpha)\left(\frac{1}{8}\sigma a\rho A\mathrm{R}\right) + (V_\infty \cos\alpha \sin\alpha)\left(\frac{1}{8}\sigma a\rho A\mathrm{R}\right)$
Pitching moment	$P = 0$

The aerodynamic performance of the propeller varies according to the propeller disk A.o.A., α, in the presence of the free-stream velocity. As a result, the accurate prediction of the aerodynamic loads of the propeller considering its A.o.A. and free-

stream velocity becomes crucial to get a high-fidelity simulation of the propeller in all flight conditions. However, the classical BET contains different assumptions given above some of which could lead to an unacceptable prediction of the propeller performance. In this study, to get a more realistic model of propeller aerodynamics, the classical BET is improved by removing assumptions 2-6. Besides, instead of using an average value of drag coefficient, $\overline{C_d}$, the AERODAS model that covers post-stall regions as well is used for both the drag and lift coefficients [31]. In addition, the induced velocity is calculated iteratively at each annulus of the rotor disc to improve the classical BEMT.

Relative flow reaches propeller with angles α and β. The azimuth angle is defined with respect to y_B axis as shown in Figure 2.3:

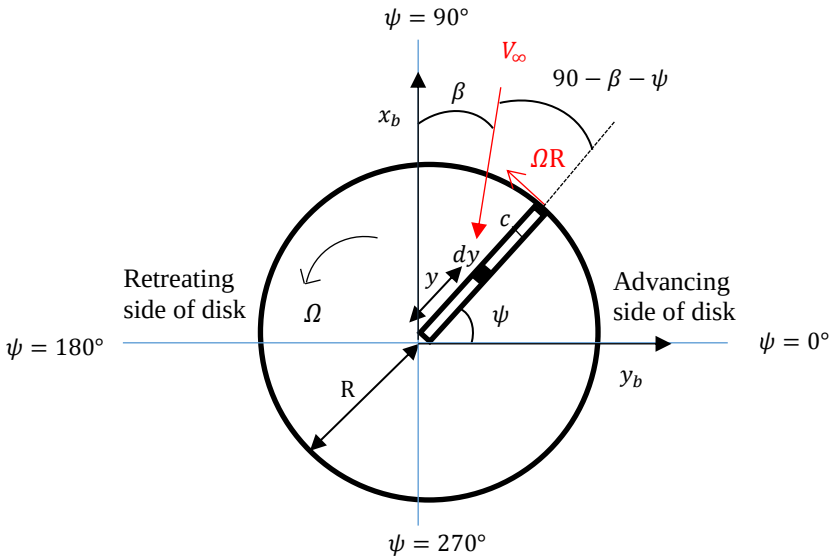

Figure 2.3: Rotor disk view from above.

The direction of the velocity components according to the propeller disk A.o.A. are given in Figure 2.4:

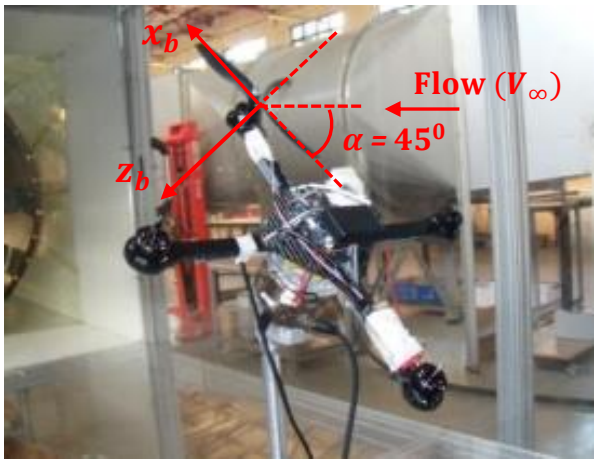

Figure 2.4: Directions of velocities for a propeller in forward flight.

In this study, $\alpha = 90^o$ corresponds to the vertical climb condition where the free-stream velocity is normal to the rotor disk as shown in Figure 2.5:

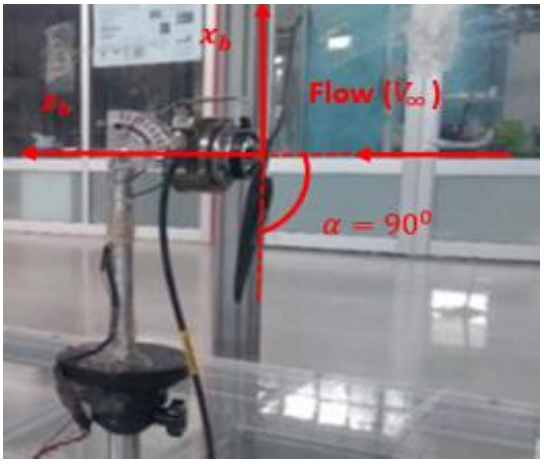

Figure 2.5: Directions of velocities for a propeller in vertical climb.

The condition for no free-stream velocity is referred to as the hovering flight. The terminology adapted for flight conditions assumes a VTOL multi-copter and are defined as shown in Table 2.2:

Table 2.2: Definitions of the flight conditions in this study.

Flight condition	α (°)	V_∞
Hovering flight	undefined	0
Forward flight	$0 \leq \alpha \leq 180$	> 0
Vertical climb	90	> 0
Vertical descend	-90	> 0

The propeller disk angle of attack, α, is different from that of drones, helicopters, and fixed-wing aircrafts that are powered with propellers. In a helicopter, α changes from 0^o to approximately 10^o. On the other hand, in a fixed-wing aircraft powered with a propeller, it changes from 80^o to 90^o. Drones are subjected to varying A.o.A. from 0^o to 180^o. Hence, modeling the post-stall region becomes important in the estimation of the propeller's aerodynamic loads.

Component of the airflow in the rotor disk plane, and perpendicular to the leading edge is given as:

$$V_h(V_\infty, \alpha, \beta, \psi) = V_\infty \cos\alpha \cos(\beta + \psi) \tag{2.1}$$

Component of the airflow perpendicular to the rotor disk plane is given as:

$$V_v(V_\infty, \alpha) = V_\infty \sin\alpha \tag{2.2}$$

Then total vertical velocity is written as follows:

$$U_P = v_i(\Omega, V_\infty) + V_v = v_i(\Omega, V_\infty) + V_\infty \sin\alpha \tag{2.3}$$

The horizontal component of the local resultant velocity at the blade section at distance y from the center is as follows:

$$U_T = \Omega y + V_\infty \cos\alpha \cos(\beta + \psi) \tag{2.4}$$

Airflow magnitude for blade section is written as:

$$V_b(V_\infty, \alpha, \beta, \Omega, y, \psi) = \sqrt{{U_P}^2 + {U_T}^2} \tag{2.5}$$

Figure 2.2 is used as a reference to writing the blade section's lift and drag force:

$$dL\,(y, \psi) = \frac{1}{2}\rho\big(V_b(V_\infty, \alpha, \beta, \Omega, y, \psi)\big)^2 C_l c(y) dy \tag{2.6}$$

$$dD(y, \psi) = \frac{1}{2}\rho\big(V_b(V_\infty, \alpha, \beta, \Omega, y, \psi)\big)^2 C_d c(y) dy \tag{2.7}$$

where $c(\mathrm{y})dy$ is the reference area, S, of the blade section.

Having found the lift and drag forces for each blade section, the aerodynamic force perpendicular to the rotor disk can be written from Figure 2.2 as:

$$dF_v(y, \psi) = dL(y, \psi)\cos\phi - dD(y, \psi)\sin\phi \tag{2.8}$$

The horizontal force on the blade section at each azimuth angle is:

$$dF_h(y, \psi) = dL\,(y, \psi)\sin\phi + dD\,(y, \psi)\cos\phi \tag{2.9}$$

Blade section's angle of attack is written as follows:

$$\alpha_b(V_\infty, \alpha, \beta, \Omega, y, \psi) = \theta(y) - \phi \tag{2.10}$$

$$\alpha_b(V_\infty, \alpha, \beta, \Omega, y, \psi) = \theta(y) - \tan^{-1}\left(\frac{v_i + V_v}{\Omega y + V_h}\right) \tag{2.11}$$

Linear twist assumption (assumption 3) made in the classical BET is as follows:

$$\theta(y) = \theta_0 - y\theta_{tw} \tag{2.12}$$

The methodology of finding α_b, $c(\mathrm{y})$, and $\theta(y)$ are explained in section 2.1.3.

The boundaries of the blade section are as follows:

$$\mathrm{R}_0 \leq y \leq \mathrm{R} \tag{2.13}$$

where R_0 is the hub radius of the propeller.

The boundaries of the azimuth angle are as follows:

$$0 \leq y \leq 2\pi \tag{2.14}$$

To calculate the total vertical force (i.e., thrust) produced by the rotor in one revolution of the blade, the aerodynamic force perpendicular to the rotor disk is integrated along the blade section and azimuth:

$$T = \iint dF_v(y, \psi) dy d\psi \tag{2.15}$$

Both the induced velocity and thrust are unknowns at this point. In this section, the thrust produced by the rotor is derived using the BET which depends on the induced velocity. Thrust force will also be derived using Momentum Theory, in Section 2.1.2. The two results allow us to solve for induced velocity and rotor thrust iteratively.

2.1.2 Momentum Theory

Momentum Theory is used to find the thrust force of the rotor disc and induced velocity. The theory is based on conservation laws of fluid mechanics called mass, momentum, and energy conservation of fluids (i.e., air) to calculate the force exerted on a rotor. Based on the sources [11, 12], the following assumptions have been made in order to derive the induced velocity:

1. Flow is inviscid, incompressible, and quasi-steady.

2. There is no discontinuity in velocity and the flow is one-dimensional.

3. Disc is infinitesimally thin and pressure is uniformly spread.

4. Induced velocity is assumed to be uniform at all points on the disc.

5. There is an infinite number of blades, hence the rotor can be thought of as a circular disc.

Airflow through rotor disc is illustrated as follows:

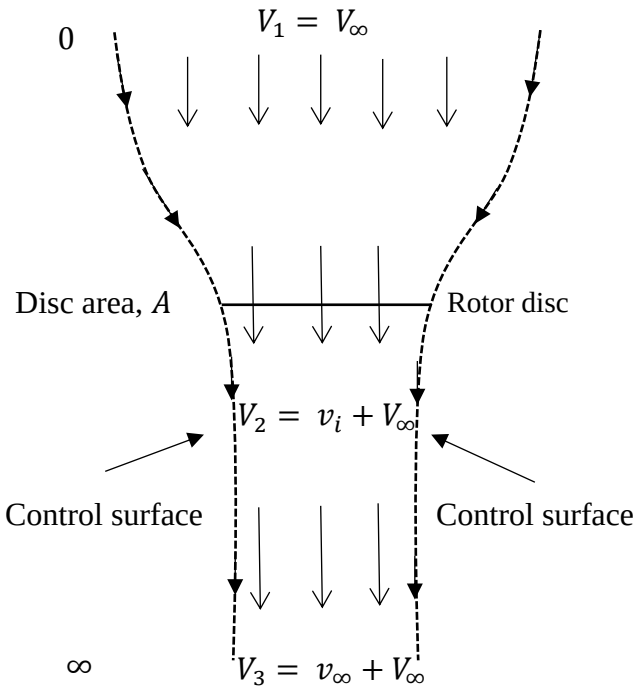

Figure 2.6: Airflow through rotor disc in hovering and vertical climb.

Because the flow is assumed quasi-steady, by the principle of conservation of mass, the mass flow rate is constant within the control volume [11]. Therefore, the mass flow rate is written as follows:

$$\dot{m} = \oiint \rho \overrightarrow{V_2} . d\vec{S} = \rho A(\mathrm{v}_i + V_\infty) \tag{2.16}$$

In hovering flight $V_\infty = 0$, then the above equation is rewritten as follows:

$$\dot{m} = \rho A \mathrm{v}_i \tag{2.17}$$

According to the conservation of momentum, the thrust produced by a rotor moving along its axis at a speed is equal to the rate of mass flow through the disc times velocity of the air after it passes through the rotor:

$$T = \oiint \rho(\overrightarrow{V_3}.d\vec{S}).\overrightarrow{V_3} - \oiint \rho(\vec{V}_1.d\vec{S}).\vec{V}_1 = \dot{m}\Delta V \tag{2.18}$$

where $\Delta V = V_3 - V_1 = (v_\infty + V_\infty) - V_\infty$, perpendicular velocity to the rotor disc.

The rotor thrust is equal and opposite to the force on the fluid, which is given by as follows:

$$T = \dot{m}v_\infty \tag{2.19}$$

By inserting Equation (2.17) into Equation (2.19), the following relation is obtained:

$$T = \rho A \mathrm{v}_i v_\infty \tag{2.20}$$

By using the principle of conservation of energy, the work done on the rotor (power consumed by the rotor, $T\mathrm{v}_i$) is equal to the gain in energy of the fluid per unit of time [11].

$$T\mathrm{v}_i = \oiint \frac{1}{2}\rho(\overrightarrow{V_3}.d\vec{S}).\left|\overrightarrow{V_3}\right|^2 - \oiint \frac{1}{2}\rho(\vec{V}_1.d\vec{S}).\left|\overrightarrow{V_1}\right|^2 \tag{2.21}$$

Since $V_\infty = 0$, the second term of the right-hand side of the above equation drops:

$$T\mathrm{v}_i = \oiint \frac{1}{2}\rho(\overrightarrow{V_3}.d\vec{S}).\left|\overrightarrow{V_3}\right|^2 = \frac{1}{2}\dot{m}{v_\infty}^2 \tag{2.22}$$

By inserting Equation (2.17) and Equation (2.20) to Equation (2.22), the following relation is obtained:

$$(\rho A \mathrm{v}_i v_\infty)\mathrm{v}_i = \frac{1}{2}\rho A \mathrm{v}_i {v_\infty}^2 \tag{2.23}$$

Then, the following relation is obtained from Equation (2.23):

$$v_\infty = 2v_i \tag{2.24}$$

Thrust force can be formulated as:

$$T = \rho A \mathrm{v}_i v_\infty = 2\rho A \mathrm{v}_i{}^2 \tag{2.25}$$

Induced velocity is found as follows when $V_\infty = 0$, which is known as hovering flight:

$$v_i = \sqrt{\frac{T}{2\rho A}} \tag{2.26}$$

Similar equations can be derived as follows for vertical climb flight, where $V_\infty > 0$. Thrust expression in vertical climb flight is expressed as follows:

$$T = \rho A \mathrm{v}_\infty (V_\infty + \mathrm{v}_i) = 2\rho A \mathrm{v}_i (V_\infty + \mathrm{v}_i) \tag{2.27}$$

Then, the above equation is formed as:

$$\mathrm{v}_i{}^2 + \mathrm{v}_i V_\infty - \frac{T}{2\rho A} = 0 \tag{2.28}$$

The roots of Equation (2.28) are found as:

$$\mathrm{v}_{i_{1,2}} = -\frac{V_\infty}{2} \pm \sqrt{\left(\frac{V_\infty}{2}\right)^2 + \left(\frac{T}{2\rho A}\right)} \tag{2.29}$$

The positive root of Equation (2.29) is valid for induced velocity expression in vertical climb condition:

$$\mathrm{v}_i = -\frac{V_\infty}{2} + \sqrt{\left(\frac{V_\infty}{2}\right)^2 + \left(\frac{T}{2\rho A}\right)} \tag{2.30}$$

The aerodynamics of the rotor in forward flight is more complex than the hovering and vertical flights because α is different from 0° or 90°. The directions of the velocities are shown in Figure 2.7:

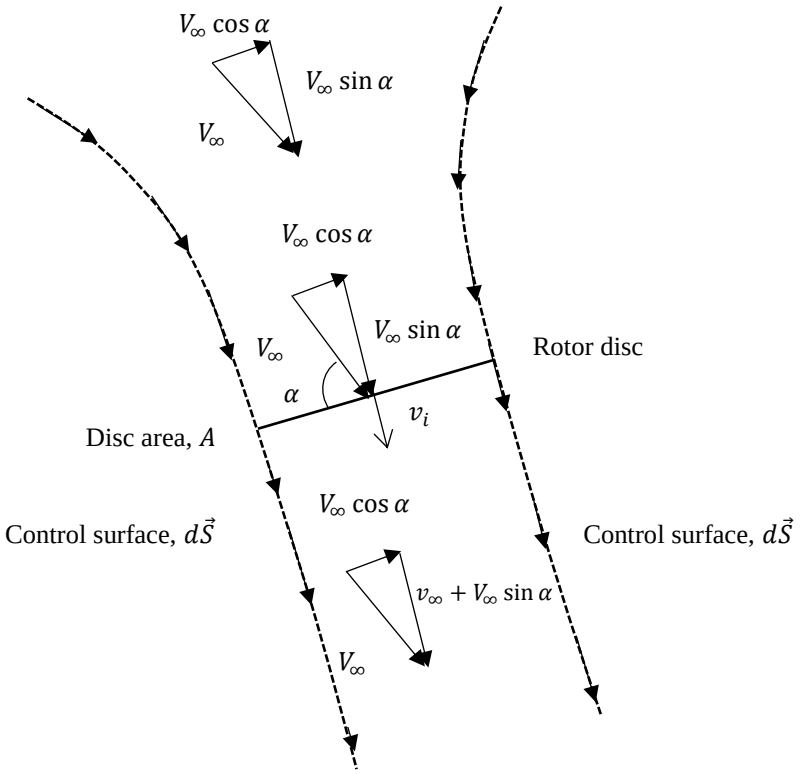

Figure 2.7: Airflow through rotor disc in forward flight.

$$\dot{m} = \rho A\sqrt{(V_\infty \sin\alpha + \mathrm{v}_i)^2 + (V_\infty \cos\alpha)^2} \tag{2.31}$$

where

$$\Delta V = \mathrm{v}_\infty + V_\infty \sin\alpha - V_\infty \sin\alpha = \mathrm{v}_\infty = 2\mathrm{v}_i$$

$\dot{m}$ expressed in Equation (2.31) is inserted in Equation (2.19), where $\Delta V = 2\mathrm{v}_i$, the following relation is found:

$$T = \rho A \left(\sqrt{(V_\infty \sin\alpha + \mathrm{v}_i)^2 + (V_\infty \cos\alpha)^2}\right)(2\mathrm{v}_i) \qquad (2.32)$$

In equations (2.26) and (2.30), induced flow through the entire disk is assumed to be uniform in hover and vertical climb conditions, respectively. Considering that the angle of attack along the span direction can change significantly, uniform induced velocity assumption is a limiting factor for the model's accuracy. One of the improvements we incorporate into our model is to make induced velocity vary along the span. We achieve this by repeating the analysis shown above for the entire disk on an annulus with radius y and infinitesimal width dy, as shown in Figure 2.8.

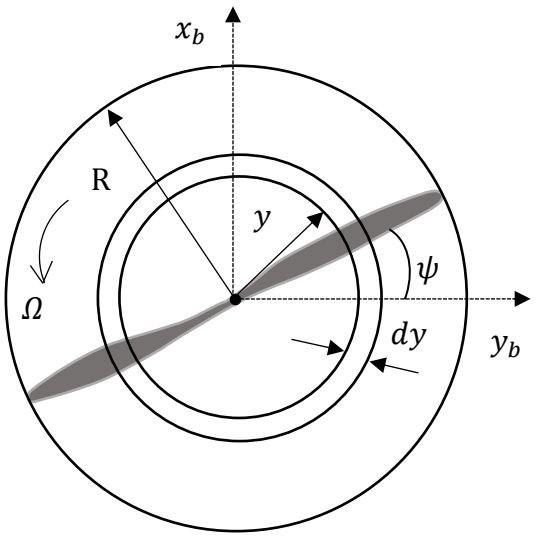

Figure 2.8: Annulus of rotor disc from top view.

The successive rotor annuli are assumed to have no mutual effects on each other.

Induced velocity derived using Momentum Theory for forward flight condition at each blade section with a section area $A = 2\pi y dy$ is as follows:

$$dF_{v_{MT}}(y) = \rho(2\pi y dy)\left(\sqrt{(V_\infty \sin\alpha + \mathrm{v}_i)^2 + (V_\infty \cos\alpha)^2}\right)(2\mathrm{v}_i) \qquad (2.33)$$

Rearranging Equation (2.33), the final expression of thrust force at each blade section found by Momentum Theory is obtained in Equation (2.34):

$$dF_{v_{MT}}(y) = 4\rho\pi y dy \mathrm{v}_i(y)\sqrt{\left(V_\infty \sin\alpha + \mathrm{v}_i(y)\right)^2 + (V_\infty \cos\alpha)^2} \qquad (2.34)$$

Equation (2.26) and Equation (2.30) can be evaluated analytically. Yet, the roots of $\mathrm{v}_i(y)$ in Equation (2.34) cannot be found analytically unlike in hovering and vertical flight conditions. Besides, in Momentum Theory, it is seen that the induced velocity depends on thrust force (i.e., the left-hand side of Equation (2.34)). Also, in Blade Element Theory (Equation (2.36)), the thrust force is a function of induced velocity (See Equation (2.3)). Therefore, during the solution of these equations, an iterative method is conducted, which satisfies (2.35), to find the induced velocity at each blade section.

$$dF_{v_{MT}}(y) = dF_{v_{BET}}(y) \qquad (2.35)$$

where $dF_{v_{BET}}(y)$ is the thrust force at one blade section, dy, along the azimuth from 0 to 2π (i.e., thrust force of annular ring of the rotor disc in Figure 2.8) found by BET, and expressed as follows:

$$dF_{v_{BET}}(y) = \frac{N}{2\pi}\left(\int_0^{2\pi} dL(y,\psi)\cos\phi - dD(y,\psi)\sin\phi\right)d\psi \qquad (2.36)$$

By equalizing $dF_{v_{BET}}(y)$ obtained from BET (Equation(2.36)) to the $dF_{v_{MT}}(y)$, in Equation (2.34) , Equation (2.37) is obtained:

$$dF_{v_{BET}}(y) - 4\rho\pi y dy \mathrm{v}_i(y)\sqrt{\left(V_\infty \sin\alpha + \mathrm{v}_i(y)\right)^2 + (V_\infty \cos\alpha)^2} = 0 \quad (2.37)$$

The reason is to solve Equation (2.37) iteratively is that because $dF_{v_{BET}}(y)$ expressed in Equation (2.36) also contains $\mathrm{v}_i(y)$ it can be seen in Equation (2.3), which is used in finding the total velocity, V_b, in sectional lift, dL (Equation (2.6)). The sectional lift contains induced velocity due the vertical component of V_b which is denoted as U_P. Besides blade's A.o.A., α_b contains v_i as well as U_P as it can be seen in Equation (2.11). Therefore, the numerical solution continues until the thrust evaluated by Momentum Theory and the thrust found by BET converge. After solving the roots of Equation (2.37) numerically, the induced velocity, v_i, is found. Then using this induced velocity found iteratively, the Euler integration is conducted for all blade sections from 0 to radius, R:

$$T = F_v = \int_0^{\mathrm{R}} dF_{v_{BET}}(y) \quad (2.38)$$

Total horizontal forces at each annular ring of rotor disc is as follows:

$$dF_{h_{BET}}(y) = \frac{N}{2\pi}\int_0^{2\pi} dF_h(y,\psi)d\psi \quad (2.39)$$

Resultant horizontal forces (hub force) along the azimuth and radius is as follows:

$$H = F_h = \int_0^{\mathrm{R}} dF_{h_{BET}}(y) \quad (2.40)$$

Force due to blade section in the x_B direction (component of the hub force in the x_B direction) is given as follows:

$$dF_{xB} = -dF_h \cos\psi \tag{2.41}$$

Force due to blade section in the y_B direction (component of the hub force in the y_B direction) is:

$$dF_{yB} = dF_h \sin\psi \tag{2.42}$$

Moment due to blade section in the z_B direction (rotor torque, Q) is:

$$dM_{zB} = dF_h y \tag{2.43}$$

Moment due to blade section in the x_B direction (rolling moment, R) is:

$$dM_{xB} = -dF_v y \cos\psi \tag{2.44}$$

Moment due to blade section in the y_B direction (pitching moment, P) is:

$$dM_{yB} = dF_v y \sin\psi \tag{2.45}$$

2.1.3 Identification of the Propeller's Geometry

If the distribution of the chord length and pitch angle along the blade is known, they can be used directly. However, if the detailed model is not available, chord and pitch distributions of the propeller can be roughly obtained from a high-resolution photograph. The twist angle and chord length distribution of the tested airfoil are identified from the photographs of the airfoil given in Figure 2.9 and Figure 2.10. The distance marked as Δh in Figure 2.10 is the projection of the chord length in the rotor disk, given as $c\cos\theta$. Projection of the chord length in the plane normal to rotor disk plane is marked as $\Delta v = c\sin\theta$ in Figure 2.9. The leading edge of the

propeller can be clearly seen in Figure 2.9. The vertical distance between the leading and trailing edges are measured as Δv in Figure 2.9.

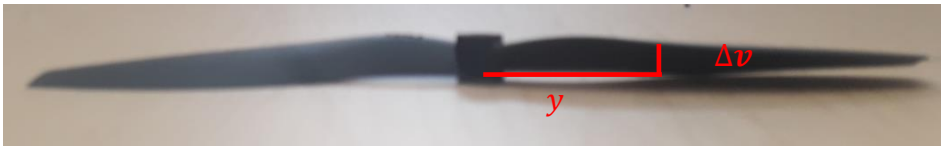

Figure 2.9: Side view of the 8x4.5in propeller.

Figure 2.10: Top view of the 8x4.5in propeller.

Using the horizontal and vertical projections of the chord line, pitch angle of the blade at distance y can be found as:

$$\theta(y) = \tan^{-1}\frac{\Delta v}{\Delta h} \tag{2.46}$$

The twist and the chord distributions along the radius of 8x4.5in propeller are given in Figure 2.11 and Figure 2.12, respectively:

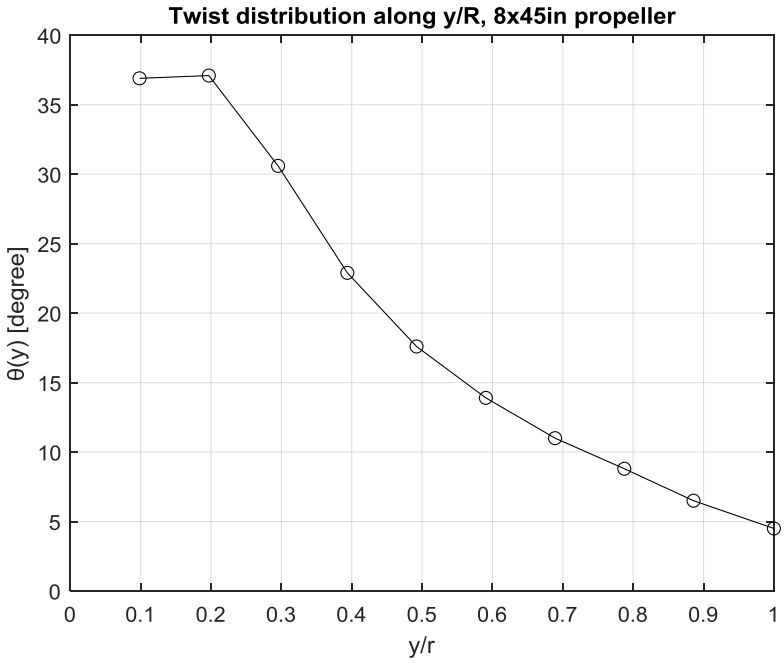

Figure 2.11: Change of the twist along the radius of 8x4.5in propeller.

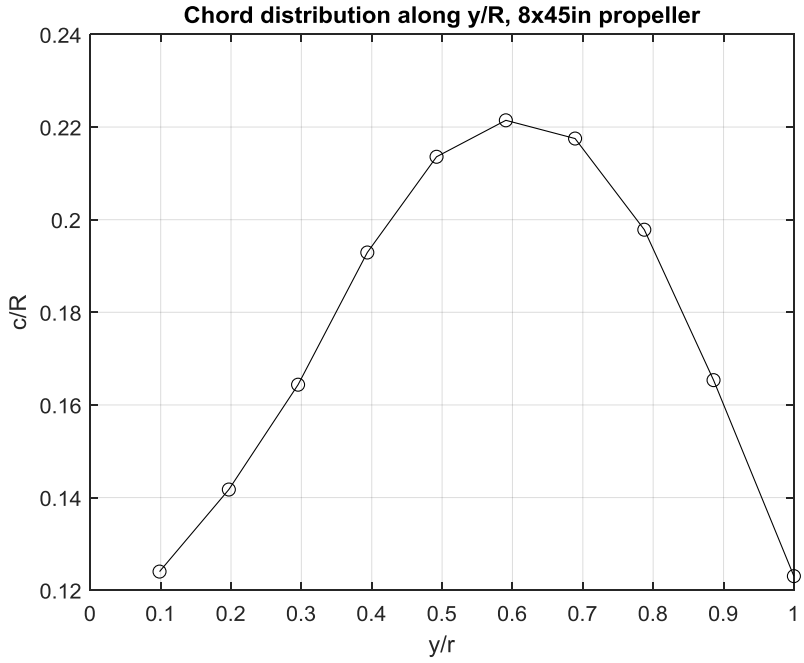

Figure 2.12: Change of chord length along the radius of 8x4.5in propeller.

Measurements from the photographs are taken in terms of pixels. The diameter of the propeller is measured as 3380 pixels in Figure 2.10. The actual diameter is measured as 20.32 cm using a caliper, which gives a pixel size of 0.00601 cm. Projections of the chord length in the rotor disk at various blade sections are measured both from the photograph and the actual propeller by using a caliper. Results are given in Table 2.3 with an average error of 2 %. This gives us confidence in using the twist angle measurements from the photographs in our model, as we cannot measure twist angle using a caliper.

Table 2.3: Chord measurements at each blade section using the photograph and a caliper.

y (pixel)	y (cm)	Chord measured by photograph (pixel)	Chord measured by photograph (cm)	Chord measured by using a calliper (cm)
169	1.016	209.6506	1.26	1.30
338	2.032	239.6007	1.44	1.45
507	3.048	277.8702	1.67	1.65
676	4.064	326.1231	1.96	1.95
845	5.080	361.0649	2.17	2.15
1014	6.096	374.3760	2.25	2.20
1183	7.112	367.7205	2.21	2.15
1352	8.128	334.4426	2.01	1.95
1521	9.144	279.5341	1.68	1.65
1690	10.160	207.9867	1.25	1.22

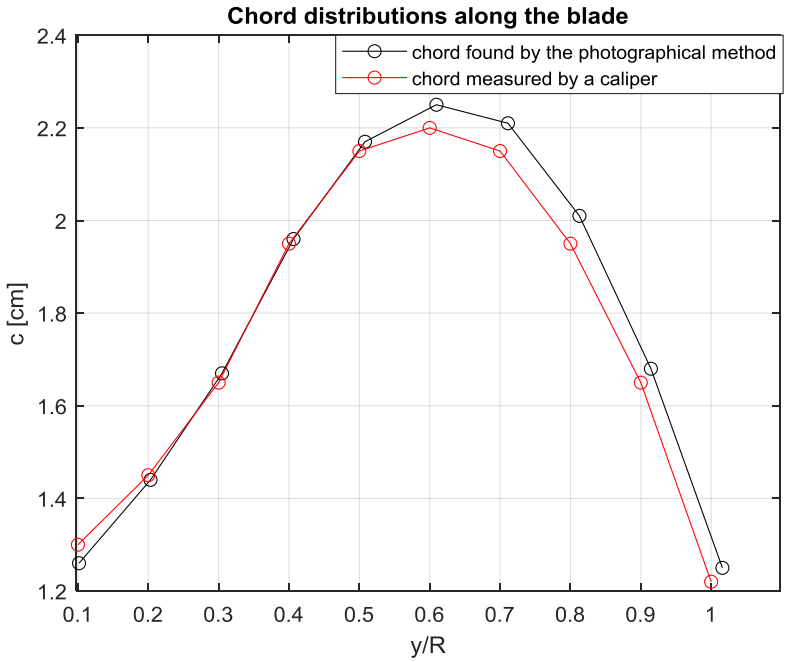

Figure 2.13: Comparison of the chord length measurements.

The photographic method meets the requirements for the calculation of the twist and chord distribution along the radius. However, because a more developed model of the pre-stall and post-stall characteristics of the airfoil is used, it is decided that the propeller should be cut in order to identify its airfoil. The propeller is cut in every 1 cm by a laser cutting machine as can be seen in Figure 2.14:

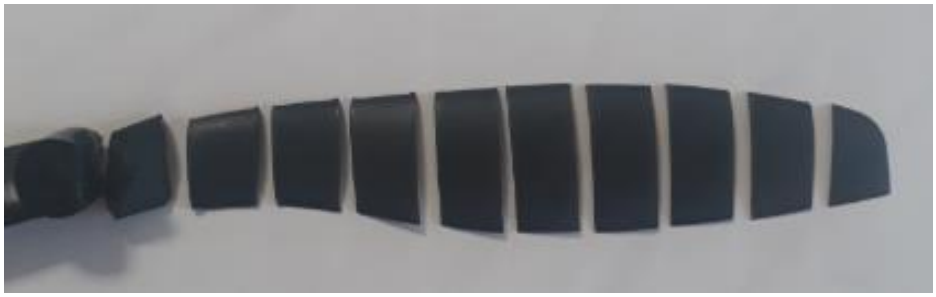

Figure 2.14: 8x4.5 in propeller after cut.

The airfoil of the propeller shown in Figure 2.15 for which test data is available is found by cutting it using a laser cutting machine.

Figure 2.15: Airfoil of the propeller.

The airfoil has a maximum thickness and camber of 7% and 9% that occur at 22% and 35% along the chord, respectively. The inputs of the AERODAS stall model given in Table 2.4 for the airfoil shown in Figure 2.15 are obtained from [50].

2.1.4 Variation of Lift and Drag Coefficients of Airfoil with Blade's Angle of Attack

The lift coefficient is usually assumed to change linearly with α_b which is quite reasonable when the airfoil's angle of attack is in the non-stall region.

$$C_l(V_\infty, \alpha, \beta, \Omega, y, \psi) = a\alpha_b \tag{2.47}$$

where a is the lift curve slope which is usually taken as 2π. The drag coefficient is assumed to be a function of lift coefficient:

$$C_d(V_\infty, \alpha, \beta, \Omega, y, \psi) = C_{d0} + KC_l^2 \tag{2.48}$$

$$K = \frac{1}{\pi \boldsymbol{AR} e} \tag{2.49}$$

The aspect ratio, $\boldsymbol{AR}$, is expressed as follows:

$$\boldsymbol{AR} = \frac{\mathrm{R}}{\overline{c}} \tag{2.50}$$

Equation (2.47) and Equation (2.48) do not include stall phenomena. In the classical BET, in the calculation of C_l value, Equation (2.47) is employed (assumption 2) and an average value of C_d is used as $\overline{C_d}$ in order to be able to take the integrals over

the blade section and azimuth angle analytically (See Table 2.1 for the analytical results). Yet, the linear assumption of the lift coefficient causes inaccurate prediction of the propeller forces and moments when the blade's A.o.A. is in the stall region, especially in thrust calculations. Besides, $\overline{C_d}$ causes inaccurate estimation of propeller aerodynamic loads such as rotor torque and hub force which are highly dependent on drag force. Therefore, a brief literature review is conducted for the variation of lift and drag coefficients with blade's A.o.A., α_b, in both pre-stall and post-stall regions.

A sigmoid function is used to approximate an airfoil's stall effect by Gill and D'Andrea [28]:

$$\sigma = \frac{1 + e^{-M(\alpha-\alpha_0)} + e^{M(\alpha+\alpha_0)}}{(1 + e^{-M(\alpha-\alpha_0)})(1 + e^{M(\alpha+\alpha_0)})} \tag{2.51}$$

Lift and drag coefficients are defined as follows:

$$C_l = (1-\sigma)c_{l_1}\alpha_b + \sigma c_{l_2} \sin\alpha_b \cos\alpha\alpha_b \tag{2.52}$$

$$C_d = C_d(\sin\alpha_b)^2 + 2\frac{1.02c_p}{\sqrt{R_e}} + C_{d0} \tag{2.53}$$

where R_e is the Reynolds Number, and C_d, c_{l_1}, c_{l_2}, c_p, α_0, and M are parameters depending on propeller characteristics.

In the pre-stall region, the linear assumption is used by Khan and Nahon [29]. On the other hand, the model proposed by Horner and Henry [33] is employed in the post-stall region [29]:

$$C_n = C_{d90} \frac{\sin \alpha_b}{(0.56 + 0.44 \sin \alpha_b)} \tag{2.54}$$

$$C_a = 0.5 C_{d0} \cos \alpha_b \tag{2.55}$$

$$C_l = C_n \cos \alpha_b - C_a \sin \alpha_b \tag{2.56}$$

$$C_d = C_n \sin \alpha_b + C_a \cos \alpha_b \tag{2.57}$$

where C_n and C_a are the normal and axial coefficients. The parameters are chosen as follows and results are presented in Figure 2.16:

$a = 2\pi$, $C_{d0} = 0.02$ and $C_{d90} = 1.98$, and the pre-stall region is defined between $-10°$ and 13° angle of attack, α_b.

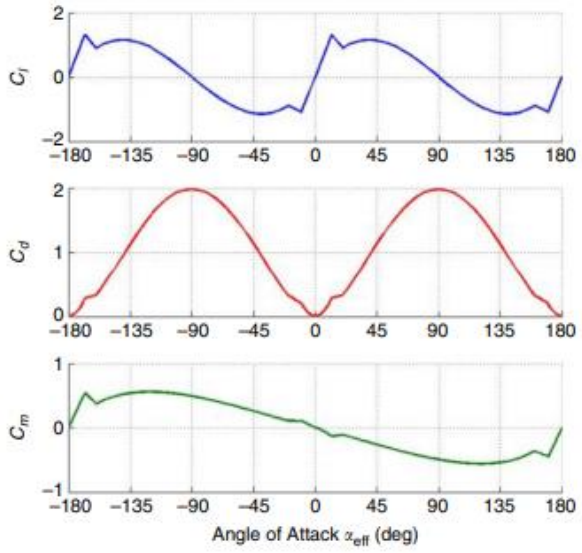

Figure 2.16: Variation of lift, drag, and moment coefficients with blade's A.o.A. using the stall model in the study conducted by Khan and Nahon [29].

A model for predicting lift and drag coefficients of s1210 airfoil for all angles of attack is presented based upon results from wind tunnel tests [34]. However, the parameter estimation is conducted for a specific airfoil (s1210).

A propeller used on a multi-copter vehicle may be subject to high angles of attack, unlike a fixed-wing aircraft propeller during flight conditions where large in-plane flow velocities U_T occur. For a propeller model that can be used for high-fidelity simulation and design of multi-copter vehicles, modeling of blade stall is critical. An empirical model for the variation of the lift and drag coefficients with the blade's angle of attack in pre-stall and post-stall regions proposed by Spera [31] is adopted in this study to model blade stall. Although this model, referred to as the AERODAS model earlier, is developed for wind turbine rotors and fans, it can be used for UAV propellers as well. The empirical model is based on airfoil data in the pre-stall region and some basic geometric properties. Airfoil data that can be found on an airfoil database such as maximum-lift coefficient, A.o.A. that corresponds to the maximum-lift coefficient, A.o.A. that corresponds to zero-lift coefficient, the slope of the linear segment, minimum and maximum drag coefficients, A.o.A. that corresponds to the maximum-drag coefficient in the pre-stall region are used as inputs. Then, the lift and drag coefficients are extended to post-stall regions using basic geometric properties of the blade, thickness ratio, and aspect ratio. The model has been tested and verified with a large quantity of reference test data for a wide variety of airfoil data [31]. The key benefit of the model is that it only needs a few parameters that can readily be found for many airfoils in the literature. Incorporation of the AERODAS model into the IBEMT model allows for evaluation of effects of airfoil

parameters on propeller performance for various conditions and hence selection or even design of propeller airfoil for a specific purpose.

Sample test data and the AERODAS model for lift and drag coefficients are presented in Figure 2.17 and Figure 2.18. The inputs of the AERODAS model for the airfoil used in this study is given in Table 2.4.

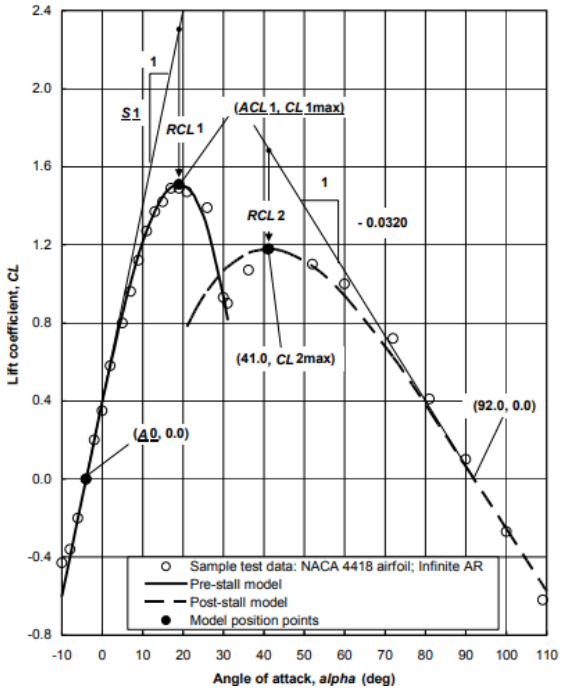

Figure 2.17: Configurations of AERODAS model for calculating lift coefficient in the pre-stall and post-stall regimes [31].

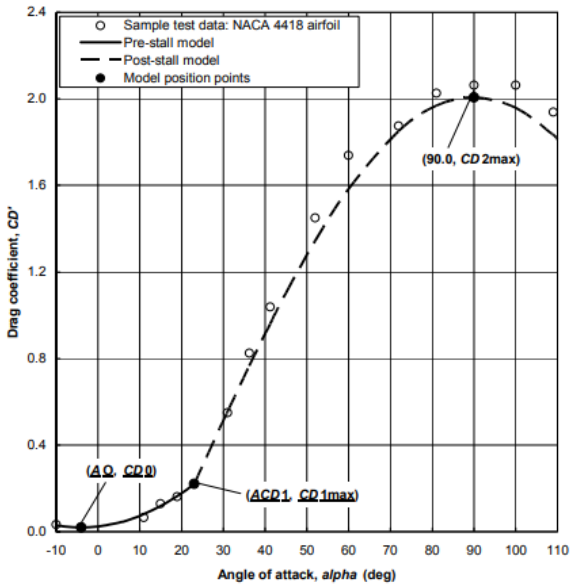

Figure 2.18: Configurations of AERODAS model for calculating drag coefficient in the pre-stall and post-stall regimes [31].

Table 2.4: The airfoil inputs to the AERODAS model obtained from [50].

Inputs	Explanation of the inputs	Values
$\boldsymbol{AR}$	Aspect Ratio	6.5
t/c	Thickness/chord	0.07
A0	Zero-lift A.o.A.	-9.3
ACL1	A.o.A. that corresponds to the maximum lift coefficient in the pre-stall region	11
ACD1	A.o.A. that corresponds to the maximum drag coefficient in the pre-stall region	11.3
S1p	Slope of the linear segment	0.103
Cl1max	Maximum lift coefficient in the pre-stall region	1.86
Cd0	Minimum drag coefficient	0.0065
Cd1max	Maximum drag coefficient in the pre-stall region	0.02
M	An exponent commonly defined as a quadratic equation.	2

Using the AERODAS stall model, lift and drag coefficients are obtained for the airfoil in Figure 2.19 and Figure 2.20, respectively:

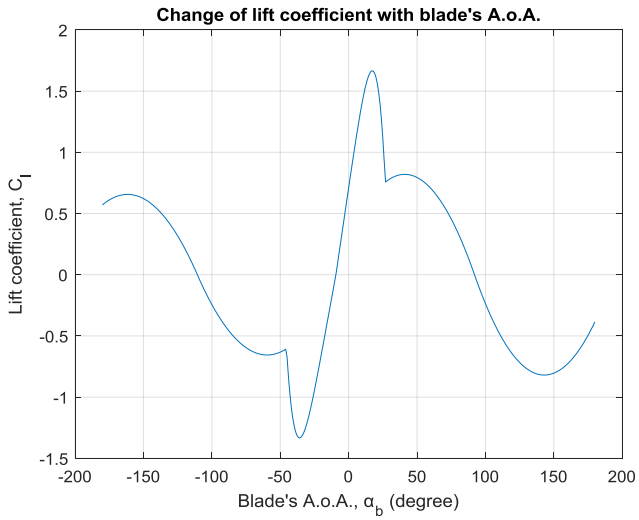

Figure 2.19: Variation of lift coefficient of the airfoil using AERODAS [31].

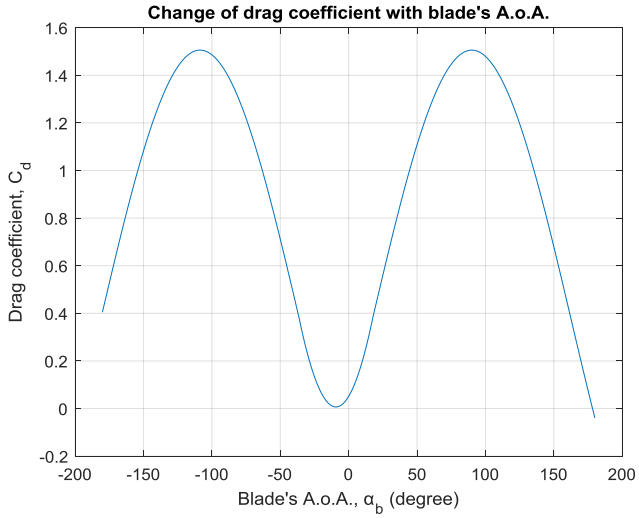

Figure 2.20: Variation of drag coefficient of the airfoil using AERODAS [31].

To compare the stall model results obtained from AERDAS stall model, the airfoil of the propeller is matched with NACA 7209 according to Airfoil Tools [32],

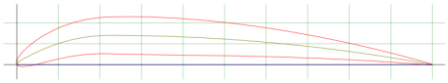

Figure 2.21: Airfoil of the 8x4.5in propeller [32].

Then, the pre-stall and the post-stall model of NACA 7209 is found by JBLADE. The results are given for the lift and drag coefficients in Figure 2.22and Figure 2.23, respectively:

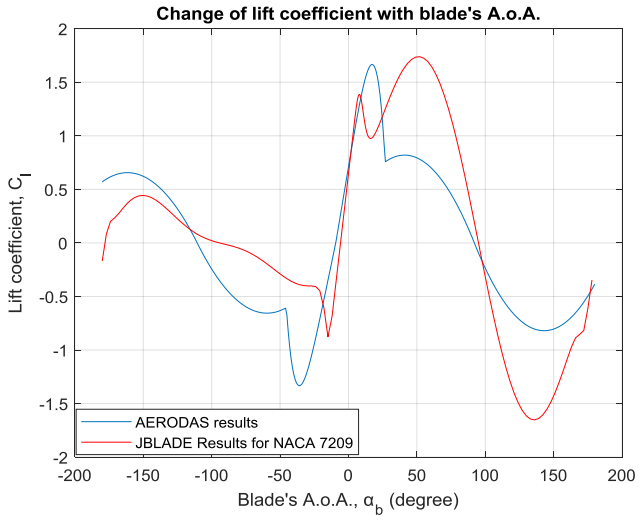

Figure 2.22: Comparison of the variation of lift coefficient of the airfoil.

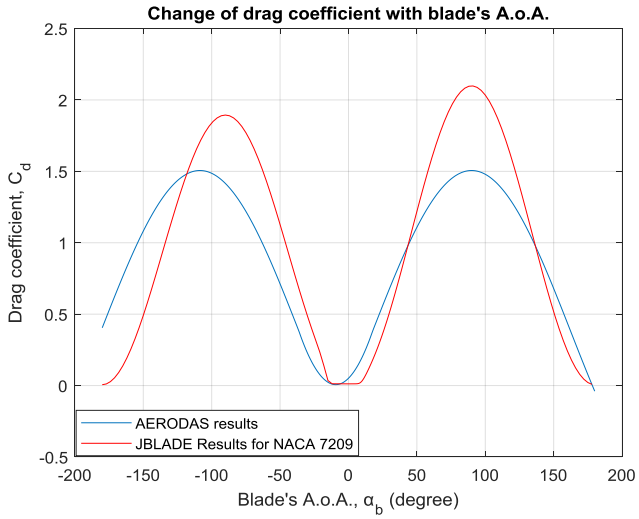

Figure 2.23: Comparison of the variation of drag coefficient of the airfoil.

According to the thickness and camber information, the airfoil in Figure 2.15 is matched with NACA 7209 [32]. The error between the lift and drag coefficients may have been caused by mismatching the airfoil.

2.2 Code Generation and Implementation of IBEMT Model

The schematic representation of the IBEMT model is given in Figure 2.24. The input parameters are the propeller chord length and twist angle distributions along the blade, airfoil parameters, propeller radius, hub radius, and number of blades. The operational parameters are the density of air, propeller's angular speed, propeller disk A.o.A., and the free-stream velocity. The iterations are conducted along the blade radius, y, and azimuth angle, ψ.

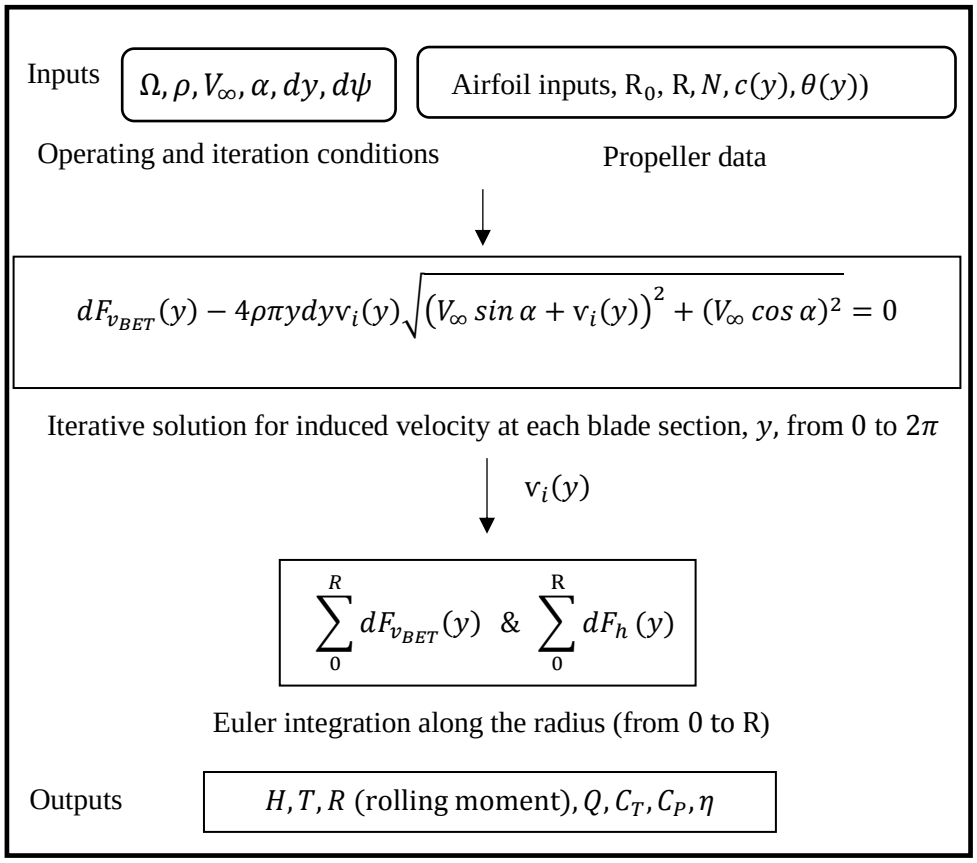

Figure 2.24: Schematic representation of the IBEMT model.

CHAPTER 3

WIND TUNNEL EXPERIMENTS

3.1 Wind Tunnel Facility

The experiments are performed in the open-return suction type wind tunnel of Middle East Technical University (METU) Center for Wind Energy Research (RÜZGEM). The wind tunnel consists of a 2D contraction with a contraction ratio of 1:5, a fully transparent test section with a cross-sectional area of $1x1\ m^2$ and a length of $2\ m$. It is powered by a 45-kW speed-controlled electrical motor, which drives a $1.2\ m$ diameter axial fan. The settling chamber includes a honeycomb and a screen in order to ensure high flow quality inside the test section. Maximum velocity inside the test section is $25\ m/s$ and the average inlet turbulence intensity is about 1 %. The wind tunnel used in the experiments is shown in Figure 3.1:

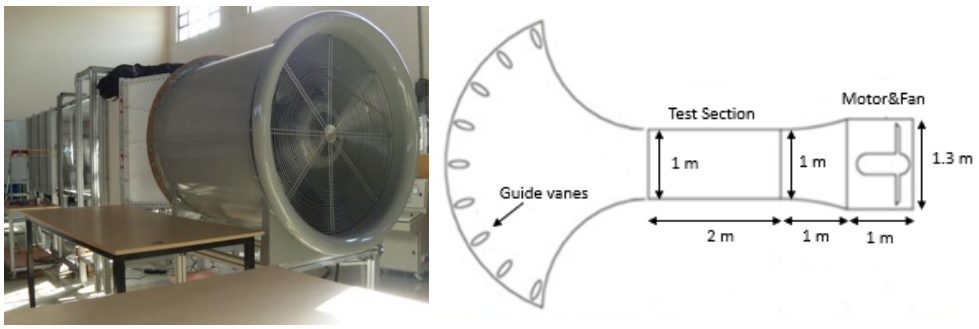

Figure 3.1: Open-return suction type wind tunnel facility.

3.2 Experimental Test Setup

The setup includes a load cell presented in Figure 3.2 to measure total forces and moments on the propeller. Total forces and moments acting on the 8x4.5in propeller are measured using a six-component force/torque transducer (ATI Gamma series). The transducer is shown in Figure 3.2 attached to the support system.

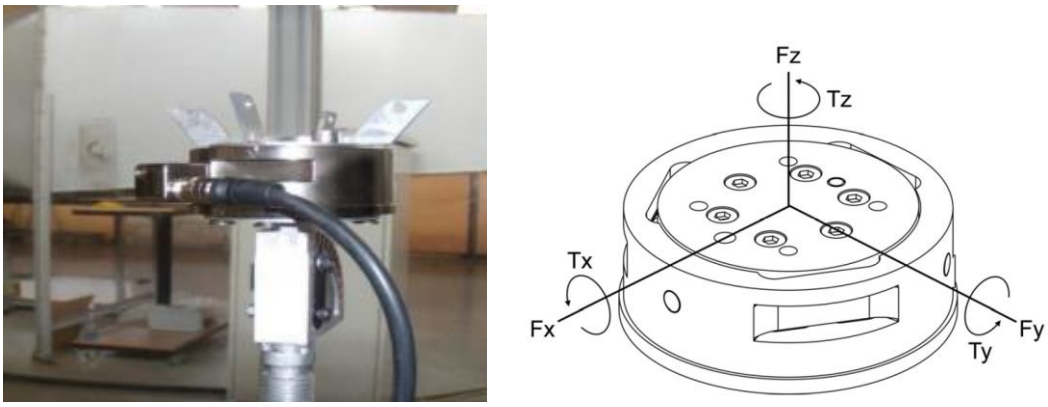

Figure 3.2: Six-component Force/Torque transducer.

The measurement ranges and uncertainties of the transducer along the 3 axes are given in Table 3.1:

Table 3.1: Measurement ranges and uncertainty of the transducer.

	F_x	F_y	F_z	T_x	T_y	T_z
Calibrated Ranges	$\pm 32\ N$	$\pm 32\ N$	$\pm 100\ N$	$\pm 2.5\ Nm$	$\pm 2.5\ Nm$	$\pm 2.5\ Nm$
Uncertainty	0.75%	0.75%	0.75%	1.00%	1.25%	1.50%

Since the rotor torque, hub force, and rolling moment are less than at least one order of magnitude of thrust force, they cannot be measured with the existing load cell. They should be measured using a more sensitive load cell.

The test setup used in the experiments is presented in Figure 3.3. The mechanical structure to mount the load cell and quadrotor in the test section at a desired position and orientation is presented in Figure 3.3 which is designed for the M.Sc. study [3]. The vehicle and the load cell were installed on this mechanical part. Then the whole system was mounted into the wind tunnel in order to measure free-stream velocity, and aerodynamic loads (i.e., forces and moments) simultaneously.

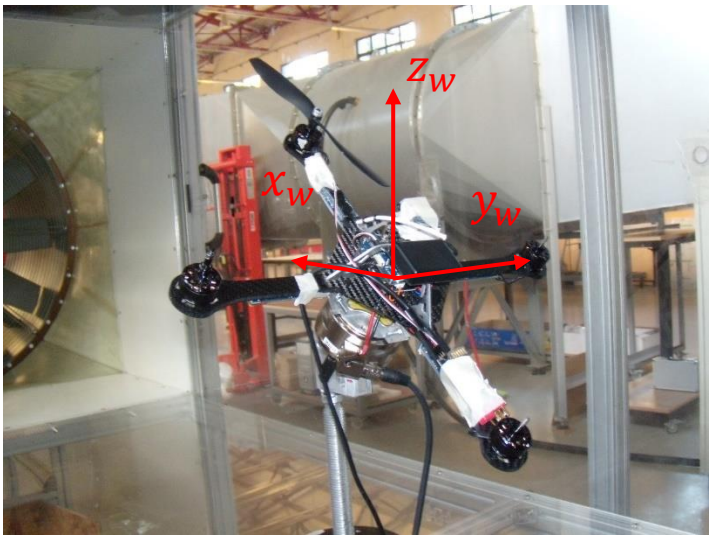

Figure 3.3: Experimental set-up for 8x4.5in propeller (D = 8in) and the axes used in the wind tunnel calibration.

Wind-tunnel dimensions measured from the test section, left wall, and bottom surfaces are as follows:

$$\begin{aligned} 0 < x_w < 2\ m \\ 0 < y_w < 1\ m \\ 0 < z_w < 1\ m \end{aligned} \tag{3.1}$$

Maximum dimensions of the test set-up inside the tunnel measured from the test section, left wall, and bottom surfaces of the wind tunnel are as follows:

$$\begin{aligned} 0.83\ m < x_t < 1.17\ m \\ 0.33\ m < y_t < 0.67\ m \\ 0.33\ m < z_t < 0.67\ m \end{aligned} \tag{3.2}$$

The test set-up consists of a velocity sensor attached at the inlet of the test section presented in Figure 3.4 that has a $0 - 30\ m/s$ range to measure free-stream velocity.

Figure 3.4: Velocity sensor.

The set-up also contains an optical RPM sensor shown in Figure 3.5 to measure the angular velocity of the rotor with ±15 RPM accuracy. The Eagle Tree e-Logger software is used to observe the RPM.

Figure 3.5: Optical RPM sensor.

The electronic part is connected to the data acquisition device given in Figure 3.6 which sends the experimental information from the load cell and velocity sensor to the computer. The National Instruments data acquisition system is used to record testing equipment voltages to the computer. The National Instruments LABVIEW programming software is employed to read and monitor the progress of the

experiment from the DAQ system. A power supply and an Electronic Speed Controller (ESC) are used to run the brushless DC motor of the propeller.

Figure 3.6: Data acquisition system.

Single rotor and single motor were run during the experiments. Steady-state values at various conditions were used. Data were collected at a rate of 1000 samples per second and averaged for processing. Moving average filter is used during the data analyses with a sample size of 15. Forces and moments are measured for a large number of test cases that are combinations of various rotor speeds, free-stream velocities, and angles of attack. Six different free-stream velocities between 0 and 11.07 m/s are scanned at eight different rotor speeds between 2000 RPM and 7000 RPM, and five different angles of attack between 0° and 90°, yielding a total of 500 test cases. Each test is repeated twice, once with the rotor rotating at a certain speed, and one without the rotor installed. Forces and moments measured without the rotor give the loads acting on the body. These values are subtracted from the values measured with the rotor to obtain the net rotor forces and moments. Because the load cell is mounted on the center of gravity of the quadrotor, the measured moments are not the moments on the rotor. The net moments are calculated by subtracting the cross product of length and measured forces from the measured moments.

To analyze test data accurately, each test with the propeller is repeated three times for flight conditions. The propeller test measurement results matched one another well, and repeatability was attainable for all flight conditions.

3.3 Wind Tunnel Characterization

To check the flow quality and uniformity at the inlet of the test section upstream of the propeller setup, horizontal and vertical measurements are conducted using a single hot-wire sensor. Measurements are performed in both the horizontal (Figure 3.3, in y_w axis) and vertical directions (Figure 3.3, in z_w axis) at the centerline of the test section. Experimental data are collected with a step size of $1\ cm$ for a total distance of almost $1\ m$ in the horizontal direction (y_w direction in Figure 3.3) and $1\ m$ in the vertical direction (z_w in Figure 3.3). Hot-wire data are collected at a sampling rate of 10 kHz for 30 seconds for these measurements.

Due to the limited distance of the traverse system used in the experiments the hot-wire is traversed in left and right sides of the horizontal axis, y_w, and top and bottom of the wind tunnel section of the vertical axis, z_w.

Figure 3.7 and Figure 3.8 show the normalized streamwise velocity and Figure 3.9 and Figure 3.10 show turbulence intensity variations along the horizontal and vertical directions, respectively. Results show that the velocity distribution along the horizontal and vertical directions is uniform and quite stable which is acceptable for a low-speed drone's propeller. The turbulence intensities of the wind tunnel in horizontal and vertical axes are determined for the range that the experiments will be conducted. As one could observe the flow is turbulent outside of $0.25\ m$ and $0.8\ m$ distances to the wall in the horizontal axis as seen in Figure 3.9. Between $0.25\ m$ and $0.8\ m$ distances, the turbulence intensity is found below 1% and almost uniform. Because the maximum size of the experimental set-up between $0.33\ m$ and $0.67\ m$ (Equation (3.2)) both in the horizontal and vertical directions, the experiments are not affected by the side walls and top and bottom surfaces of the wind tunnel. In the vertical direction, the turbulence intensity is quite uniform and the corresponding levels are below 1%.

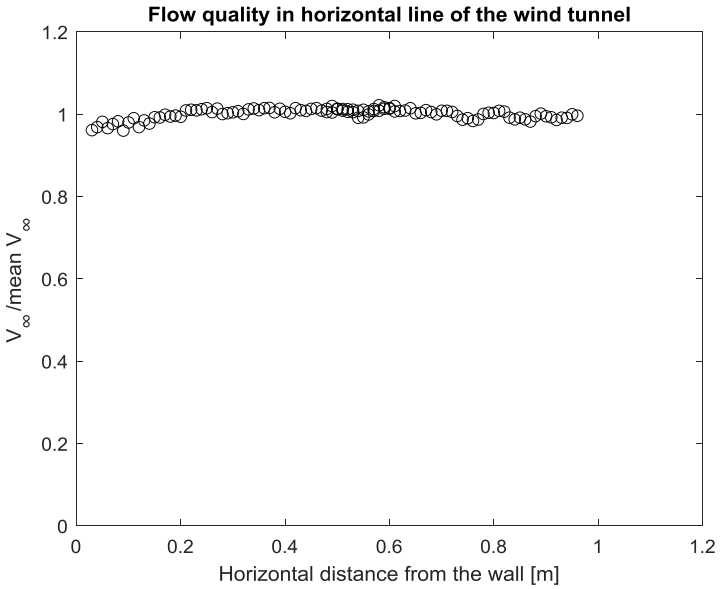

Figure 3.7: Flow quality in the horizontal (i.e., y_w) axis of the wind tunnel.

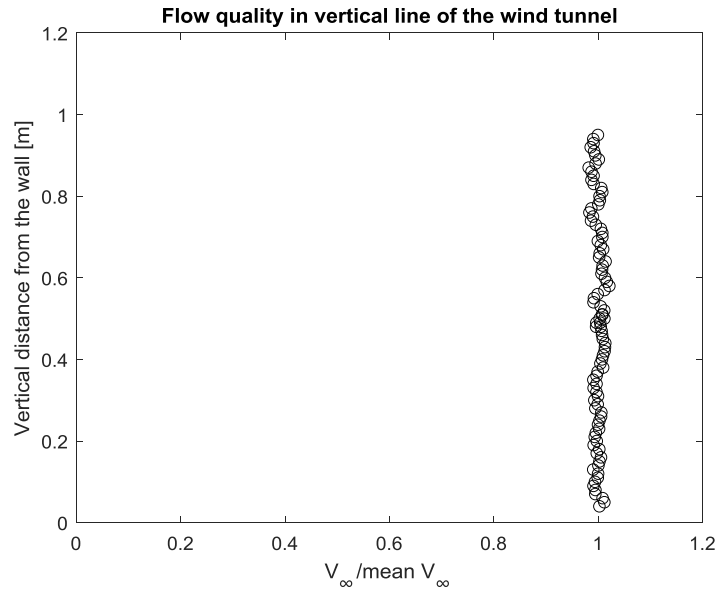

Figure 3.8: Flow quality in the vertical (i.e., z_w) axis of the wind tunnel.

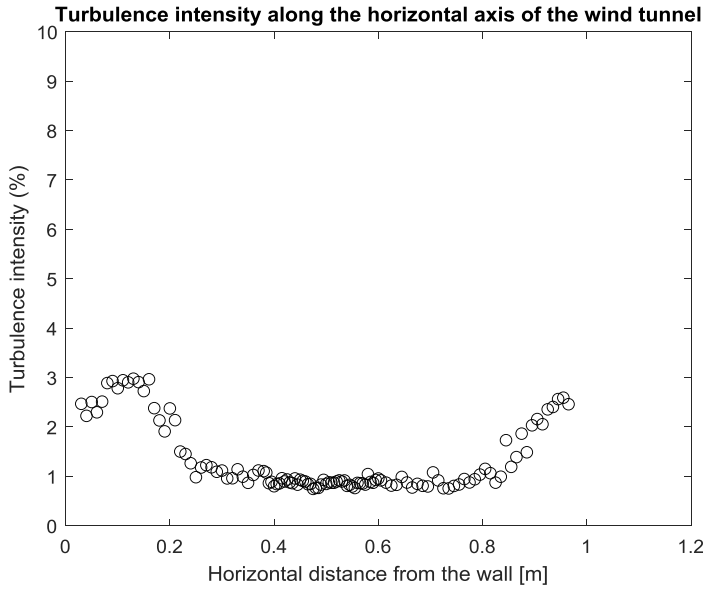

Figure 3.9: Turbulence intensity along the horizontal axis of the wind tunnel.

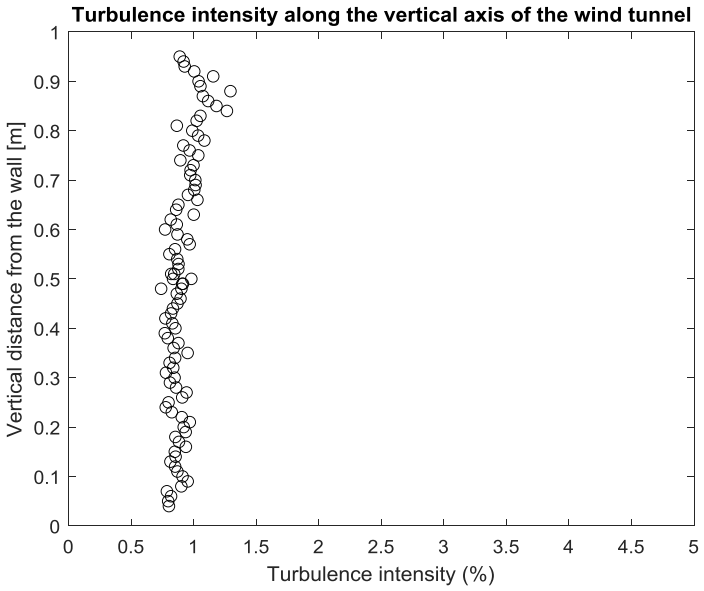

Figure 3.10: Turbulence intensity along the vertical axis of the wind tunnel.

As a result of the wind tunnel characterization, the flow quality of the wind tunnel is convenient for the low-speed and small-scale UAV propellers with less than 1% turbulence intensity both in horizontal and vertical directions of the wind tunnel.

CHAPTER 4

PROPELLER DESIGN OPTIMIZATION

In the field of electric aviation, the challenge is that the flight time of multi-copter manned and unmanned aerial vehicles are still too short because of the limited-battery technology. As a result, choosing the optimum propeller becomes an important factor in the design of aircrafts to increase their flight time. This chapter focuses on finding the optimum propeller of a fixed-wing UAV for a given flight mission profile using the IBEMT model improved in this thesis. The optimum geometric information of the propeller such as its chord length and twist angle can be obtained using the optimization techniques by MATLAB® Optimization Toolbox [35]. The propeller performance is analyzed using the IBEMT model that can estimate the propeller loads in a wide flight regime from hover to forward flight for unmanned aircraft applications. The propeller design process is treated as single-objective function subjected to the highest thrust coefficient and lowest rotor power coefficient for the maximum propeller efficiency.

4.1 Literature Review on Blade Optimization Studies

The optimization studies are most common for ship propellers in the literature [36-42]. Theoretically, both marine and aircraft propellers perform in the same way. However, a marine propeller operates in a much dense fluid, so it experiences more stress compared to an aircraft propeller that makes it more difficult to move through the water. Therefore, structural analysis becomes also important as well as aerodynamic analyses for marine propellers. There are some studies for propeller design optimization [43-46]. An experimental optimization is conducted for a quadrotor propulsion system by testing different propeller and motor combinations [44]. Experimental optimization can be very costly and time-consuming. Besides, it might not converge easily to a good solution because it is based on the traditional

trial and error approach to design. In the study conducted by Dai et al. [45], the precise modeling methods for the propeller, ESC, motor, and battery are studied respectively to solve the optimization problem for the propulsion system of multi-copters in hovering flight. A fixed-pitch propeller of a fixed-wing aircraft called High-altitude Long-Endurance (HALE) UAV that uses twin propellers mounted on each wing is analyzed using BEMT for the propeller performance and CFD for the airfoil analysis, and then the designed propeller is tested in a wind tunnel by Park et al. [46]. In the study conducted by Toman et al. [47], the classical BET is employed as the coarse model and the CFD tool is used as the fine model to predict the propeller performance and experimental data is used to verify the results. Then, blade-shape optimization is performed using MATLAB® for maximum aerodynamic efficiency with a minimal number of high-fidelity model evaluations. For the flow analysis, low-fidelity BEMT and a high-fidelity Navier–Stokes (N–S) flow solver is used [48].

This chapter aims to find the optimum propeller in terms of its chord length, twist angle, and angular speed using the IBEMT model and MATLAB® Optimization Tool-Box [35] that allows the propeller to produce the desired thrust with the lowest power, hence the highest efficiency with acceptable dimensions.

4.2 Objective Function, Design Variables, and Constraints of the Optimization

Propeller aerodynamic loads (i.e., forces and moments in all three axes) are found using the IBEMT model improved in this study that accurately estimates the propeller loads in hover, vertical climb, and forward flight. The IBEMT model subsequently serves as an input to the propeller optimization algorithm in MATLAB® Optimization Toolbox [35] to optimize the propeller geometry (i.e., chord and twist angle distributions along the blade) and angular speed of the propeller for a given flight mission profile for maximum propeller aerodynamic efficiency. The schematic representation of the IBEMT model is given in Figure 2.24.

The input parameters such as free-stream velocity, propeller disk A.o.A., and air properties (i.e., the density of air) at the design point are defined as the operating conditions. In this design optimization process, the radius of the propeller and the number of blades are considered constant. The target performance can be the maximum thrust force or minimum rotor torque. Hence, the propeller efficiency is considered as the target performance.

Propeller aerodynamic efficiency is defined in Equation (4.1):

$$\eta = \frac{C_T}{C_P} J \tag{4.1}$$

The objective function, constraints, design variables and their upper and lower bounds are determined after a careful consideration. The MATLAB® Optimization Toolbox [35] is selected as the optimization algorithm for this study which is designed to minimize a problem. However, the propeller efficiency is thought to be maximized. Therefore, the inverse of the propeller efficiency, $\frac{1}{\eta}$, is used as the objective function to be minimized by the optimization algorithm.

The identification of the right design variables plays an important in optimization. In propeller design optimization, its airfoil, diameter, number of blades, chord distribution, and twist distributions are considered as its planform shape. From an aerodynamic perspective, ideally the airfoil with the best compromised L/D performance in different flight conditions should be selected for each blade element [49].

During the optimization, the angular speed of the propeller, chord, and twist distributions are chosen to be optimized for a given free-stream velocity and thrust required value according to the flight mission profile of a given aircraft. Instead of a reference aircraft, the following values are generated to obtain thrust required and

free-stream velocity plot to demonstrate the application of the IBEMT model in a propeller design optimization problem.

Table 4.1: Generated specifications for a reference aircraft used in the optimization.

C_{D0}, zero-drag coefficient of the aircraft	0.05
$K = \frac{1}{\pi e \boldsymbol{AR}}$	0.05
m_{ac}, mass of the reference aircraft	100 kg
S_{ac}, area of the reference aircraft	4.5 m^2

Forces in steady-level flight is given in Figure 4.1:

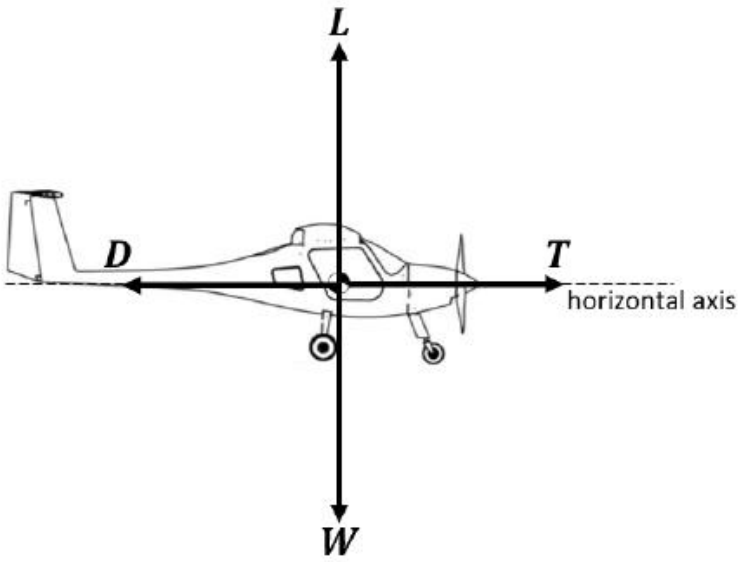

Figure 4.1: Forces in steady-level flight [49].

During the steady-level flight thrust obtained by a fixed-wing aircraft's propeller (Figure 4.1) equals drag:

$$T = D \tag{4.2}$$

Drag force produced by the aircraft during the steady-level flight is as follows:

$$D = \frac{1}{2}\rho S {V_\infty}^2 C_D \tag{4.3}$$

As well, in steady-level flight, lift equals to total weight of the aircraft:

$$L = W \tag{4.4}$$

where

$$L = \frac{1}{2}\rho S {V_\infty}^2 C_L \tag{4.5}$$

By using Equation (4.4), lift coefficient in cruise flight is found as follows:

$$C_L = \frac{2W}{S {V_\infty}^2} \tag{4.6}$$

Drag coefficient is given in Equation (4.7):

$$C_D = C_{D0} + K {C_L}^2 \tag{4.7}$$

Hence, thrust required formula in steady-level flight can be calculated as follows:

$$T_R = \frac{1}{2}\rho S {V_\infty}^2 \left\{ C_{D0} + K \left(\frac{2W}{\rho S {V_\infty}^2} \right)^2 \right\} \tag{4.8}$$

Using the information in Table 4.1, thrust required can be plotted to be used in propeller design optimization at different free-stream velocities as shown in Figure 4.2:

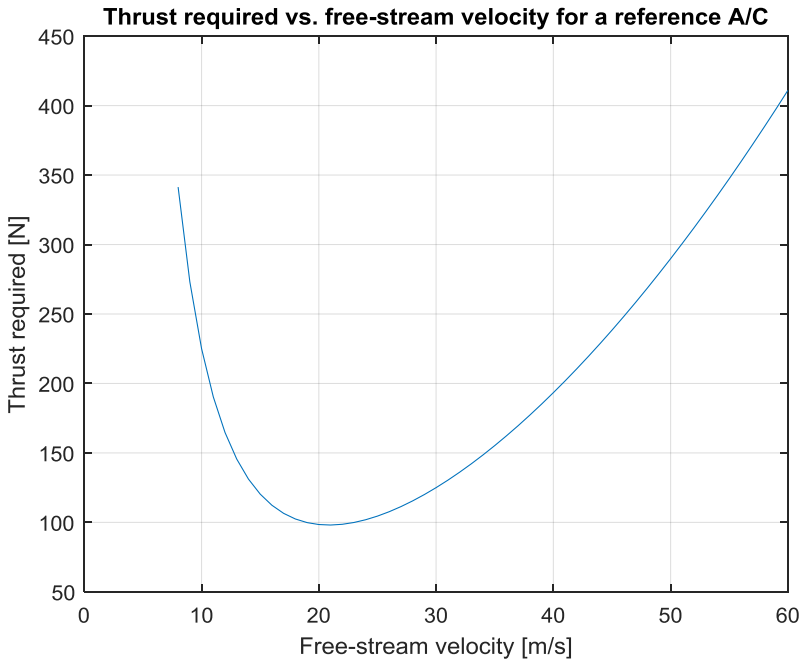

Figure 4.2: Thrust required versus free-stream velocity for a reference aircraft.

For the chord distribution, the constraint in Equation (4.9) and the lower and upper bounds presented in Figure 4.3 proposed in [49] are used to avoid unrealistic blade shapes which can cause structural disadvantages.:

$$c_3 > c_4 \tag{4.9}$$

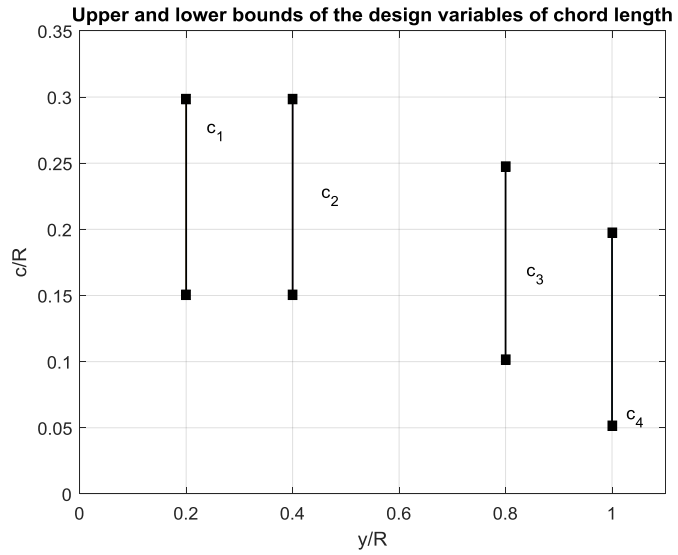

Figure 4.3: Lower and upper bounds of the chord distributions.

Similarly, the constraint for the twist distribution that ensures the decreasing twist angle from root to tip is formulated in Equation (4.10) and the upper and lower bounds for the twist angles are given in Figure 4.4

$$\theta_3 > \theta_4 \tag{4.10}$$

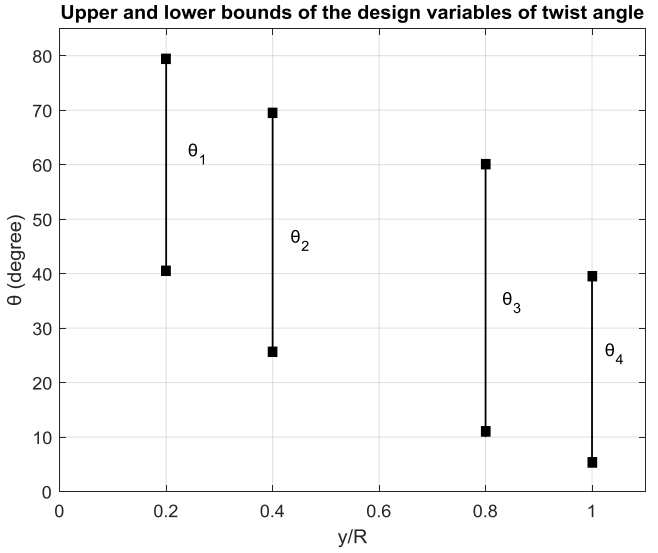

Figure 4.4: Lower and upper bounds of the twist distributions.

Initial values of the design variables are chosen as follows:

$$\vec{x}_{0_{total}} = [0.20\text{R}, 0.20\text{R}, 0.15\text{R}, 0.15\text{R}, 42°, 32°, 22°, 13°, 1500\ RPM] \quad (4.11)$$

The optimization problem is defined as follows:

$$\text{Minimize} \quad F(\vec{x}_{total}) = \frac{1}{\eta(\vec{x})} + p(\sum \min\{0, g(\vec{x})\}^2)$$

$$\text{w.r.t} \quad \vec{x}_{total} = \vec{x}_{total}(\, c_1, c_2, c_3\, , c_4, \theta_1, \theta_2, \theta_3, \theta_4, \Omega)$$

$$\text{subject to } \vec{x}_{0_{total}},\ \overrightarrow{lb}_{total},\ \overrightarrow{ub}_{total}$$

$$g_1 = \frac{c_3}{c_4} - 1 > 0 \quad (4.12)$$

$$g_2 = \frac{\theta_3}{\theta_4} - 1 > 0$$

$$g_3 = \frac{T}{T_R} - 1 > 0$$

The objective function of the optimization problem consists of $\frac{1}{\eta(\vec{x})}$ and a penalty function term ($p = 10^4$) which ensures that if one or more of the constraints are violated the objective function value is increased significantly. The upper and lower bounds are included to the objective function with the penalty term since MATLAB® fminsearch is used. The initial values, lower and upper bounds of the design variables are defined in Equation (4.11), Figure 4.3, and Figure 4.4.

The flowchart of the optimization method is as follows:

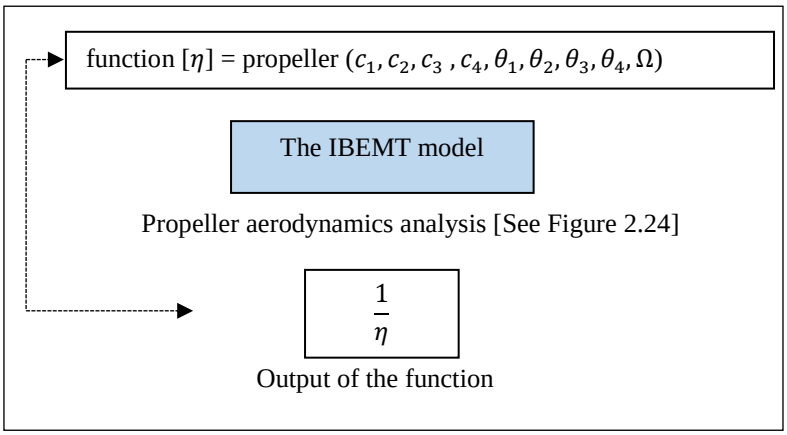

Figure 4.5: Schematic of building the function for the optimization process with MATLAB®.

CHAPTER 5

RESULTS

The results of the IBEMT model with the validation of the wind tunnel tests, comparison of the model with another experimental data found in the literature, the effects of the assumptions made in the classical BET on thrust force, propeller efficiency obtained from the IBEMT model, and the optimization using the IBEMT model are presented in separate sub-sections, respectively:

5.1 Validation of the IBEMT Model by the Wind Tunnel Experiments

The IBEMT model is verified with experimental data obtained from the wind tunnel tests. The results of 0^o angle of attack (i.e., in the presence of free-stream velocity) are presented in Figure 5.1. As can be understood from Figure 5.1, at 0^o A.o.A., the free-stream velocity does not affect the thrust force negatively. However, as the propeller disk angle of attack increases thrust is started to decrease as shown in Figure 5.2, Figure 5.3, Figure 5.4, and Figure 5.5.

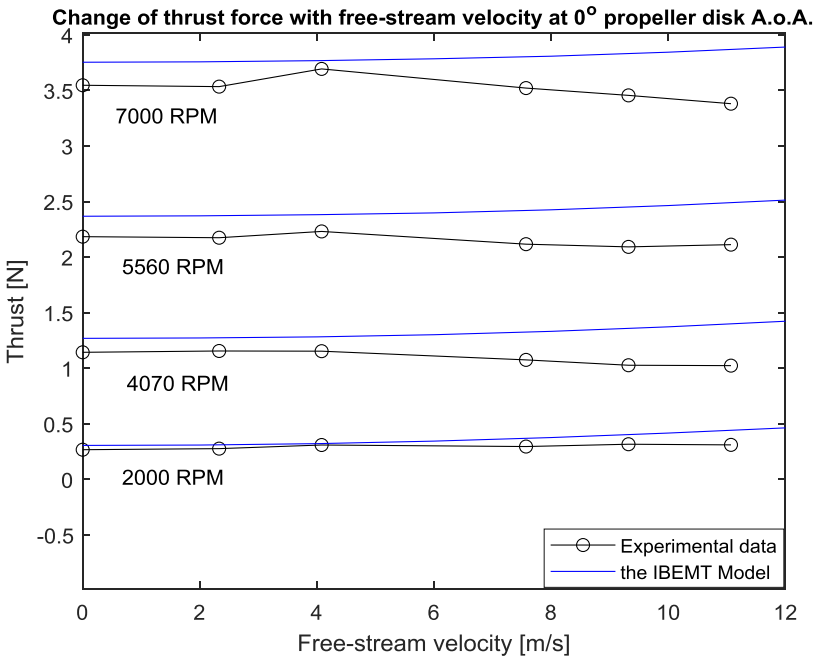

Figure 5.1: Thrust versus free-stream velocity (wind speed) at 0^o propeller disk A.o.A.

The results of 30^o angle of attack are presented in Figure 5.2. As can be understood from the figure, the free-stream velocity adversely affects the thrust. Besides, the error between the experimental data and the IBEMT model increases as the propeller's speed increases. The reason for this is that at higher RPM values, the experimental set-up starts to vibrate which affects the accuracy of the test data obtained by the load cell. As well, at lower RPM values, after 7 m/s wind speed, the error between the experimental data and the IBEMT model also increases as the wind tunnel speed increases because of the vibrations of the test set-up. Hence, at higher RPM values such as more than 4000 RPM and the higher free-stream velocities such as more than 7 m/s, using the IBEMT model gives mode accurate results compared to wind tunnel tests.

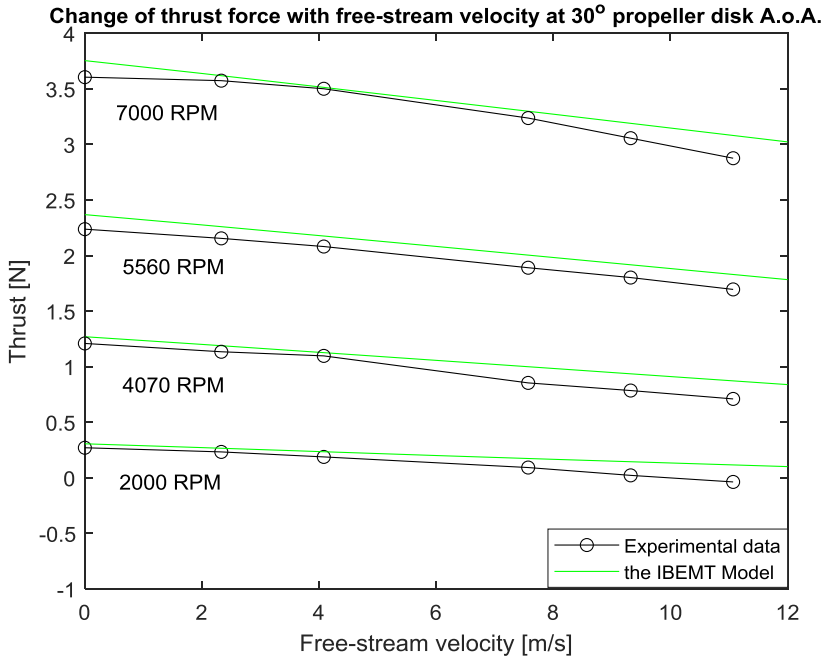

Figure 5.2: Thrust versus free-stream velocity (wind speed) at 30^o propeller disk A.o.A.

The thrust change with free-stream velocity at four different angular speeds of the propeller at 45^opropeller disk angle of attack (see Figure 2.4 for the velocity directions at 45^o A.o.A.) is presented in Figure 5.3. The decrease of the thrust force with free-stream velocity is more noticeable than the case of 30^opropeller disk angle of attack as expected. Same conclusion can be made for the 45^opropeller disk angle of attack such that at 7000 RPM, the difference between the experimental data and the IBEMT model is more noticeable compared to lower RPM values.

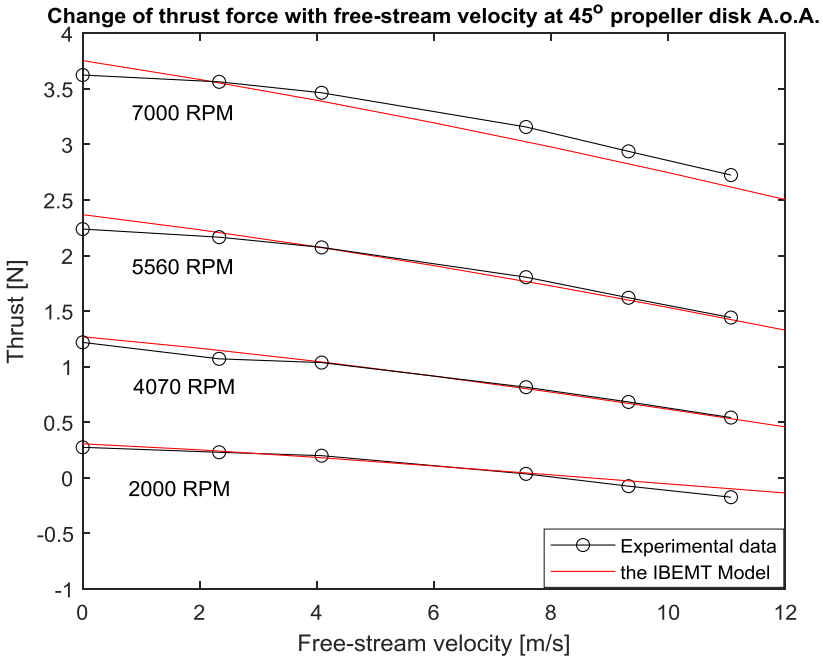

Figure 5.3: Thrust versus free-stream velocity (wind speed) at 45^o propeller disk A.o.A.

The results of 60^o propeller disk angle of attack are presented in Figure 5.3. The same conclusion can be obtained for 60^o A.o.A. Propeller thrust force is more affected by the free-stream velocity as the A.o.A. increases. As a result, the decrease of the thrust at 60^o is higher than when the propeller disk A.o.A. equals 45^o.

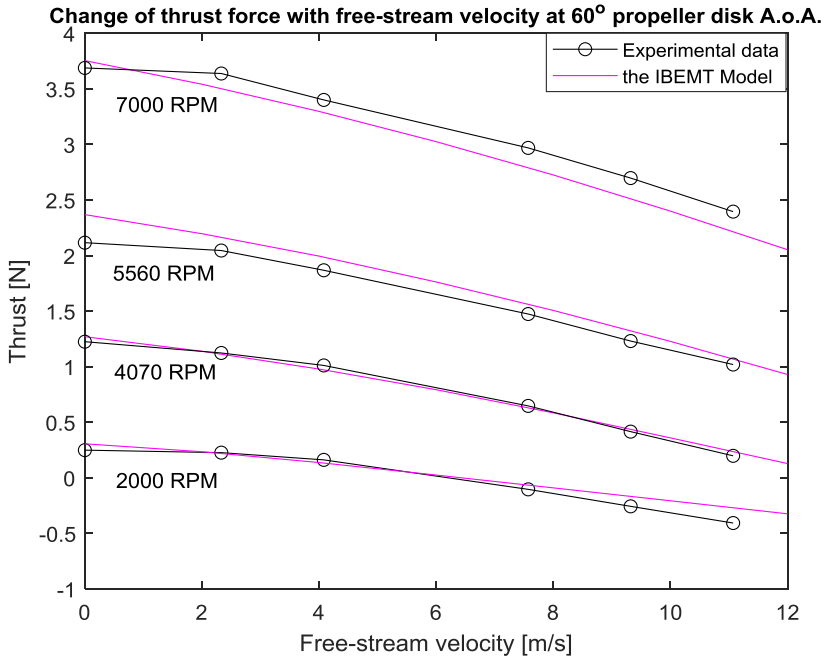

Figure 5.4: Thrust versus free-stream velocity (wind speed) at 60^o propeller disk A.o.A.

The result of 90^o angle of attack is presented in Figure 5.5. As expected, the thrust force is most affected by the free-stream velocity at 90^o A.o.A. when the flow is perpendicular to the propeller disk (see Figure 2.5 for the velocity directions at 90^o A.o.A.).

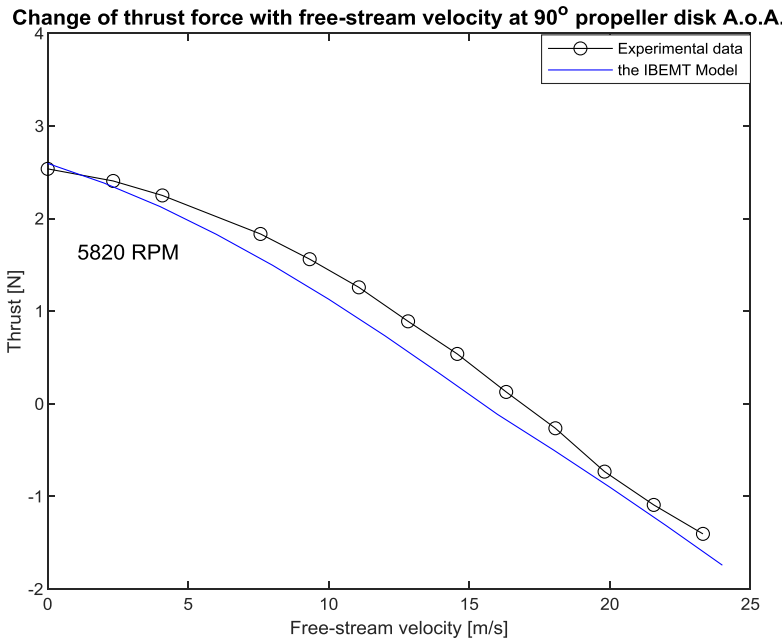

Figure 5.5: Thrust versus free-stream velocity (wind speed) at 90^o propeller disk A.o.A.

The experimental data of the change of thrust force with the angular speed of the propeller at 0^o propeller disk A.o.A. are given in Figure 5.6 at three different wind tunnel speeds. Besides, it is captured by the IBEMT model in Figure 5.7. As seen in Figure 5.6, there is not a certain trend of thrust force depending on the free-stream velocity is parallel to the propeller disk ($\alpha = 0^o$). However, the IBEMT model results presented in Figure 5.7 gives a conclusion on 0^o propeller disk A.o.A. such that thrust force increases with free-stream velocity when the flow is parallel to the rotor disk.

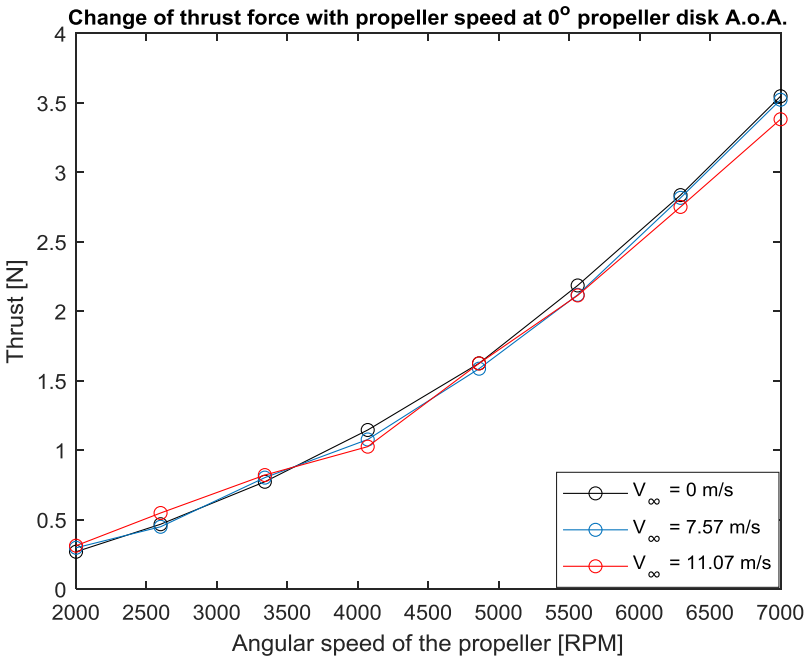

Figure 5.6: Experimental data of the thrust change with angular speed of the propeller at 0^o propeller disk A.o.A.

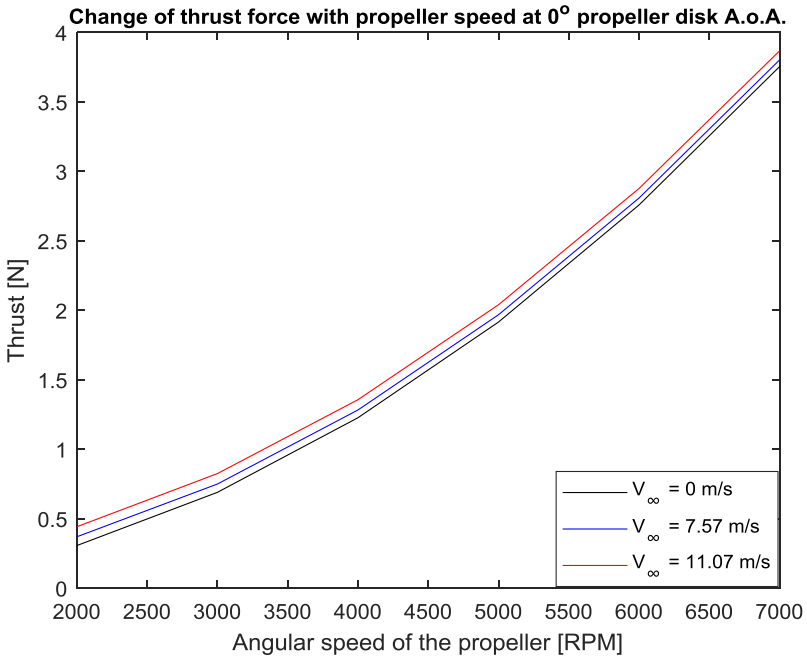

Figure 5.7: Thrust change with angular speed of the propeller at 0^o A.o.A., using the IBEMT model.

On the other hand, at 30^o propeller disk A.o.A. (Figure 5.8) unlike 0^o A.o.A, as the propeller disk A.o.A. increases thrust produced by the propeller decreases as well. As is expected, lower thrust is obtained at higher wind speed at the same RPM values.

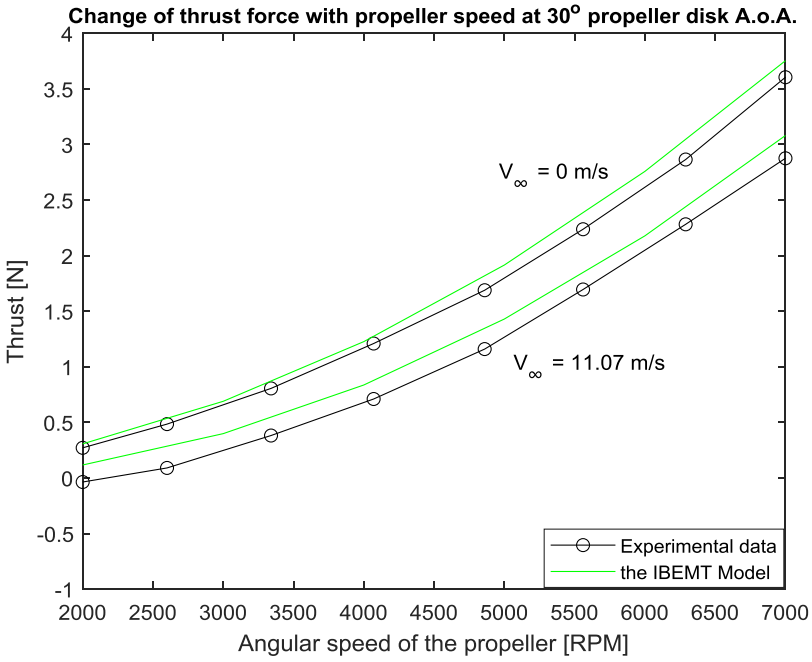

Figure 5.8: Thrust versus angular speed of the propeller at 30^o A.o.A.

Thrust change with propeller's angular speed at 45^o A.o.A. is presented in Figure 5.9. The difference between the lowest and the highest free-stream velocity is more noticeable compared to 30^o A.o.A. (Figure 5.7). The difference between $0\ m/s$ and $11\ m/s$ increases as the propeller disk A.o.A. increases which implies that the aerodynamic performance of the thrust force at higher propeller disk angles of attack in the presence of the free-stream velocity becomes crucial.

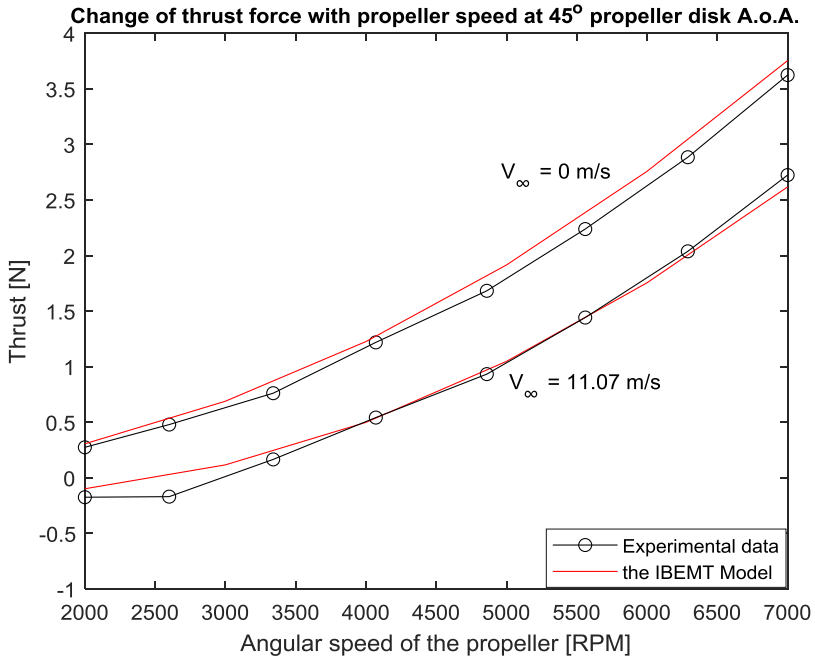

Figure 5.9: Thrust versus angular speed of the propeller at 45^o A.o.A.

Thrust change with propeller's angular speed at 60^o A.o.A. is presented in Figure 5.10. From Figure 5.10, it is verified that the difference between 0 m/s and 11 m/s increases as the A.o.A. of the propeller increases when it is compared with Figure 5.8 and Figure 5.9.

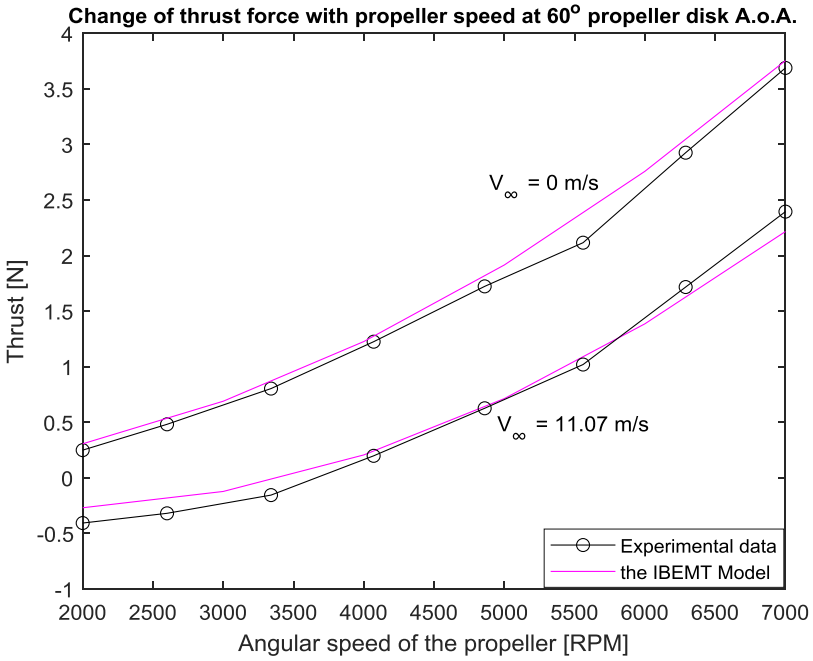

Figure 5.10: Thrust versus angular speed of the propeller at 60^o A.o.A.

The trend of the experimental data is captured by the IBEMT model as shown in Figure 5.11. In Figure 5.11, the dash lines represent the test data, and the solid lines show the results obtained by the IBEMT model. As seen, thrust force increases only when the propeller disk A.o.A equal zero ($\alpha = 0°$) which means that the flow is parallel to the rotor disk. On the other hand, as the propeller disk A.o.A. increases ($\alpha = 30°, 45°, 60°$), thrust force starts to decrease.

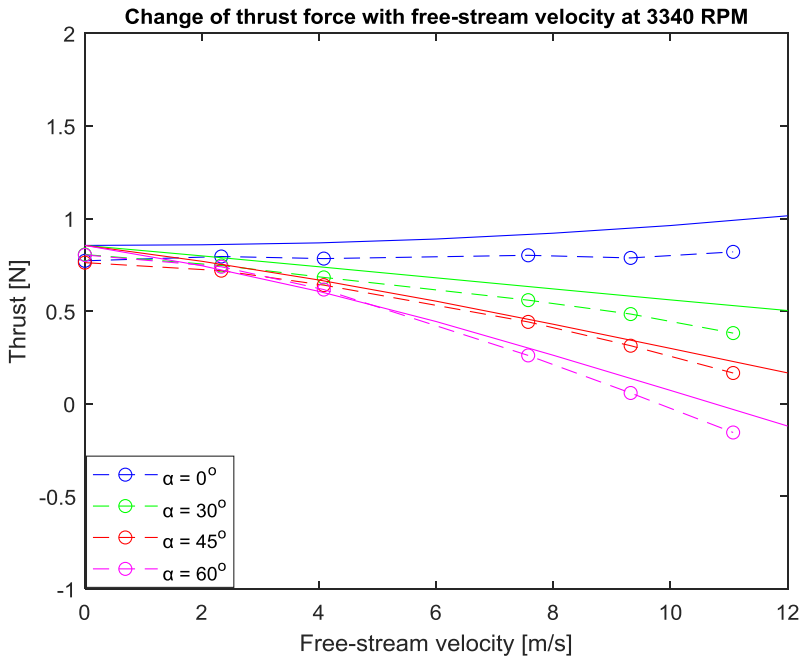

Figure 5.11: Comparison of IBEMT model with experimental data at different angles of attack, at 3340 RPM.

Rotor torque, hub force, and rolling moment are too small compared to thrust force. Therefore, these loads cannot be found experimentally by the load cell used in this study with given specifications presented in Table 3.1. It is recommended that a more sensitive load cell should be used to measure these small-aerodynamic loads accurately.

The change of the rotor torque with the free-stream velocity at different propeller disk angles of attack found by the IBEMT model is given in Figure 5.12. Rotor torque decreases with an increasing A.o.A.

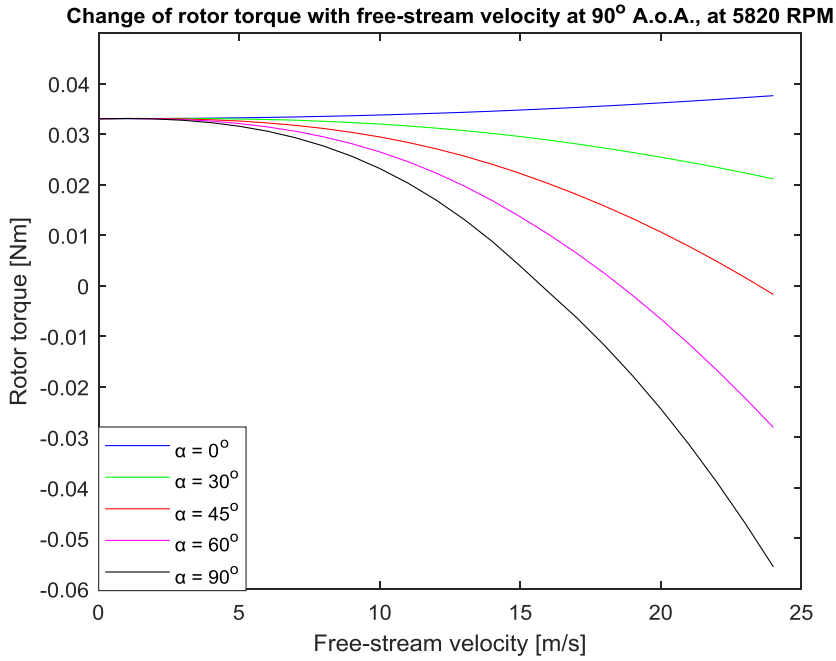

Figure 5.12: Change of rotor torque with free-stream velocity found by the IBEMT model.

The change of the hub force with the free-stream velocity at different propeller disk angles of attack is given in Figure 5.13. As expected and it is seen in Figure 5.13, when $\alpha = 90°$, only thrust force acts on the propeller, hub force should equal zero. On the other hand, as the propeller disk A.o.A. decreases, the hub force increases in the negative direction of the x_B axis (See Figure 2.1 for the direction of the hub force on a propeller). The maximum hub force occurs at 0° propeller disk A.o.A. as shown in Figure 5.13.

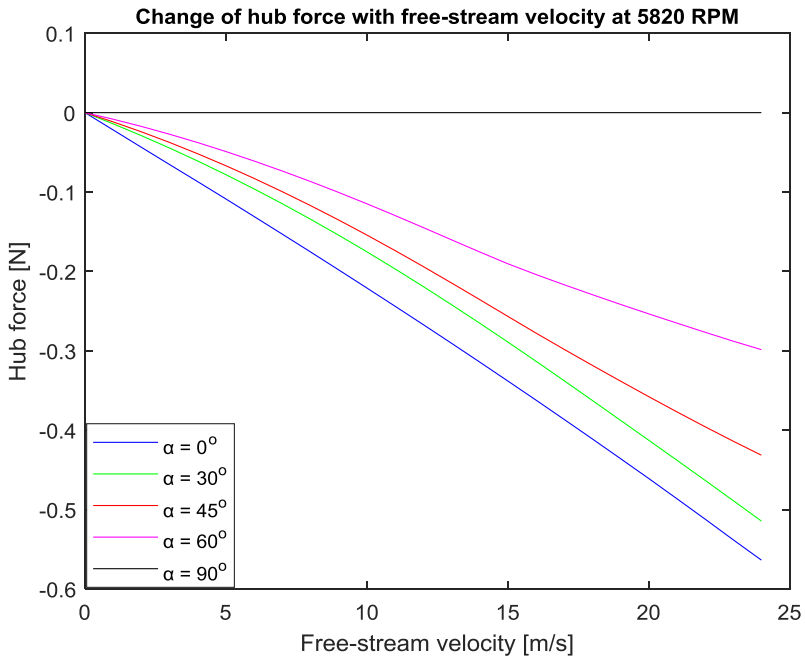

Figure 5.13: Change of hub force with free-stream velocity at 5820 RPM, at different propeller disk angles of attack.

The change of the rolling moment with the free-stream velocity at different propeller disk angles of attack is given in Figure 5.14. The rolling moment occurs due to the advancing and retreating blades see different free-stream velocities. When the free-stream velocity is perpendicular to the rotor disk (i.e., $\alpha = 90°$), the advancing and the retreating part of the propeller sees the same free-stream velocity. Therefore, the rolling moment becomes zero. On the other hand, when the free-stream velocity is parallel to the rotor disk (i.e., $\alpha = 0°$), the rolling moment becomes more noticeable because propeller sees different free-stream velocities at the advancing and retreating side of the rotor disk.

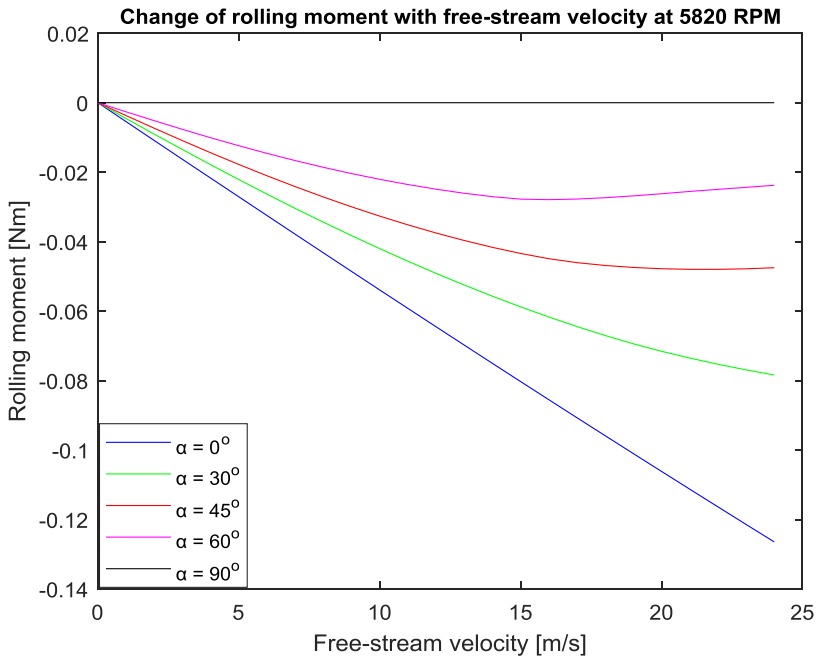

Figure 5.14: Change of rolling moment with free-stream velocity at 5820 RPM, at different propeller disk angles of attack.

The analytical results show that side force and pitching moment equal zero after the integration in the classical BET (See Table 2.1 for the analytical results). The IBEMT model verifies these results as seen in Figure 5.15 and Figure 5.16, respectively.

In some studies, the component of the hub force in y_B axis (See Figure 2.1) with a non-zero side-slip angle is defined as side force. Similarly, the component of the rolling in y_B axis (See Figure 2.1) with a non-zero side-slip angle is defined as pitching moment. However, they are still the components of the hub force and rolling in y_B axis. According to the definitions of the forces and moments acting on a blade [12, 13] side force and pitching moment equal to zero.

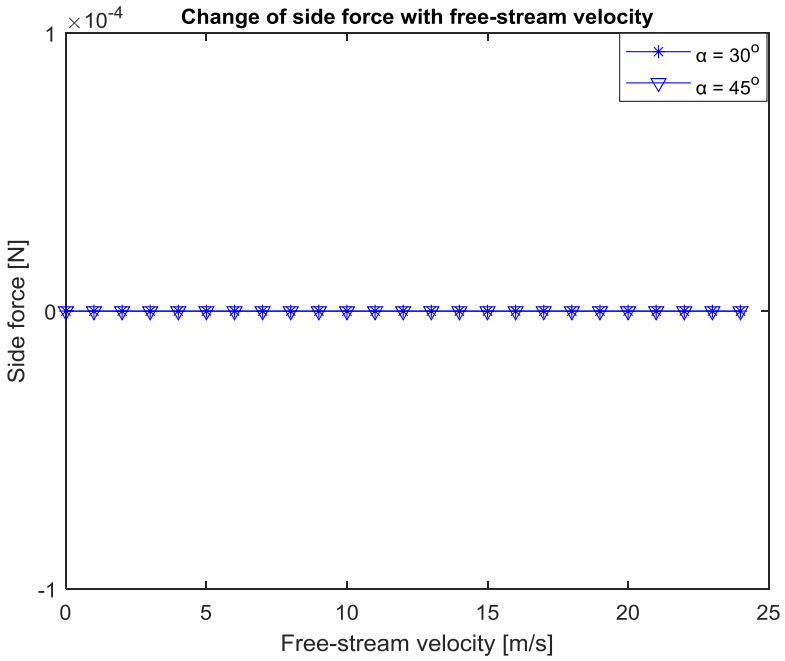

Figure 5.15: Change of side force with free-stream velocity at 5820 RPM.

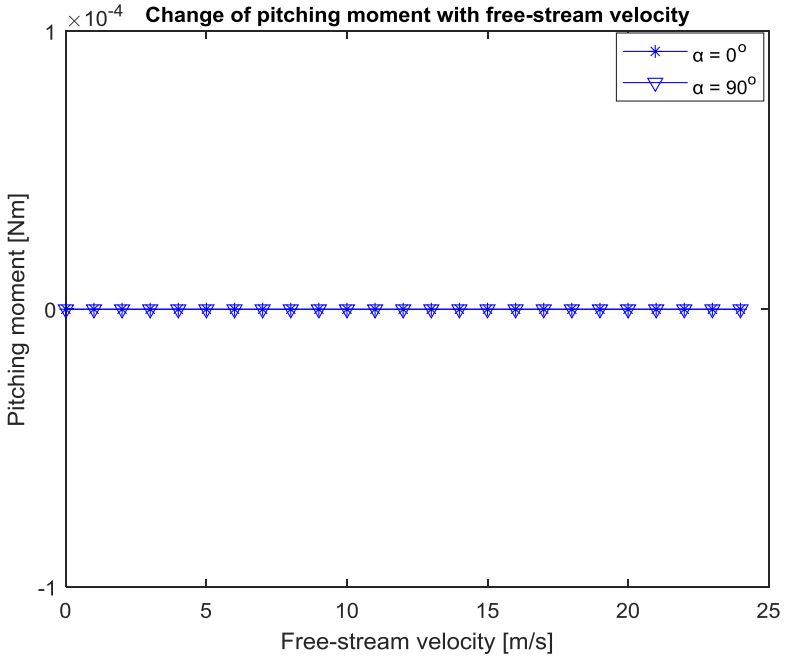

Figure 5.16: Change of pitching moment with the free-stream velocity at 5820 RPM.

In hovering flight, only thrust force and rotor torque acts on a propeller. Yet, in the presence of free-stream velocity, hub force and rolling moment occurs. Side force and pitching moment equal zero both in the absence and presence of the free-stream velocity. These theoretical results are validated with the IBEMT model. However, because the rotor torque, hub force, and rolling moment are too small to be measured by the load cell used in this study, they are captured by the IBEMT model. The rotor torque results obtained from the IBEMT model is compared with another in-house BEMT model in the following section by comparing the power coefficients results.

5.2 Comparison of the IBEMT model with another experimental data and a CFD study

Comparison of the IBEMT model with the experimental data given by Serrano et al. [27] with SF 12x6in (slow flyer) propeller given in Figure 5.17. The IBEMT model is compared with [27] because the propeller geometric data was available.

The green plots in the left-hand side of Figure 5.17 are compared with the IBEMT model (right-hand side of Figure 5.17). Note that in the study conducted by Serrano et al. [27], the propeller disk A.o.A., α_p, is defined as zero when the free-stream velocity is perpendicular to the rotor disk. However, in this study, it is defined as 90°. Therefore, in [27], α_p corresponds to $90° - \alpha$ in this study. To compare the results, α is changed with $90° - \alpha$ in the legend of the (right-hand side of Figure 5.17).

Thrust coefficient results are very close to each other at different propeller disk A.o.A. as seen in Figure 5.17 and Figure 5.18 for two different propellers operating different RPM values:

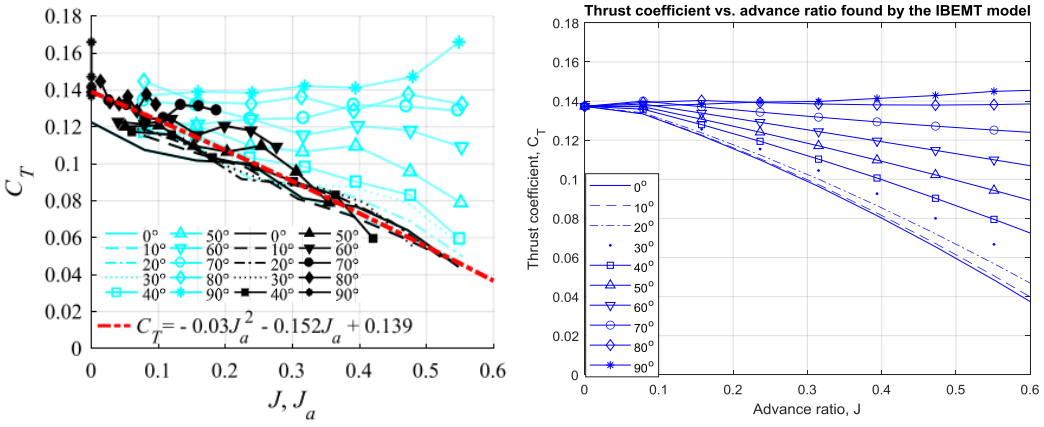

Figure 5.17: C_T comparison of the SF 12x6in propeller at different propeller's disk angles of attack at 5000 RPM (the results in [27] and the IBEMT model's result, respectively).

The thrust coefficient results obtained by Serrano et al. [27] with SP 12x6in (sport flyer) propeller experimentally and obtained by the IBEMT model are given in Figure 5.18:

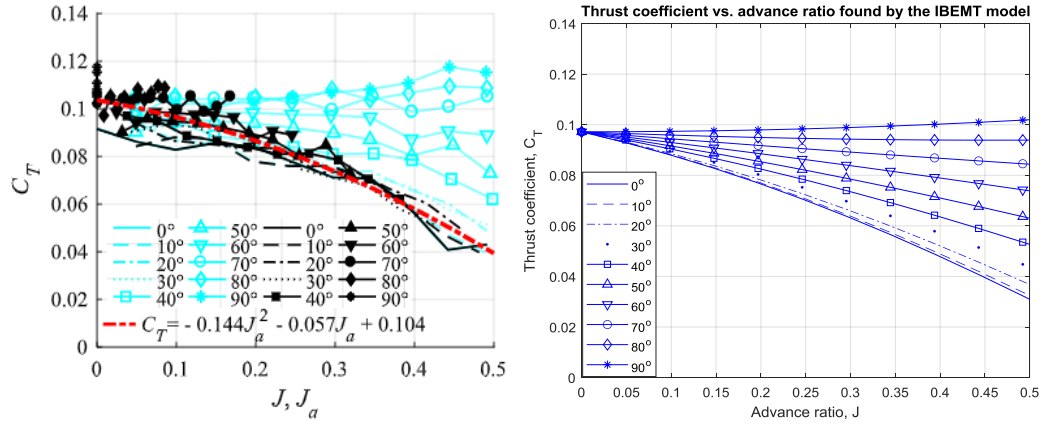

Figure 5.18: C_T comparison of the SP 12x6in propeller at different propeller disk angles of attack at 8000 RPM (the results in [27] and the IBEMT model's result, respectively).

Power coefficient results obtained by Serrano et al. [27] with SF 12x6in (slow flyer) propeller experimentally and obtained by the IBEMT model are given in Figure 5.19:

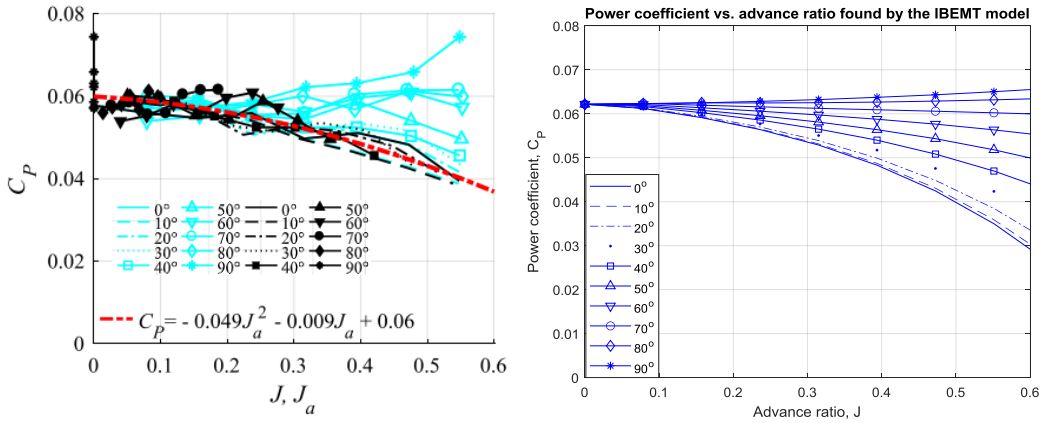

Figure 5.19: C_P comparison of the SF 12x6in propeller at different propeller's disk angles of attack at 5000 RPM (the results in [27] and the IBEMT model's result, respectively).

The power coefficient results obtained by Serrano et al. [27] with SP 12x6in (sport flyer) propeller experimentally and obtained by the IBEMT model are given in Figure 5.20:

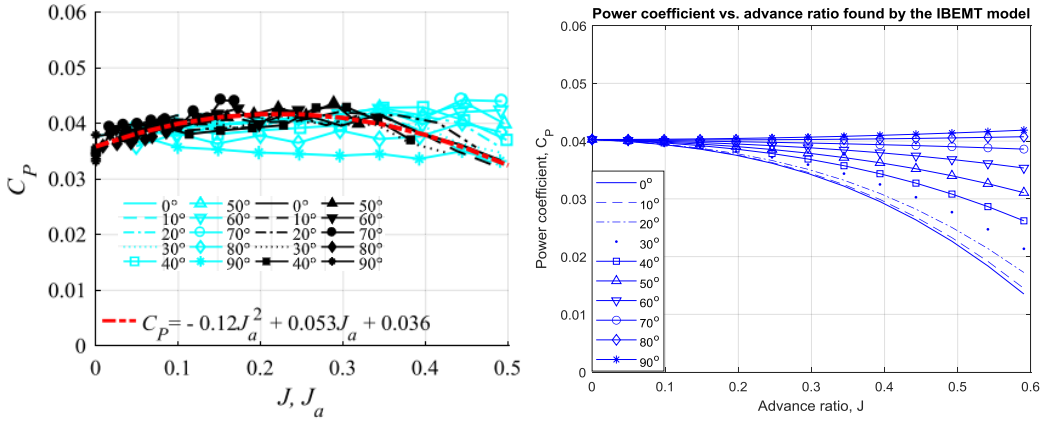

Figure 5.20: C_P comparison of the SP 12x6in propeller at different propeller's disk angles of attack at 8000 RPM (the results in [27] and the IBEMT model's result, respectively).

As one could observe from Figure 5.17 and Figure 5.18 that the thrust coefficient results obtained by the IBEMT model are very close to the experimental data in [27].

As well, results of the power coefficients are also very close up to 0.4 advance ratio. However, as the advance ratio exceeds 0.4, the power coefficient found by the IBEMT model are more sensitive to the free-stream velocity compared to [27] as shown in Figure 5.19 and Figure 5.20 which is expected because as the flow comes to the rotor disk perpendicularly, rotor torque decreases with an increasing free-stream velocity (Figure 5.12). Since the power coefficient depends on rotor torque (Equation (5.4)), it is expected to decrease with free-stream velocity, as well.

The IBEMT model results are also compared to a CFD study [10] for which the geometric properties of the propeller used and operating conditions are known in hovering flight. The thrust force and rotor torque produced by a 16x4in propeller at $1050, 2000$, and 3150 RPM found using CFD simulations are given in [10]. The results are obtained by the IBEMT model at the same operating conditions. The results are compared for thrust force and for rotor torque in Figure 5.21 and Figure 5.22, respectively:

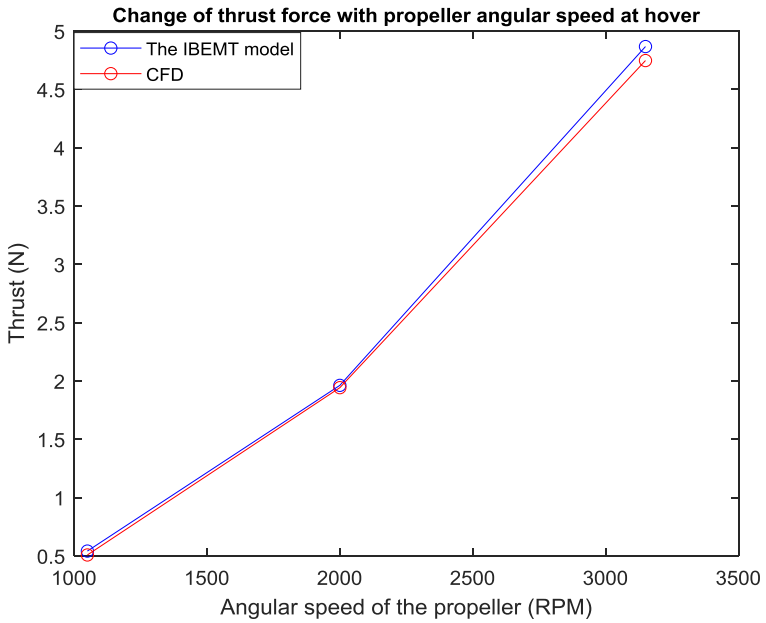

Figure 5.21: Change of thrust force with angular speed of the propeller found by the IBEMT model and CFD method [10] for a 16x4in propeller (D = 16in).

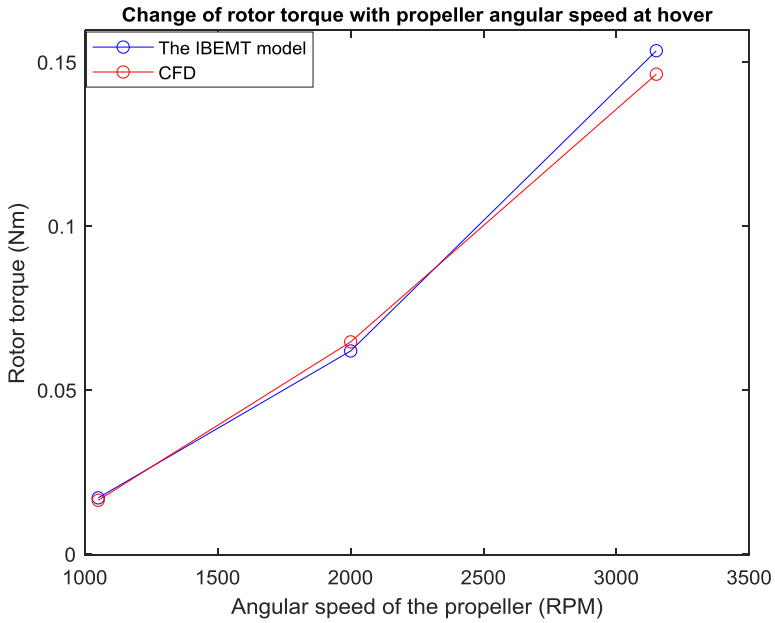

Figure 5.22: Change of rotor torque with angular speed of the propeller found by the IBEMT model and CFD method [10] for a 16x4in propeller (D =16in).

Table 5.1: Thrust and power coefficient comparison data for hovering flight, 16x4in.

	CFD		Wind tunnel test		The IBEMT model	
RPM	C_T	C_P	C_T	C_P	C_T	C_P
1050	0.0542	0.0264	0.0564	0.0278	0.0556	0.0272
2000	0.0561	0.0288	0.0627	0.0271	0.0556	0.0272
3150	0.0559	0.0263	0.0577	0.0246	0.0556	0.0272

5.3 Effects of the Assumptions used in the Classical BET on Thrust Force

In subsection 5.1, the performance of the IBEMT model is validated with the wind tunnel measurements using an 8x4.5in UAV propeller. Moreover, it is compared with another BEMT model for two different propellers operating at different flight conditions. According to the results given in the sections 5.1 and 5.2, it is concluded that the thrust is most affected by the free-stream velocity at 90^o A.o.A. Therefore,

the assumptions in the classical BET are investigated at 90^o A.o.A. to see the maximum effects of the assumptions on thrust force.

In Section 2.1, assumption 2 is investigated. In the classical BET, the lift and drag coefficients are found as follows:

$$C_l = 2\pi\alpha_b \tag{5.1}$$

Besides, the drag coefficient is assumed constant: $C_d = \overline{C_d} = 0.1$

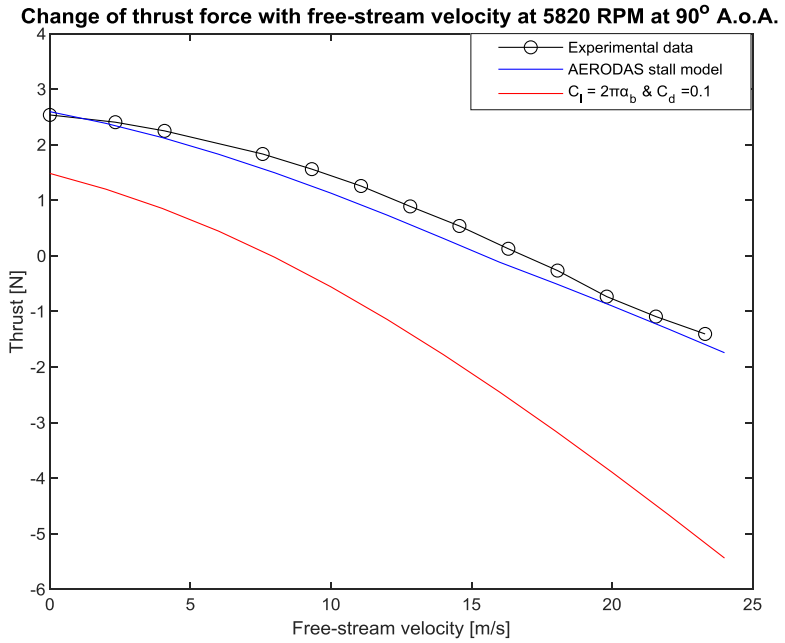

Figure 5.23: Comparison of the linear lift coefficient assumption and a more developed stall model AERODAS [31].

Modeling the post-stall region for the airfoil is important to get an accurate result. According to Figure 5.23, the stall model affects results remarkably. Therefore, in the classical BET, assumption 2 causes an inaccurate estimation of thrust force. It is highly recommended that a stall model should be included in BEMT estimations.

Assumption 3 is investigated in Figure 5.24, and assumption 4 is investigated in Figure 5.25. Assuming the change of the twist angle along the blade linearly is a very reasonable assumption. The crucial point is that the identification of the twist

distribution along the blade accurately because the IBEMT model is very sensitive to the twist angle distributions.

Chord length can be assumed constant and the average value of it can be used according to Figure 5.25:

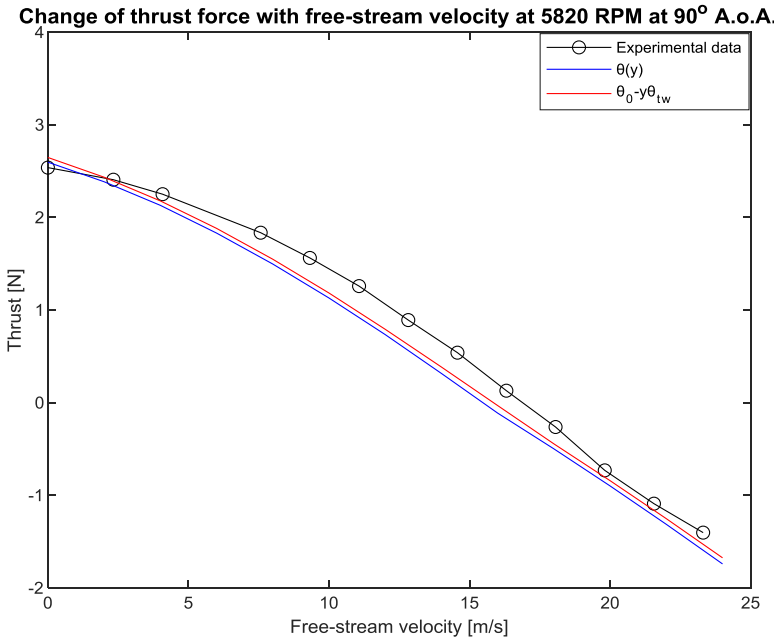

Figure 5.24: Comparison of the experimental data with the linear twist assumption and using twist distribution along the blade.

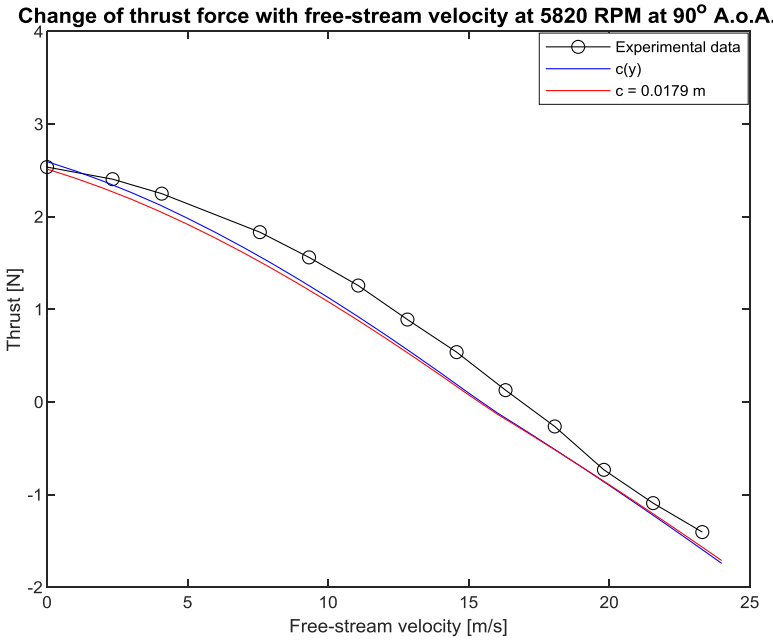

Figure 5.25: Comparison of the chord changing along the radius and average chord length $\overline{c} = 0.0179\ m$, 90° propeller disk A.o.A., 5820 RPM.

Assumption 5, which neglects the sectional drag, is demonstrated in Figure 5.26. As a result, the sectional drag force can be neglected in the calculation of thrust force.

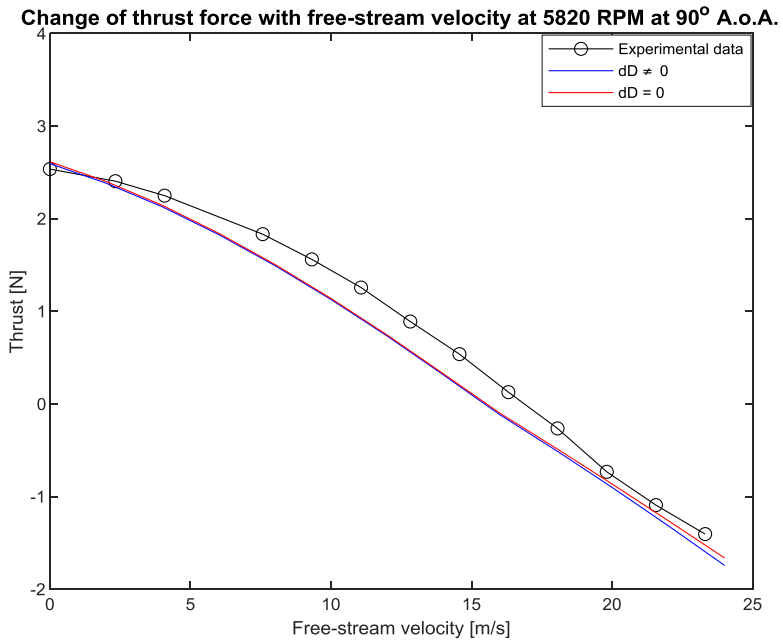

Figure 5.26: Thrust force results including and ignoring sectional drag force.

Assumption 6, which assumes that the inflow angle is too small, is investigated in Figure 5.27. Assuming the inflow angle very small (red plot in Figure 5.27) is meaningful up to 10 m/s free-stream velocity. However, as the free-stream velocity increases the importance of the inflow angle increases, too. Therefore, it is recommended that the small angle assumption, which is applied assuming that the inflow angle, ϕ, is very small, should not be used to get accurate results in higher flight speeds.

Note that when the effect of an assumption is studied, the other assumptions are not applied to the calculation of thrust force. For instance, during the investigation of liner-twist assumption (assumption 3), AERODAS stall model is used, as well as chord length is thought to change with blade radius, inflow angle is not assumed too small, sectional drag force is not ignored and induced velocity is calculated at each section of the rotor disk.

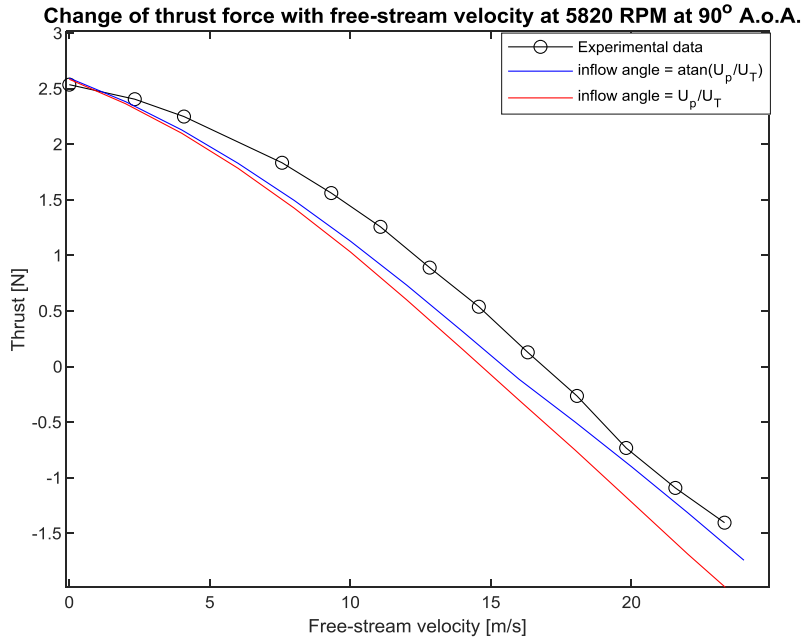

Figure 5.27: The comparison of the assumption on the inflow angles.

Finally, the assumption on the induced velocity is presented in Figure 5.28. In the classical BET, the induced velocity at hovering flight is used to obtain an analytical solution. However, induced velocity changes along the blade radius, y, and it depends on thrust force, as well. For this reason, the iterative solution and non-uniform calculation of the induced velocity is implemented to improve the classical BET which is realized as one of the most important development in the IBEMT model as well as implementing a realistic stall model.

The importance of the accurate calculation of induced velocity is illustrated in Figure 5.28:

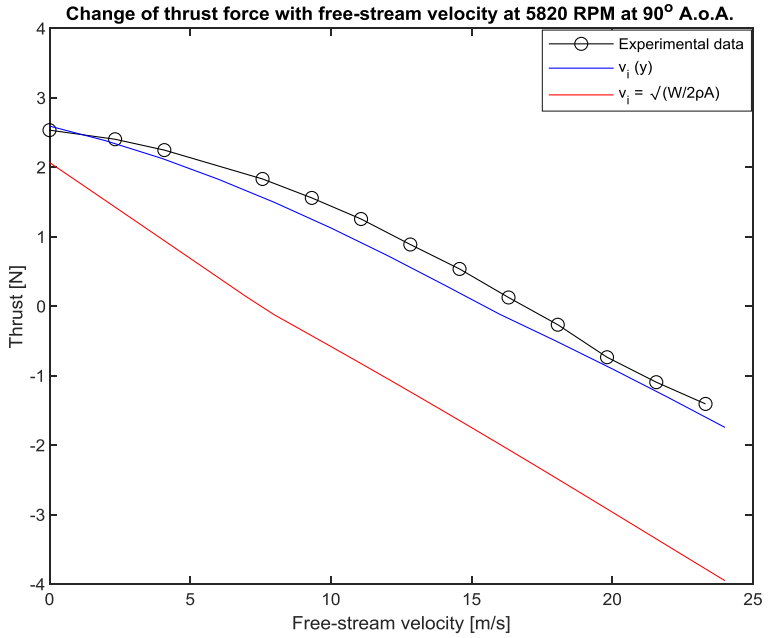

Figure 5.28: The comparison of the assumption on the induced velocity.

5.4 Efficiency of 8x4.5in Propeller

Since the aerodynamic efficiency of the propeller depends on the advance ratio, thrust coefficient, and power coefficient of the propeller the mathematical expressions of these parameters are needed to be defined.

In aeronautics, the advance ratio is the ratio of the free-stream velocity to the propeller's tip speed, and formulated as follows:

$$J = \frac{V_\infty}{nD} \tag{5.2}$$

According to the Buckingham Pi Theorem [51], the thrust coefficient is expressed as follows:

$$C_T = \frac{T}{\rho n^2 \mathrm{D}^4} \tag{5.3}$$

The change of the thrust coefficient with the advance ratio is given in Figure 5.29. It is independent of the angular speed of the propeller as seen in Figure 5.29:

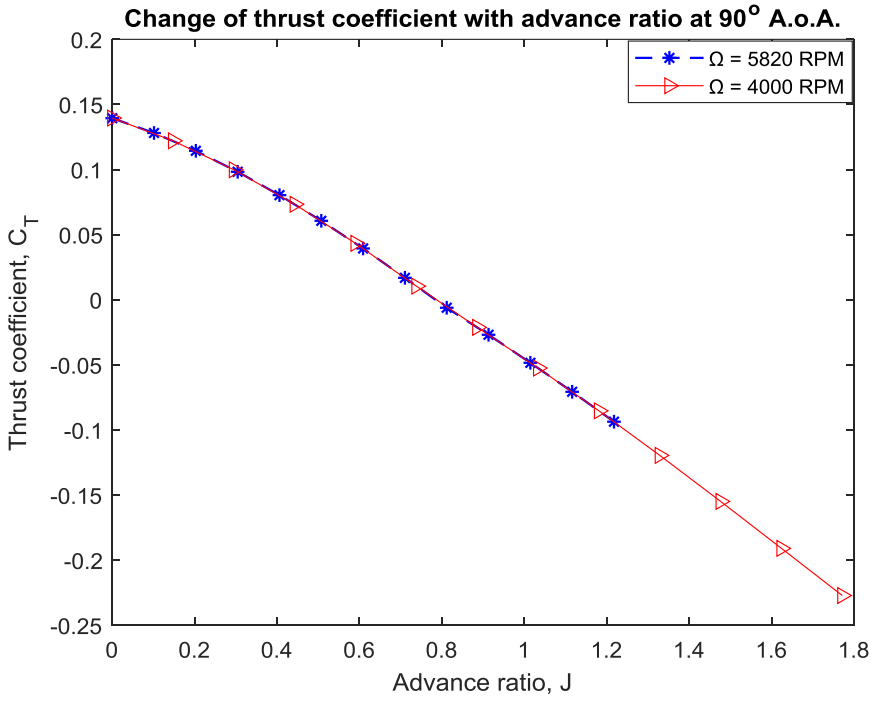

Figure 5.29: The change of the thrust coefficient (C_t) of 8x4.5in propeller with respect to the advance ratio (J), at 90° A.o.A.

However, thrust coefficient depends on the propeller disk A.o.A. as can be deduced from Figure 5.30. Like the thrust force, thrust coefficient is increases with free-stream velocity only when the flow is parallel to the rotor disk. On the other hand, thrust coefficient is decreases with an increasing free-stream velocity. It is most affected from the free-stream velocity, when the flow is perpendicular to the rotor disk (See Figure 2.5 for $\alpha = 90°$).

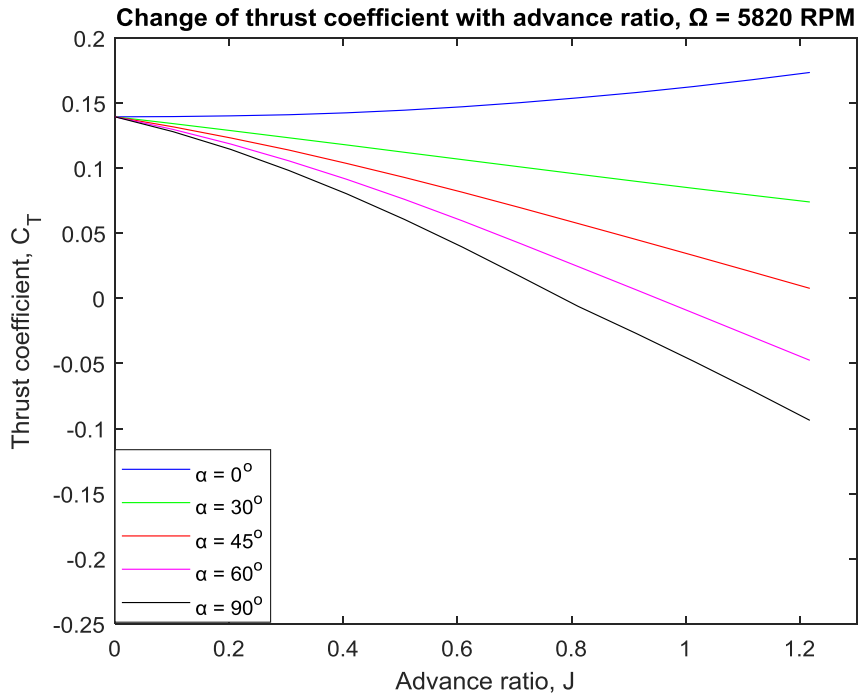

Figure 5.30: The change of the thrust coefficient at different propeller disk angles of attack.

Power coefficient is found as follows:

$$C_P = \frac{\mathrm{Q}}{\rho n^3 \mathrm{D}^5}\Omega \tag{5.4}$$

Change of the power coefficient of 8x4.5in propeller with respect to the advance ratio at 90° A.o.A., at 5820 RPM, at different propeller disk angles of attack is given in Figure 5.31. Because the power coefficient depends on rotor torque (Figure 5.12), its decreasing trend with free-stream velocity is similar to rotor torque.

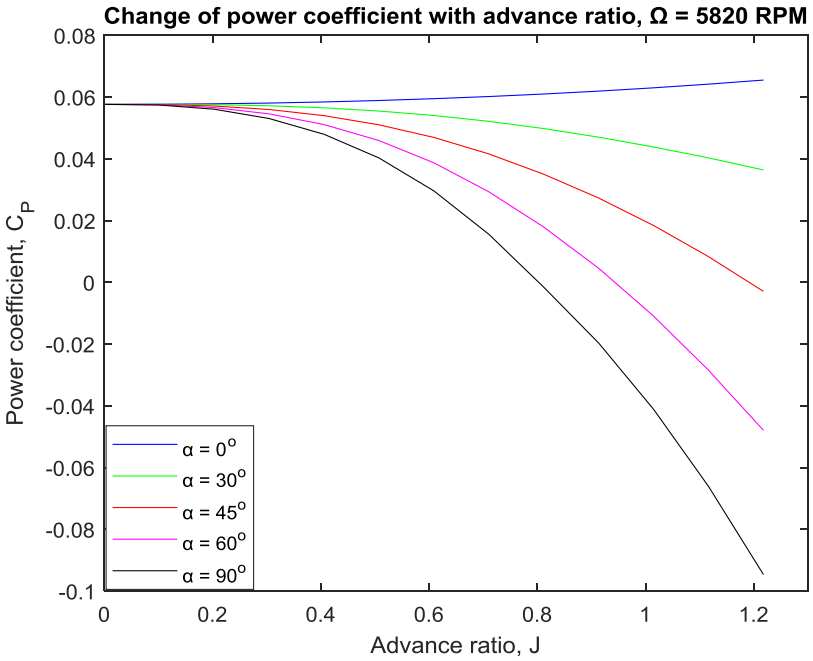

Figure 5.31: The change of the power coefficient at different propeller disk angles of attack.

Propeller efficiency in the presence of the free-stream velocity is calculated as:

$$\eta = \frac{C_T}{C_P} J \tag{5.5}$$

The variation of the propeller efficiency with the advance ratio is given in Figure 5.32. The figure implies that the propeller's aerodynamic efficiency is independent of the propeller's angular speed.

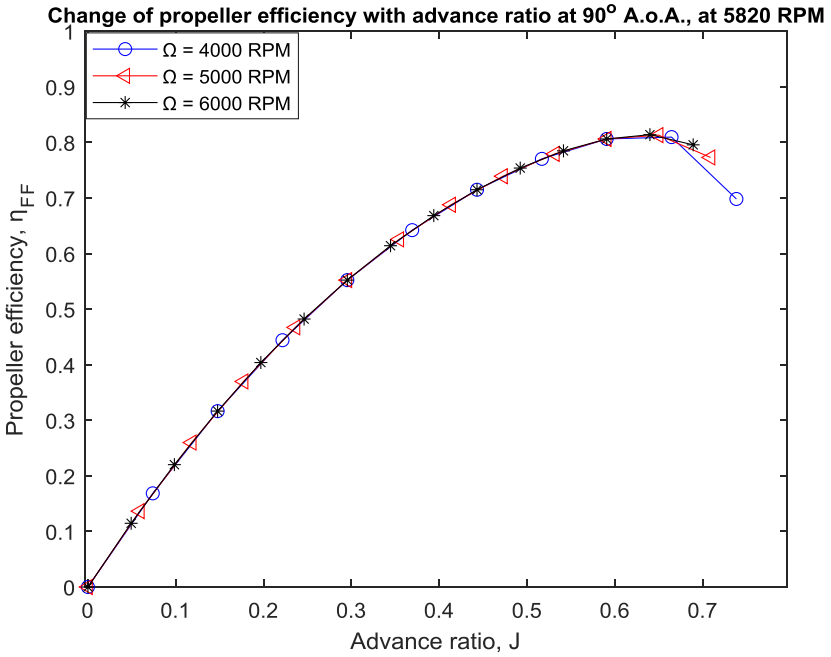

Figure 5.32: Efficiency at different angular speeds of the propeller.

5.5 Propeller Design Optimization's Results

This section aims to demonstrate the application of the IBEMT model improved in this thesis in a propeller design optimization problem. Hence, a propeller design optimization study is conducted whose design variables are twist angle, chord length, and angular speed of the propeller. Optimization is conducted at three different radiuses, using three different airfoils, and two different numbers of blades at a given free-stream velocity and thrust required value.

Minimum thrust required equals $98\ N$ and the corresponding free-stream velocity equals $21\ m/s$ for a reference aircraft with the given specifications in Table 4.1. First of all, the propeller design optimization at a given thrust required and free-stream velocity are performed using two-bladed and three-bladed propellers having 17in, 18in, and 19in radiuses to see the effect of the propeller size and blade's number on the maximum propeller aerodynamic efficiency. The results are given in Figure 5.33 and Figure 5.34:

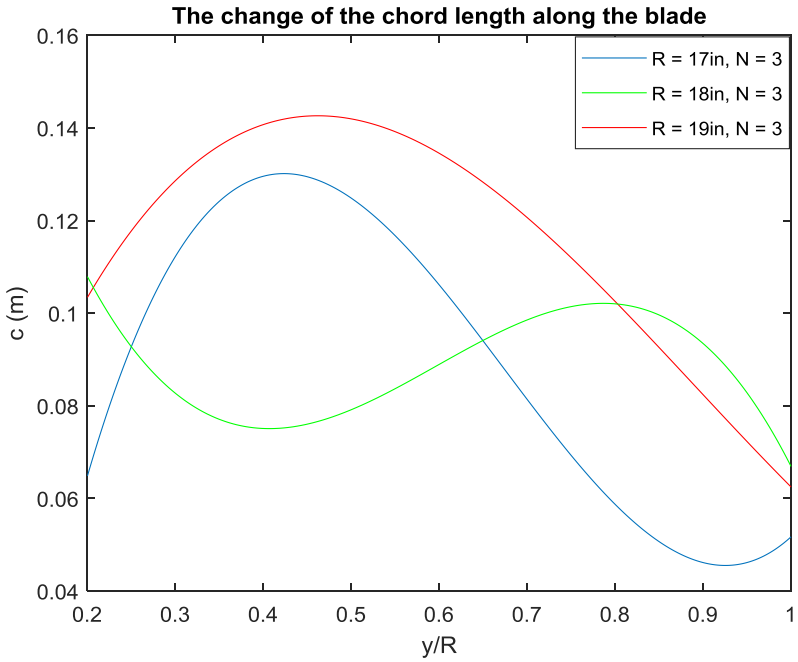

Figure 5.33: Chord distributions along the blade for different sizes of propeller, at minimum thrust required, $T = 98\ N$, V_∞=21 m/s.

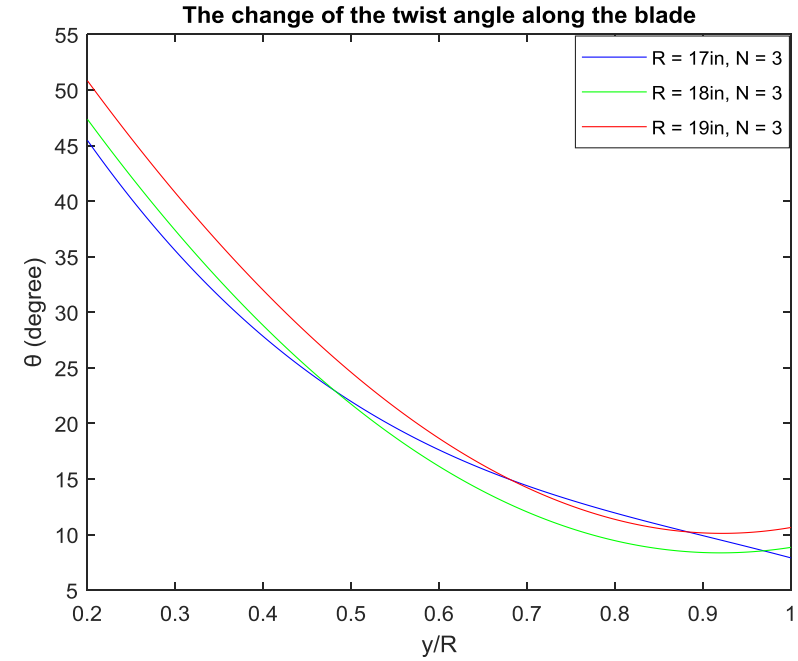

Figure 5.34: Twist angle distributions along the blade for different sizes of propeller, at minimum thrust required, $T = 98\ N$, V_∞=21 m/s.

Propeller's speed and the maximum efficiency are given in Table 5.2 for a 17in, 18in, and 19in propeller with different number of blades. The propeller's speed is decreases as the propeller radius increases (Table 5.2).

Table 5.2: Angular speed of the propeller and maximum aerodynamic efficiency at different propeller sizes and number of blades.

Inputs		Outputs	
R	N	Ω (RPM)	η_{max}
17in	2	2470.7	0.7081
18in	2	2318.0	0.7301
19in	2	1934.3	0.7354
17in	3	2243.9	0.7460
18in	3	2077.8	0.7509
19in	3	1690.2	0.7743

It can be concluded that within design size limits, the highest radius can be used to meet the cruise minimum thrust required constraint for maximum propeller aerodynamic efficiency. Besides, it is found that the performance of the three-bladed propeller is better than the two-bladed propeller at the same radius as shown in Figure 5.35. As well, it is concluded from Figure 5.36 that the required RPM for two-bladed propellers at the same radius are higher than the three-bladed propellers as expected.

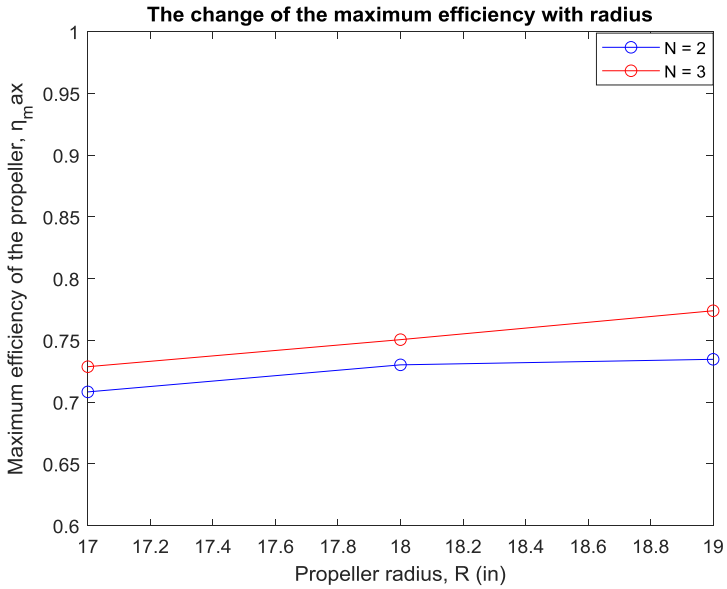

Figure 5.35: Effects of propeller radius and number of blades on the maximum propeller aerodynamic efficiency, $T = 98\ N$, V_∞=21 m/s.

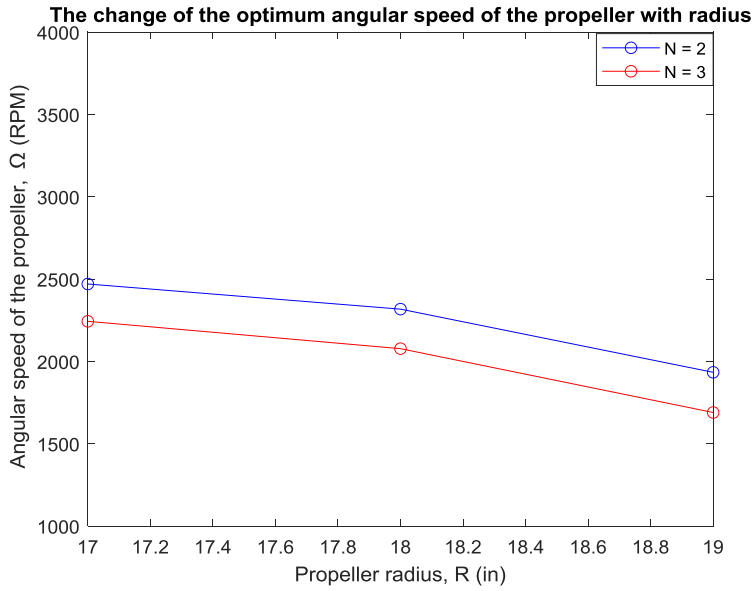

Figure 5.36: Effects of propeller radius and number of blades on the optimum angular speed of the propeller, $T = 98\ N$, V_∞=21 m/s.

Based on how propeller twist angle and angular speed vary during flight, aircraft propellers can be classified into three main types: Fixed-pitch variable-speed propeller, variable-pitch constant-speed propeller, and variable-pitch variable-speed

propeller. A fixed-pitch propeller can only be controlled by changing only its propeller's angular speed [15, 19, 21]. Variable-pitch propellers can adapt to changing flight conditions. They are used in various dynamical systems such as wind turbines, drones, and helicopters. The fundamental advantage of a variable-pitch propeller over a fixed-pitch propeller is being able to change the direction of the thrust vector very fast which is efficient in control.

Firstly, an optimization study is performed using the IBEMT model improved in this thesis for a fixed-pitch variable-speed propeller. In this case, the propeller's geometry is constant. To achieve the thrust required value at corresponding free-stream velocity, only the propeller's angular speed is changed. Then, the efficiency and the required RPM value is noted. The results are given in Table 5.3:

Table 5.3: Fixed-pitch variable-speed propeller optimization results with given propeller's geometry for three-bladed 19in propeller.

Inputs			Outputs	
$V_\infty\ (m/s)$	α (°)	$T_R\ (N)$	Ω (RPM)	η
21	90	98.0	1609.2	0.7743
25	90	104.7	1889.8	0.8007
30	90	125.0	2185.5	0.8140
35	90	155.3	2507.7	0.8196
40	90	194.5	2844.9	0.8219

Secondly, an optimization study is performed using the IBEMT model improved in this thesis for a variable-pitch constant-speed propeller that operates by adjusting the twist angle of the blades to keep them operating at the most efficient twist angle with a constant RPM value. In this case, the geometry (i.e., twist angle) of a three-bladed 19in propeller is changed at each blade section by increasing them with an amount of $d\theta$ assuming a variable-pitch mechanism is used. During the optimization, the

geometric values found for the three-bladed 19in propeller and the propeller speed are taken as constant, and then how much the twist angle of the propeller should rotate (i.e., $\theta + d\theta$) for the other thrust required and free-stream velocities is calculated. That is, $d\theta$ values are found by the optimization and they are presented in Table 5.4:

Table 5.4: Variable-pitch constant-speed propeller optimization results at 1690.2 RPM, for three-bladed 19in propeller.

Inputs			Outputs	
$V_\infty\ (m/s)$	$\alpha\ (°)$	$T_R\ (N)$	$d\theta\ (°)$	η
21	90	98.0	0	0.7743
25	90	104.7	3.30	0.8006
30	90	125.0	7.92	0.8121
35	90	155.3	12.77	0.8101
40	90	194.5	17.71	0.7988

In variable-pitch constant-speed propeller case, the required thrust can only be achieved by increasing the twist angle of the propeller. However, after $25\ m/s$, increasing the twist angle such as 12.77° and 17.71° decreases the aerodynamic efficiency because of the stall phenomena.

The results are demonstrated in Figure 5.37 for the variable-pitch constant-speed case.

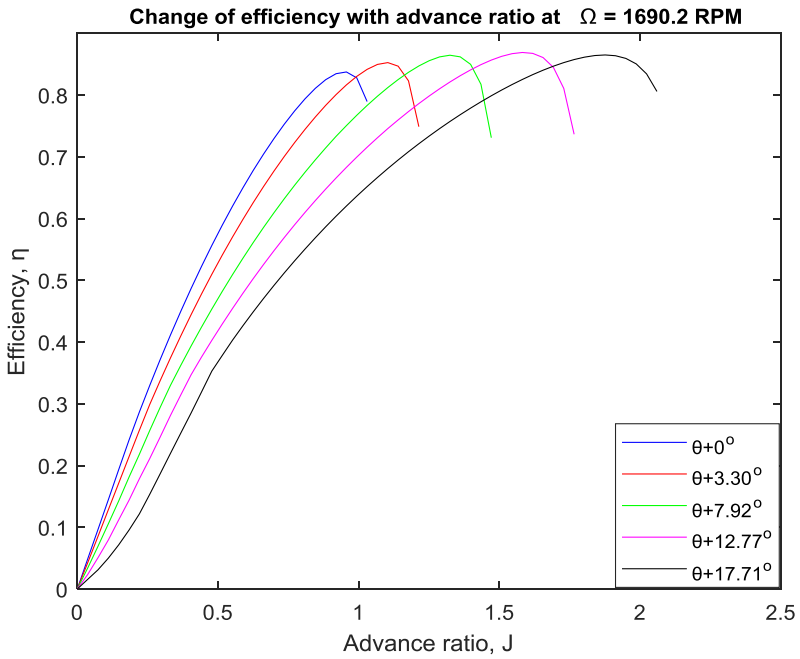

Figure 5.37: Variable-pitch constant-speed optimization results using the current airfoil (Figure 2.15) with R = 19in and $N = 3$.

As seen in Figure 5.37, propeller aerodynamic efficiency can be increased at higher free-stream velocities by increasing the propeller twist angle along the blade at a constant RPM using a variable-pitch mechanism given in Table 5.4. How much the twist angle needs to be increased ($d\theta$) can be found through optimization. Then, the optimization results can be used in the control of an aircraft having variable-pitch propeller configurations which has been studied with great interest lately in control engineering [52-62]. However, increasing only the twist angle might cause decrease in aerodynamic efficiency because blade's A.o.A. experiences more stall. Therefore, variable-pitch variable-speed propeller case is studied to obtain higher propeller aerodynamic efficiency.

Variable-pitch variable-speed case is investigated using the MATLAB® Optimization Toll-Box and the IBEMT model, and then the results are given in Table 2.1:

Table 5.5: Variable-pitch variable-speed propeller optimization results for three-bladed 19in propeller.

Inputs			Outputs		
$V_\infty\ (m/s)$	α (°)	$T_R\ (N)$	$d\theta$ (°)	Ω (RPM)	η
21	90	98.0	0	1609.2	0.7743
25	90	104.7	0.55	1853.0	0.8007
30	90	125.0	3.00	1968.7	0.8165
35	90	155.3	1.1	2404.2	0.8224
40	90	194.5	4.30	2450.3	0.8262

The comparison of propeller aerodynamic efficiency of each type of propeller is given in Table 5.6:

Table 5.6: The propeller aerodynamic efficiency of each type of aircraft propeller.

$V_\infty\ (m/s)$	Fixed-pitch variable-speed, η	Variable-pitch constant-speed, η	Variable-pitch variable-speed, η
25	0.8007	0.8006	0.8007
30	0.8140	0.8121	0.8165
35	0.8196	0.8101	0.8224
40	0.8219	0.7988	0.8262

At lower free-stream values such as $25\ m/s$, the propeller aerodynamic efficiencies of each type of the propeller are very close to each other because $d\theta$ is lower and acceptable as seen in Table 5.4. As the free-stream velocity increases the difference between the efficiencies increases. In terms of propeller aerodynamic efficiency, the variable-speed propellers show better performance than the constant-speed propeller

(Table 5.6) because increasing the twist angle causes stall in blade's angle of attack. Therefore, it is very meaningful to get lower aerodynamic efficiency in variable-pitch constant-speed propeller case at higher free-stream velocities (Table 5.4). As well, changing RPM and twist angle at the same time gives higher efficiency (Table 5.6) because the angular velocity and twist angle are optimized at the same time hence blade can operate at the optimum condition.

To sum up, variable-pitch variable-speed propeller is more efficient compared to fixed-pitch variable-speed and variable-pitch constant-speed propellers. Besides, variable-pitch propellers are known as more efficient in terms of control with increased controller bandwidth and the addition of reverse thrust capabilities [61, 62]. According to the overall efficiency, the propeller-motor combination should also be considered in terms of efficiency of the motor drive system defined by a ratio of mechanical power to electric power.

CHAPTER 6

CONCLUSION, DISCUSSION and FUTURE WORK

6.1 The IBEMT Model

In conclusion, a high-fidelity simulation model is required for the analysis of UAV design and flight performance. Since the open-source tools do not meet our demand because they cannot be modified by the user, and commercial tools are unaffordable for UAV optimization, an in-house BEMT model that is able to simulate the propeller in all flight conditions is decided to be studied for multirotor UAV optimizations. In this study, a mathematical model for propellers that is able to predict the aerodynamic forces and moments in all three axes under different flight conditions such as hover, vertical climb, and forward flight is presented. The IBEMT is a physics-based model that uses Blade Element and Momentum Theory by eliminating some assumptions in Blade Element Theory, and calculated induced velocity iteratively using Momentum Theory. Thus, using a propeller's geometric parameters, without the need for wind tunnel tests or CFD methods, all aerodynamic loads of propellers can be predicted thanks to the IBEMT model. It has a lower computational cost than the CFD and experimental studies and higher accuracy compared to the classical BET. The results of the IBEMT model are validated with wind tunnel experiments at various angles of attack ($0°, 30°, 45°, 60°,$ and $90°$), free-stream velocities (i.e., $0, 2.33, 4.08, 7.57, 9.32, 11.07\ m/s$), and propeller's speeds (i.e., $2000, 2600, 3340, 4070, 4860, 5560, 6290,$ and 7000 RPM) for thrust force. As well, the results of the IBEMT model for thrust and power coefficients using 2 different propellers operating different flight conditions are compared with another experimental study in which the geometric properties of the propeller used in the study are given in detail.

In addition, a more developed stall model is used whose input parameters depending on the airfoil of the propeller. The AERODAS stall model is more realistic because the airfoil information of the propeller is utilized. The airfoil information is obtained by cutting the propeller using a laser cutting machine.

Besides, the effects of the assumptions in the classical BET are investigated using the IBEMT model. The vertical climb case (Figure 2.5) is used because it is concluded that the thrust force is most affected by the free-stream velocity in the vertical climb case. As a result, the following conclusions and recommendations are given:

- As expected the thrust force decreases greatly at higher propeller disk angles of attack and higher speeds.
- Thrust force is most affected by the free-stream velocity at 90 A.o.A. (i.e., vertical climb).
- At higher RPM values such as more than 4000 RPM and the higher free-stream velocities such as more than 10 m/s, using the IBEMT model gives more accurate results compared to wind tunnel tests because of the vibrations of the test set-up.
- Assumption 2 affects the results remarkably, and it is not recommended to be used in a high-fidelity BEMT model. A stall model should be included in order to increase the accuracy.
- Drag force can be neglected in the calculation of thrust force in BEMT applications.
- Linear twist and mean chord assumptions can be applied instead of using twist angle and chord length as a function of the blade section.
- Assumption 6 can be used up to 10 m/s free-stream velocity. However, as the free-stream velocity increases, assuming the inflow angle is too small is not reasonable.

- Accurate calculation of induced velocity is essential in order to get an accurate result. Hence, it is recommended to calculate the induced velocity at each annulus of the rotor disk.
- The distribution of the twist angle along the radius affects the results remarkably. Therefore, identification of the twist angle is very important in the estimation of the propeller loads. Propeller forces and moments are very sensitive to the twist angle.
- Because rotor torque, hub force, and rolling moment are at least one order of magnitude smaller than thrust force, they should be measured by a more sensitive load cell.

To sum up, accurate calculation of induced flow and stall model plays an important role in the accurate estimation of propeller's loads. Besides, the IBEMT model is very sensitive at each 1° twist angle value.

The Mach number of the 8x4.5in propeller (R = 4in) at 7000 RPM at 11 m/s at the tip is found 0.251. Therefore, the compressibility effect is ignored since it is lower than 0.3. The IBEMT model can be developed such as by adding tip and hub losses as in wind turbine blades.

6.2 Applications

Because the in-house improved BEMT model proposed in this thesis is fast and gives accurate results in the presence of propeller disk A.o.A. and free-stream velocity, the optimum propeller design can be reached in terms of its chord and twist distributions along the blade and angular speed of the propeller for a given required thrust and free-stream velocity serving the IBEMT model as an input to the optimization code. Besides, the control of variable-pitch propellers can be studied that enables to increase the controller bandwidth with a variable-pitch mechanism. Moreover, optimum airfoil and radius of the propeller can be determined using the optimization developed in this study by comparing their performances. However, the coaxial

propeller configurations cannot be analyzed by a model-based method study like the IBEMT model because the in-house BEMT models have no capability to study flow around the propeller when the flow is disturbed by a surface. For these kinds of studies experimental and CFD methods are recommended to be performed.

Following conclusions are presented for the application of the IBEMT model in propeller design optimization:

- Three-bladed propellers are more efficient than two-bladed propellers at the same propeller radius. On the other hand, as the propeller radius increases efficiency also increases. If the radius is limited, then the number of blades is recommended to be increased to get higher aerodynamic efficiency.
- As the free-stream velocity increases, maximum propeller aerodynamic efficiency can be reached by increasing the twist angle of the blade with a variable-pitch mechanism at constant RPM.
- Variable-pitch variable-speed propellers are more efficient compared to fixed-pitch variable-speed and variable-pitch constant-speed propellers.
- In terms of propeller aerodynamic efficiency, the variable-speed propellers show better performance than the constant-speed propeller. However, the propeller-motor combination should also be considered in terms of the efficiency of the motor drive system defined by a ratio of mechanical power to electric power.

REFERENCES

[1] Rankine, W. J. M. 1865. On the Mechanical Principles of the Action of Propellers. Transaction of the Institute of Naval Architects, Vol. 6.

[2] Froude, R. E. 1889. On the Part Played in Propulsion by Difference in Pressure. Transactions of the Institute of Naval Architects, Vol. 30, pp. 390–405.

[3] Kaya, D. 2014. Modeling and Experimental Identification of Quadrotor Aerodynamics. M.Sc. Thesis. Department of Aerospace Engineering, Middle East Technical University, Ankara, Turkey.

[4] Kaya, D. Kutay, A. T. 2014. Aerodynamic Modeling and Parameter Estimation of a Quadrotor Helicopter. AIAA Aviation, Atmospheric Flight Mechanics Conference, Atlanta, GA, AIAA 2014-2558.

[5] Cevher L. 2019. Control System Design and Implementation for a Tilt Rotor UAV. M.Sc. Thesis. Department of Aerospace Engineering, Middle East Technical University, Ankara, Turkey.

[6] Gill, R. D'Andrea, R. 2019. Computationally Efficient Force and Moment Models for Propellers in UAV Forward Flight Applications. Drones 3, no. 4: 77.

[7] Podsędkowski, M. Konopiński, R. Obidowski, D. Koter, K. 2020. Variable Pitch Propeller for UAV-Experimental Tests. Energies 2020, 13, 5264.

[8] Westmoreland, W. Tramel, R. Barber, J. 2008. Modeling Propeller Flow-Fields Using CFD. In 46th AIAA Aerospace Sciences Meeting and Exhibit, Reno, NV, USA.

[9] Dubbioso, G. Muscari R. Mascio A. D. 2013. CFD Analysis of Propeller Performance in Oblique Flow. Third International Symposium on Marine Propulsors smp'13, Launceston, Tasmania, Australia.

[10] Yener, S. 2019. A Computational Analysis on Rotor-Propeller Arm Interaction in Hovering Flight. M.Sc. Thesis. Department of Aerospace Engineering, Middle East Technical University, Ankara, Turkey.

[11] Leishman, J. G. 2006. Principles of Helicopter Aerodynamics. 2nd Edition, Cambridge University Press, NY.

[12] Seddon, J. M. 1990. Basic Helicopter Aerodynamics. Kent, Great Britain: BSP Professional Books.

[13] Fay, G. 2001. Derivation of the Aerodynamic Forces for the Mesicopter Simulation.

[14] Wheatley, J. B. 1934. An Aerodynamic Analysis of the Autogiro Rotor with a Comparison Between Calculated and Experimental Results. NACA Report No. 487.

[15] Bouabdallah, S. 2007. Design and control of quadrotors with application to autonomous flying. Ph.D. dissertation, Ecole Polytechnique Federale de Lausanne.

[16] Orsag, M. S. Bogdan. 2012. Influence of Forward and Descent Flight on Quadrotor Dynamics. Agarwal, R. K. Recent Advances in Aircraft Technology. Zagreb, Croatia: InTech, 141-15.

[17] Bresciani, T. 2008. Modelling, identification and control of a quadrotor helicopter. Master's Thesis, Lund University Libraries.

[18] Powers, C. Mellinger, D. Kushleyev A. Kothmann B. Kumar V. 2013. Influence of Aerodynamics and Proximity Effects in Quadrotor Flight. Experimental Robotics: The 13th International Symposium on Experimental Robotics (pp.289-302).

[19] Achtelik, M. 2010. Nonlinear and Adaptive Control of a Quadcopter. M.Sc. Thesis. Institute of Flight System Dynamics, Technical University Munich.

[20] Mellinger, D. Michael N. Kumar V. 2012. Trajectory Generation and Control for Precise Aggressive Maneuvers with Quadrotors. International Journal of Robotics Research, 31(5), 664-674.

[21] Kaya, D. Buyukkocak, A. T. Kutay, A. T. Tekinalp, O. 2016. Design and control of a Micro UAV. AIAA Aviation, Atmospheric Flight Mechanics Conference, Washington, D.C.

[22] Hepperle, M. 2008. Javaprop user manual.

[23] Drela, M. 2006. Qprop Formulation. MIT Aero & Astro.

[24] Silvestre M. Morgado J. Pascoa J. 2013. JBLADE: A Propeller Design and Analysis Code. International Powered Lift Conference - AIAA AVIATION Forum.

[25] Martin, D. QBlade Short Manual, retrieved http://www.q-blade.org/, 12/11/2020.

[26] Johnson, W. 1988. A Comprehensive Analytical Model of Rotorcraft Aerodynamics and Dynamics. Johnson Aeronautics, Palo Alto, California.

[27] Serrano, D. Ren, M. Qureshi, A. J. Ghaemi, S. 2019. Effect of Disk Angle-of-Attack on Aerodynamic Performance of Small Propellers. Aerospace Science and Technology, Volume 92, September 2019, Pages 901-914, DOI: 10.1016/j.ast.2019.07.022.

[28] Gill, R. D'Andrea, R. D. 2017. Propeller Thrust and Drag in Forward Flight. IEEE Conference on Control Technology and Applications (CCTA). Kohala Coast, Hawai'i, USA.

[29] Khan, W. Nahon, M. 2015. A Propeller Model for General Forward Flight Conditions. International Journal of Intelligent Unmanned Systems, Vol. 3, 2/3 pp. 72 – 92.

[30] Molter C. Cheng P. W. 2017. Propeller Performance Calculation for Multicopter Aircraft at Forward Flight Conditions and Validation with Wind Tunnel Measurements. International Micro Air Vehicle Conference and Flight Competition (IMAV).

[31] Spera, D. A. 2008. Models of Lift and Drag Coefficients of Stalled and Unstalled Airfoils in Wind Turbines and Wind Tunnels. Technical Report. NASA-2008-215434.

[32] Airfoil Tools: retrieved: http://airfoiltools.com/airfoil/naca4digit, 10/11/2020.

[33] Hoerner, S. F. Henry, V. B. 1975. Fluid-Dynamic Lift: Practical Information on Aerodynamic and Hydrodynamic Lift. NASA STI/Recon Technical Report No. A76, Washington, DC, 32167.

[34] Stringer, D. et al. 2018. A new 360° Airfoil Model for Predicting Airfoil Thrust Potential in Vertical-Axis Wind Turbine Designs. Journal of Renewable and Sustainable Energy. 10-1. pp 013304.

[35] MATLAB® Optimization Toolbox Functions, retrieved https://www.mathworks.com/help/optim/ug/problems-handled-by-optimization-toolbox-functions.html#tblminprobs, 12/05/2021.

[36] Karim, M. M., Ikehata, M. 2000. A Genetic Algorithm (GA) Based Optimization Technique for the Design of Marine Propeller, in SNAME symposium on Propeller/Shafting, Virginia Beach, USA.

[37] Benini, E. 2004. Significance of Blade Element Theory in Performance Prediction of Marine Propellers, Ocean Engineering, Vol. 31, No. 8, pp. 957-974.

[38] Emmerich, M., T. M. Hundemer, J. Varcol M. C. Abdel-Maksoud, M. 2006. Design Optimization of Ship Propellers by Means of Advanced Metamodel-assisted Evolution Strategies, International Conference on Design Optimization, Las Palmas, Gran Canaria.

[39] Dunja, M. Roko, D. 2008. Neural Network Prediction of an Optimum Ship Screw Propeller, in 19th International DAAAM Symposium, Vienna.

[40] Taheri, R. Mazaheri, K. 2013. Hydrodynamic Optimization of Marine Propeller using Gradient and Non-Gradient-based Algorithms, Acta Polytechnica Hungarica, Vol. 10, No. 3, pp. 221-237.

[41] Vesting, F. Johansson, R. Bensow, R. E. 2013. Parameter Influence Analysis in Propeller Optimisation, Third International Symposium on Marine Propulsors smp'13, Launceston, Tasmania, Australia.

[42] Tadros, M. Vettor, R. Ventura, M. Guedes Soares, C. 2021. Coupled Engine-Propeller Selection Procedure to Minimize Fuel Consumption at a Specified Speed. J. Mar. Sci. Eng., 9, 59. https://doi.org/10.3390/jmse9010059.

[43] Moita, N. S. M., Marta, A. C. 2018. Optimization of the Propeller-Driven Propulsion System for a Small UAV. In: Rodrigues H. et al. (eds) EngOpt 2018 Proceedings of the 6th International Conference on Engineering Optimization. EngOpt, Springer, Cham. https://doi.org/10.1007/978-3-319-97773-7_118.

[44] Kaya, D. Kutay, A. T. Kurtuluş, D. F. Tekinalp, O. Şimşek, İ. Hoşgit, G. Soysal, S. 2016. Propulsion System Selection and Modeling for a Quadrotor with Search and Rescue Mission. AIAA SciTech, San Diego, California, January 2016., DOI: 10.2514/6.2016-1528.

[45] Dai, X. Quan, Q. Ren J. Cai, K. 2019. An Analytical Design-Optimization Method for Electric Propulsion Systems of Multicopter UAVs With Desired Hovering Endurance. in IEEE/ASME Transactions on Mechatronics, vol. 24, no. 1, pp. 228-239, Feb. 2019, DOI: 10.1109/TMECH.2019.2890901.

[46] Park, D. Lee, Y. Cho, T. Kim, C. 2018. Design and Performance Evaluation of Propeller for Solar-Powered High-Altitude Long-Endurance Unmanned Aerial Vehicle, International Journal of Aerospace Engineering Volume 2018, Article ID 5782017, 23 pages, DOI: https://doi.org/10.1155/2018/5782017.

[47] Toman, U. T. Abdel-Karim SO Hassan, Owis F. M. Mohamed, A. S. A. 2019. Blade Shape Optimization of an Aircraft Propeller Using Space Mapping Surrogates. Advances in Mechanical Engineering 2019, Vol. 11(7) 1–16.

[48] Ngatchou, P. Zarei, A. El-Sharkawi, M. A. 2005. Pareto Multi Objective Optimization. Intelligent Systems Application to Power Systems, pages 84–89, DOI: 10.1109/ISAP.2005.1599245.

[49] van Neerven J. M. F. 2020. Design of a Variable Pitch, Energy-Harvesting Propeller for In-Flight Power Recuperation on Electric Aircraft, M.Sc. Thesis, Department of Aerospace Engineering, TU Delft.

[50] AeroFoilEngineering, retrieved: https://aerofoilengineering.com/index.php, 01/0.6/2021.

[51] Anderson, J. D. 2001. Fundamentals of Aerodynamics. 3rd Edition. McGraw-Hill, New York, NY.

[52] Podsedkowski, M. Konopinski, R. Obidowski, D. Koter, K. 2020. Variable Pitch Propeller for UAV-Experimental Tests. Energies 2020, 13(20), 5264, DOI: 10.3390/en13205264.

[53] Sheng, S. Sun, C. 2016. Control and Optimization of a Variable-Pitch Quadrotor with Minimum Power Consumption. Energies, 9(4), 232, DOI: 10.3390/en9040232.

[54] Fresk, E. Nikolakopoulos, G. 2014. Experimental Model Derivation and Control of a Variable Pitch Propeller Equipped Quadrotor. 014 IEEE Conference on Control Applications (CCA), Juan Les Antibes, pp. 723-729, DOI: 10.1109/CCA.2014.6981426.

[55] Cutler, M. Ure, N. Michini, B. How, J. 2011. Comparison of Fixed and Variable Pitch Actuators for Agile Quadrotors. AIAA Guidance, Navigation, and Control Conference, Portland, Oregon, p. 6406.

[56] Cohen, R. Miculescu, D. Reilley, K. Pakmehr, M. Feron, E. 2013. Online Performance Optimization of a DC Motor Driving a Variable Pitch Propeller. [Online]. Available: https://arxiv.org/abs/1310.0133.

[57] Manchin, A. Mahmod Lafta, W. Viet Dao, D. 2019. Smart Variable Pitch Propeller System for Unmanned Aerial Vehicles. International Journal of Engineering & Technology, 7(4), 5238-5241.

[58] Cutler, M. How, J. 2015. Analysis and Control of a Variable-Pitch Quadrotor for Agile Flight. J. Dyn. Syst. Meas. Control, 137, 101002.

[59] Bhargavapuri, M. Sahoo, S.R. 2019. Kothari, M. Robust Nonlinear Control of a Variable-Pitch Quadrotor with the Flip Maneuver. Control Eng. Pract. 87, 26–42.

[60] Henderson, T. Papanikolopoulos, N. 2019. Power-Minimizing Control of a Variable-Pitch Propulsion System for Versatile Unmanned Aerial Vehicles. In Proceedings of the 2019 International Conference on Robotics and Automation (ICRA), Montreal, QC, Canada, 20–24 May 2019; pp. 4148–4153.

[61] Pretorius, A. Boje, E. 2014. Design and Modelling of a Quadrotor Helicopter with Variable Pitch Rotors for Aggressive Manoeuvres. Volume 47, Issue 3, pages 12208-12213, DOI: 10.3182/20140824-6-ZA-1003.01586.

[62] Gupta, N. Kothari, M. and Abhishek. 2016. Flight Dynamics and Nonlinear Control Design for Variable-Pitch Quadrotors. American Control Conference (ACC), 2016, pp. 3150-3155, DOI: 10.1109/ACC.2016.7525402.

CURRICULUM VITAE

PERSONAL INFORMATION

Surname, Name: Kaya, Derya
Nationality: Turkish (TC)
Date and Place of Birth: August 1986, Turkey
Marital Status: Married

EDUCATION

Degree	Institution	Year of Graduation
MS	METU Aerospace Engineering	2014
BS	METU Physics	2010

WORK EXPERIENCE

Year	Place	Enrollment
2015-Present	METU, Aerospace Engineering	Research Assistant
2013-2015	METU, Career Planning Center	Research Assistant

FOREIGN LANGUAGES

Advanced English, Intermediate German

INTERNATIONAL CONFERENCE PAPERS

1. Metehan Yayla, Derya Kaya, Ali Türker Kutay, "High Gain Observer based Attitude and Altitude Control of a Quadrotor", AIAC, Ankara, (September 2017).

2. Derya Kaya, Ali Türker Kutay, Ozan Tekinalp, "Experimental Analysis of Optimal Gap Distance between Rotors of a Quadrotor UAV"-Aviation, Denver, Colorado-USA, (June 2017).

3. Derya Kaya, Ali Tevfik Büyükkoçak, Ali Türker Kutay, Ozan Tekinalp, "Design and Control of a Micro UAV" AIAA-Aviation, Washington D. C.-USA, (June 2016).

4. Derya Kaya, Ali Türker Kutay, Dilek Funda Kurtuluş, Ozan Tekinalp, İlay Şimşek, Gürkan Hoşgit, Sefa Soysal, “Propulsion System Selection and Modeling for a Quadrotor with Search and Rescue Mission” AIAA-SciTech, San Diego-USA, (January 2016).

5. Derya Kaya and Ali Türker Kutay, “Modeling and Simulation of a Quadrotor using Curve Fitting Method”, AIAA-Aviation, Dallas-USA, (June 2015).

6. Derya Kaya and Ali Türker Kutay, “Aerodynamic Modeling and Parameter Estimation of a Quadrotor UAV”, AIAA-Aviation, Atlanta-USA, (June, 2014).

7. Derya Kaya and Ali Türker Kutay, “Modeling, Simulation, and System Identification of a Quadrotor UAV”, (September 2013), Ankara International Aerospace Conference (AIAC), Ankara-Turkey, (September 2013).